

THERMAL METROLOGY AND CHARACTERIZATION OF HIGH THERMAL CONDUCTIVITY POLYMER FIBERS AND FABRICS

by

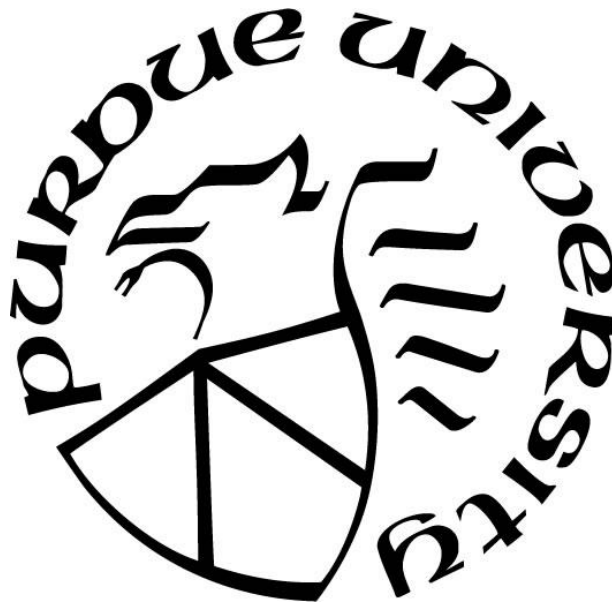
Aaditya A. Candadai

A Dissertation

Submitted to the Faculty of Purdue University

In Partial Fulfillment of the Requirements for the degree of

Doctor of Philosophy



School of Mechanical Engineering

West Lafayette, Indiana

May 2021

THE PURDUE UNIVERSITY GRADUATE SCHOOL
STATEMENT OF COMMITTEE APPROVAL

Dr. Amy M. Marconnet, Co-Chair

School of Mechanical Engineering

Dr. Justin A. Weibel, Co-Chair

School of Mechanical Engineering

Dr. Tahira Reid Smith

School of Mechanical Engineering

Dr. Mukerrem Cakmak

School of Materials and Mechanical Engineering

Approved by:

Dr. Nicole Key

ACKNOWLEDGMENTS

I would like to express my deepest appreciation to Prof. Amy Marconnet and Prof. Justin Weibel. I thoroughly enjoyed my research experience while working under their mentorship and I truly could not have asked for better Ph.D. advisors. Their constant and dedicated support, technical expertise and constructive feedback, and genuine care towards my academic and professional development has guided me immensely throughout my time as a graduate student. I will always be grateful for the numerous learning opportunities and unceasing support they provided me with on all aspects of my research and professional growth. I would like to extend my sincere thanks to my committee member, Prof. Mukerrem Cakmak for his continuous support and valuable feedback, especially with respect to developing my understanding related to the materials engineering aspects of this work. I am also very grateful to my committee member, Prof. Tahira Reid for her support that enabled me to build on some aspects of her former student's work and for her insightful feedback related to the ergonomic considerations of this work. I am extremely grateful to Prof. Timothy Fisher for his support, guidance, and mentorship when I first came to Purdue in 2015, and for motivating me to take up a Ph.D. in this field.

I would like to sincerely thank all the industry members of the Cooling Technologies Research Center for their funding support and technical guidance. The CTRC Meetings were an integral and enjoyable part of my Ph.D. and were instrumental towards defining and shaping the specific goals and directions of this work. I would also like to thank Dr. Todd Salamon for a great summer internship (virtual) experience at Nokia Bell Labs.

I am very thankful to Prof. Alison Stewart in the Textiles Department at Purdue for allowing me to audit her weaving class and taking time out of her schedule to teach me the basic concepts of weaving. I acknowledge Prof. Ali Shakouri's assistance with providing access to his

equipment that I used to perform many measurements for this work. I am grateful to my former MTEC colleague, Dr. Jaesik Hahn for training me on using the IR microscope, a tool that I used throughout my research work and for introducing me to the Angstrom method which formed an integral foundation for various aspects of this thesis. I am thankful to Zeynep Mutlu for assisting me with polymer characterization measurements and Brian Fu for designing the laser heating fixture. I appreciate the support from my MTEC and CTRC colleagues - Dr. Collier Miers, Rajath Kantharaj and Srivathsan Sudhakar, for their help with various aspects of my experimental work in the lab. I am also thankful to my colleagues at the Birck Center - Rishav Roy, Prabhu Kumar, and Yuan Hu, for fruitful technical discussions related to my research. I have also been fortunate to work with some brilliant undergraduate students at Purdue. I thank Emily Nadler, Jack Burke, Radhakrishna Korlam and Debraliz Isaac-Aragones for their involvement and valuable contributions to this work. I acknowledge my lab mates Albraa Alsaati, Brian Fu, Dr. Anurag Kumar, Dr. Majed Alrefae, Dr. Arpan Kundu, Dr. Yuqiang Zeng, and all other MTEC, CTRC and NTRG lab mates for being helpful and supportive throughout.

My graduate school journey would not have been possible without the support of an amazing group of friends who were always there when I needed them – Saaketh, Rajath, Rishav, Srivathsan, Prabhu, Malavika, Revati, Pranav, Ujash, Aishwarya, Kshitiz, Sukshitha, Kaushik, Radha, Brian, Yuan and all friends at Purdue – thanks everyone!

I express my deepest thanks to my parents, sister, and my entire family for their moral and emotional support throughout. Special thanks to everyone in Atlanta who truly made me feel at home here in the US, and for the wonderful Thanksgiving breaks. Finally, I cannot begin to express my most sincere gratitude to my uncles, Deepak and Ashok, who have been role models for me in many ways. I would not have made it to where I am today without their incredible support.

TABLE OF CONTENTS

LIST OF TABLES.....	8
LIST OF FIGURES	9
ABSTRACT	14
CHAPTER 1. INTRODUCTION	17
1.1 Motivation and Background	17
1.2 Objectives and Major Contributions	20
1.3 Outline of the Document.....	21
CHAPTER 2. LITERATURE REVIEW	23
2.1 Gel-Spun High-Performance Polyethylene Fibers.....	23
2.1.1 Gel Spinning Process.....	24
2.1.2 Desirable Process Parameters	25
2.1.3 Thermal Conductivity Dependence on Draw Ratio	27
2.2 General Thermal Characterization Methods.....	29
2.2.1 Steady State Methods	29
2.2.1.1 Absolute Techniques	30
2.2.1.2 Comparative Techniques.....	30
2.2.1.3 Differential Techniques.....	31
2.2.2 Transient Methods	32
2.3 Related Work on High Thermal Conductivity UHMW-PE	35
2.4 Related work on high-performance fabrics	38
CHAPTER 3. INFRARED MICROSCOPY-ENHANCED CHARACTERIZATION: IN- PLANE HEATER WIRE METHODS	40
3.1 Micro-IR Angstrom Measurement Technique	40
3.2 Steady State Thermal Conductivity Measurement Technique	42
3.2.1 Methods	42
3.2.1.1 Experimental Facility Details	42
3.2.1.2 Thermal Characterization Methodology	45
3.2.2 Validation of the Measurement Technique	54
3.2.2.1 Nichrome Wire	54

3.2.2.2	High Density Polyethylene Sheet	55
3.2.3	Uncertainty and Sensitivity Analysis	56
3.2.4	Summary of the Developed Technique	59
CHAPTER 4. THERMAL CHARACTERIZATION OF ULTRA-HIGH MOLECULAR WEIGHT POLYETHYLENE: FROM FIBERS TO FABRICS		61
4.1	Methods	61
4.2	Results and Discussion	63
4.2.1	Effective Thermal Conductivity of Yarns	63
4.2.2	Effective Thermal Conductivity of Fabrics.....	67
4.2.3	Thermal Characterization of Fibers	72
4.2.4	Discussion	77
CHAPTER 5. THERMAL AND MECHANICAL CHARACTERIZATION OF COMMERCIAL HIGH-PERFORMANCE POLYMER FABRICS		81
5.1	Materials Survey and Selection	81
5.2	Experimental Methods	86
5.2.1	Thermal Metrology	86
5.2.2	Mechanical Metrology.....	86
5.3	Results and Discussion	88
5.3.1	Thermal Conductivity.....	88
5.3.2	Bending Stiffness	91
5.3.3	Crease Testing.....	92
5.3.4	Thermal Annealing	94
5.3.5	Thermal and Mechanical Property Assessment.....	96
CHAPTER 6. INFRARED-MICROSCOPY ENHANCED CHARACTERIZATION: IN-PLANE LASER-ANGSTROM METHOD		98
6.1	Concept and Experimental Methodology	98
6.2	Numerical Experiments	101
6.3	Numerical Analysis and Property Extraction	102
6.3.1	Generalized Numerical Approach	103
6.3.2	Reduced Analytical Model for Isotropic Case	105
6.4	Results and Discussion	107

6.4.1	Representative Analysis for Validation of the Method	107
6.4.2	Measurement Considerations	113
6.4.3	Experimental Demonstration	117
CHAPTER 7. CONCLUSION.....		121
7.1	Summary	121
7.2	Future Research Directions	123
7.2.1	Metrology related.....	124
7.2.2	Materials	126
APPENDIX A. BENDING STIFFNESS		128
APPENDIX B. DIFFERENTIAL SCANNING CALORIMETRY MEASUREMENTS		130
APPENDIX C. FIN HEAT CONDUCTION ANALYSIS OF ANNEALED DYNEEMA FABRICS		132
APPENDIX D. ANALYTICAL SOLUTION FOR 1D RADIAL-ANGSTROM METHOD		134
REFERENCES		136
VITA.....		147
PUBLICATIONS		148

LIST OF TABLES

Table 2.1: Summary of general thermal measurement techniques.....	33
Table 3.1: Nominal value and uncertainty in experimental and modeling parameters for the validation measurements (validation sample is another nichrome wire with same emissivity and diameter as the heater wire)	58
Table 5.1: Details of the different high-performance polymer fibers (shown in Figure 1)	84
Table 5.2: Summary of the materials considered in this study	85
Table 7.1: Topic Coverage of Future Research Directions.....	124

LIST OF FIGURES

Figure 2.1: Schematic representation of (a) the surface spinning technique (reproduced from [51]); and (b) the gel-spinning and drawing process (reproduced from [52]).....	25
Figure 2.2: (a) Illustration of solution concentration affecting entanglement density and drawability. (b) Schematic of the drawing process and its physical effect on the polymer molecular chains. These figures have been reproduced from [55].....	26
Figure 3.1: (a) Illustration of the principle of the micro-IR Angstrom method. (b) Experimental equipment showing the IR microscope, vacuum pump and sample stage employed in the thermal diffusivity measurements.	41
Figure 3.2: Schematics of the experimental setup. (a) The assembly consisting of the crossing sample and heater wire on a heat sink with a circular opening are placed in a vacuum chamber to minimize convection losses (see top-down view in inset). (b) Illustration of the energy balance in the wire–sample cross-structure arrangement; all of the heat conducted into the junction from the left and right sides of the heater wire (Q_L and Q_R , respectively) and the heat generated in the junction region (Q_{gen}) conducts into the sample (Q_T and Q_B). (c) Expected temperature profiles of the wire and the sample which are measured during the IR experiments. The heat rates (Q_L and Q_R) and temperature gradients dT/dy_T and dT/dy_B are calculated from these profiles.	44
Figure 3.3: (a) IR temperature map of the wire calibration experiment at a current input of 220 mA, corresponding to $T_{avg} = 60^\circ\text{C}$. (b) Experimental and fitted temperature profiles of the nichrome wire at all power levels (best fit: $kw = 10.9 \text{ Wm}^{-1}\text{K}^{-1}$). The error in experimental temperature data is smaller than the size of the data points shown (in the range of ± 0.5 - 0.9°C depending on temperature).	47
Figure 3.4: Temperature profile in the sample for several different assumed sample thermal conductivities when radiation losses in the sample region are included (sample width = 2 mm, sample thickness = 650 μm , emissivity = 0.6, $T_b = 40^\circ\text{C}$, and $T_L = 24^\circ\text{C}$).	53
Figure 3.5: Heat flux as a function of the sample temperature gradients for a validation experiment using a nichrome wire as the sample. The best-fit “sample” wire thermal conductivity is $kw = 11.8 \text{ Wm}^{-1}\text{K}^{-1}$	55
Figure 3.6: (a) IR temperature map of the experiment with the HDPE sample at an input electrical current of 240 mA. Experimental and modeled temperature profiles of the (b) wire in the suspended region and (c) the HDPE sample including radiation losses from the sample.....	55
Figure 3.7: Sensitivity analysis of experimental and modeling input parameters for the validation experiment with the nichrome wire reference sample. Each parameter is varied by its uncertainty amount and the resulting absolute change in thermal conductivity, Δk is shown in the vertical axis.	59
Figure 4.1: (a) Overview of the procedure for construction of plain-weave fabrics from flat yarn (Dyneema). Photographs of the (b) flat yarn (as received) with loosely bound individual fibers and (c) a woven fabric prototype sample when held in the miniature loom with warp and weft directions	

identified. (d) Top-view photograph of the woven fabric with inset showing optical microscope images of portions of the weave at high magnification. The weft yarn number density is 4-5 times higher compared to that of the warp yarns resulting in a weft-faced plain-weave pattern in which the warp is almost completely covered by the weft. Thermal characterization is conducted along the high density weft yarn direction.62

Figure 4.2: (a) IR temperature map of the wire–yarn experiment at a current input of 220 mA. Temperatures shown are based on corresponding emissivity values of the nichrome wire and the yarn, within the regions as indicated. (b) The corresponding temperature profiles used to extract the heat rates and sample temperature gradients are also shown. Representative error bars in the experimental temperature data are shown in cyan near the center of each profile. (c) Heat flux as a function of sample temperature gradient at different levels of input current for two different yarn samples. The slope of the linear fit across all power levels yields the thermal conductivity of the yarn sample. Error bars indicate the calculated uncertainty in heat flux and temperature gradient. Note that uncertainty in the sample temperature gradient is smaller than the data point width. ...64

Figure 4.3: (a) Representative *in situ* IR images of yarns in the experimental setup at two different twist levels characterized by a surface helix angle of $\sim 8^\circ$ (low twist) and $\sim 30^\circ$ (high twist). (b) Thermal conductance (product of yarn thermal conductivity and cross-sectional area, $kyAy$) measured as a function of surface helix angle of the yarn. Variation of thermal conductance with twist is not very significant ($<6\%$) for the range of twist levels evaluated.66

Figure 4.4: Schematic of the experimental configuration used for the thermal measurements for the woven fabric sample.68

Figure 4.5: (a) IR temperature map of the wire–fabric experiment at a current input of 300 mA. Temperatures shown are based on corresponding emissivity values of the nichrome wire and the fabric, within the regions as indicated, and (b) the corresponding temperature profiles. Representative error bars in the experimental temperature data are shown in cyan near the center of each profile. (c) Heat flux as a function of sample temperature gradient at different levels of input current for different experimental trials: Run 1 is performed with the thermal gap pad between the wire and fabric for enhanced thermal contact, while Run 2 is performed without this pad. The slopes of the linear fit from both runs are extracted to calculate an average fabric thermal conductivity of $\sim 9.5 \pm 0.6 \text{ Wm}^{-1}\text{K}^{-1}$68

Figure 4.6: (a) Schematic drawing (top-view) of a plain-weave fabric showing the heat transfer nodal-network associated with the reduced-order model to calculate the effective thermal conductivity of the fabric in the y direction (along the blue yarns). The neighboring nodes associated with a node ‘P’ on a particular blue yarn are also shown in the inset to illustrate node connectivity. (b) Schematic drawings of the plain-weave fabric cross-section, showing only the blue yarns that participate in heat conduction. These drawings illustrate the effective area-based packing fraction for a loose fabric ($ly/dy = 1$) as compared to a tight fabric ($ly/dy = 0.5$). (c) Effective thermal conductivity as a function of ly/dy as predicted by the reduced order model. The measured fabric thermal conductivity from the experiments is shown as a ‘star’ symbol and agrees well with the prediction from the reduced-order model.71

Figure 4.7: (a) Representative experimental and filtered (based on a moving average) temperature profiles of the nichrome wire at an electrical power input of 14 mW. The peak-to-peak distance, lp is shown, which is used to extract the heat rate entering the fiber, and (b) corresponding

experimental temperature profiles and linear-fits of the two sides of the fiber sample. (c) Heat flux as a function of the sample temperature gradient. The linear fit across power levels yields fiber thermal conductivity. 74

Figure 4.8: Measured thermal diffusivity as a function of temperature amplitude as a result of different levels of electric current supplied to the heater wire. The dashed lines show a comparison from two other references ([41], [46]) based on the extracted thermal diffusivity (from measured thermal conductivity) using standard values of density and heat capacity for UHMW-PE. 76

Figure 4.9: (a) Thermal conductivity of various forms of UHMW-PE measured in the literature and the present study. The thermal conductivity for each material is reported using a bar along the horizontal axis scale, with bars organized into groups of similar form and groups shown in order of increasing length scale. Details of the materials are listed in (b). 78

Figure 5.1: Elastic modulus and thermal conductivity of conventional polymer fibers (in blue) and commercially produced high-performance polymer fibers (in red). The high-performance polymer fibers typically have ~1-2 orders of magnitude higher thermal conductivity and elastic modulus (note the log scales). Data compiled from references with details for the high-performance fibers summarized in Table 5.1. 82

Figure 5.2: Representative schematics of the commercial Dyneema® fabric samples: (a) the Dyneema® denim fabric weave structure consisting of Dyneema® and cotton yarns, with optical micrographs of the Dyneema® and cotton faces for the Dyneema® Black fabric shown as an example. (b) the Composite Dyneema® fabric sample consisting of a grid of Dyneema® fibers sandwiched between polymer films, with a polyester weave attached on one face. 85

Figure 5.3: (a) Schematic representation of the thermal metrology setup showing a heating wire orthogonally oriented in contact with the test sample to be measured (left). Representative temperature profiles of the wire and sample shown (right) are captured using an infrared microscope. Heat rates (Q_l and Q_r) are determined from the wire temperature profile, and the temperature gradients (dT/dy_T and dT/dy_B) in the sample are used to calculate the sample thermal conductivity k_s . (b) Illustration of the principle of the bend testing metrology, where the overhang length L and bending angle θ of a fabric under its own weight enables quantification of the bending stiffness. 87

Figure 5.4: Representative temperature profiles of (a) the heating wire and (b) fabric sample obtained from IR thermal measurements of the Dyneema® BW and EeonTex® samples at the same electrical power input. The Dyneema® BW sample exhibits significantly lower wire and sample temperatures, a steeper temperature gradient in the wire approaching the central region, and a relatively more linear sample temperature profile, which all are indicative of a higher in-plane thermal conductivity. (c) Measured effective in-plane thermal conductivity for the different samples. 90

Figure 5.5: (a) Photograph of three different fabrics bending under their own weight. The stiff HDPE sheet does not visibly bend under its own weight, the Dyneema® Black fabric is much more flexible as seen from its extent of bending, and the 100% Dyneema® lies in between. (b) Measured average bending stiffness (flexural rigidity) based on the described bend testing metrology. 91

Figure 5.6: (a) Schematic diagram showing the top-view of the testing configuration to assess impact of creasing on thermal performance. The fabric sample is creased by bending by 180° at a

specific location as indicated, and infrared temperature maps are captured before and after creasing. (b) Steady state temperature profile as a function of distance from the heater wire on the creased side of the fabric swatch, shown for increasing number of crease cycles and after scoring. The temperature profiles indicate no significant change in heat spreading properties except for the extreme scenario of scoring to purposely damage the individual yarns.93

Figure 5.7: Thermal conductivity versus flexibility (inverse of bending stiffness) for different materials. The materials shown in shades of red (top left) are conventional heat spreaders and possess low flexibility, while those shown in shades of blue (bottom center-right) represent conventional polymer and fabric materials with high flexibility and low thermal conductivity. Dyneema® fabrics (stars) break the trend by demonstrating significantly higher thermal conductivity relative to polymers, while retaining good mechanical flexibility. Data for standard materials (not characterized in this study) taken from references ^{144–148}.97

Figure 6.1: (a) Schematic of the experimental setup of the Laser-Angstrom method. A periodic heat input is supplied to the center of the bottom surface of a sample using a laser source and transient temperature movies of the top surface are captured using an IR microscope lens. (b) Illustration of amplitude of temperature oscillations at three different points away from the location of laser heat input. The quasi-steady oscillations exhibit decreasing amplitude and increasing phase lag with distance from the center.99

Figure 6.2: Overview of the numerical experiments. (a) Numerical model geometry and boundary conditions simulated in COMSOL Multiphysics. (b) Overall approach illustrating the use of numerical experiments to aid the development of a numerical model for data analysis101

Figure 6.3: Representative analysis of numerical simulations for an in-plane anisotropic sample with $k_x = 2 \text{ Wm}^{-1}\text{K}^{-1}$ and $k_y = 6 \text{ Wm}^{-1}\text{K}^{-1}$ depicting the (a) simulated top surface temperature map at a given time instant at quasi-steady state with the evolution of temperature with time for two specific points plotted in (b). The extracted contour maps of k_x and k_y obtained individually at each point are plotted (c) and (d) respectively. The red-dashed circles indicate the inner and outer boundaries representing the edge of the metal tape disc and the edge of the heat sink.....109

Figure 6.4: Representative analysis of numerical simulations for an in-plane isotropic sample with $k_x = 2 \text{ Wm}^{-1}\text{K}^{-1}$ and $k_y = 2 \text{ Wm}^{-1}\text{K}^{-1}$ depicting the (a) simulated top surface temperature map at a given time instant at quasi-steady state with the evolution of temperature with time at the indicated point plotted in (b). The extracted contour maps of k_x and k_y obtained individually at each point are plotted (c) and (d) respectively. The red-dashed circles indicate the inner and outer boundaries representing the edge of the metal tape disc and the edge of the heat sink110

Figure 6.5: (a) The temperature amplitude and phase lag as a function of radial distance from the edge of the metal tape disc averaged over 360° for the case of the in-plane isotropic sample with $k_x = 2 \text{ Wm}^{-1}\text{K}^{-1}$ and $k_y = 2 \text{ Wm}^{-1}\text{K}^{-1}$. The data from the indicated fitting region is used to fit for the thermal conductivity of the sample as shown in (b) along with 10% sensitivity bounds. A fitted conductivity of $1.995 \text{ Wm}^{-1}\text{K}^{-1}$ is obtained which agrees well with the input value of $2 \text{ Wm}^{-1}\text{K}^{-1}$ 112

Figure 6.6: (a) Illustration of periodic heating frequency bounds depending on the in-plane and through-plane thermal conductivity of a sample at a fixed value of thickness and outer radius of the experimental setup. An example case corresponding to $k_x, y = 4 \text{ Wm}^{-1}\text{K}^{-1}$ and $k_z = 0.5 \text{ Wm}^{-1}\text{K}^{-1}$ is shown.113

$^1\text{K}^{-1}$ is depicted as indicated by the pair of ‘X’ points. A typical frequency choice (25 mHz) for measurement in this case is indicated. (b) Input and predicted thermal conductivities along the x and y orthotropic directions demonstrating the applicability of the proposed measurement method across a wide range of thermal conductivity values.115

Figure 6.7: Representative IR temperature maps at quasi-steady state for (a) HDPE sheet, and (b) Dyneema Black fabric under periodic heating frequencies of 25 mHz and 100 mHz respectively using a laser heat source. The circular isotherms in the case of the isotropic HDPE sheet and the elliptical isotherms in the case of the Dyneema fabric demonstrate that the intrinsic in-plane anisotropy of the sample can be captured experimentally.118

ABSTRACT

Recent technological advances in the field of electronics and the accompanying trend of device miniaturization with enhanced functionality has led to growing interest in new methods of electronic device integration. As a result, flexible, wearable, and portable electronic devices have emerged as a way of providing a multifunctional infrastructure to facilitate various consumer needs, creating new challenges for materials development. Polymers possess a unique combination of desirable properties such as mechanical compliance, durability, low density and chemical stability which makes them ideally suitable as substrate materials to cater to such diverse applications. However, the low thermal conductivity of polymers hinders their heat spreading capability in thermal management applications for flexible and wearable devices. In recent years, there has been a growing interest in ultra-high molecular weight polyethylene (UHMW-PE) materials with aligned polymer chains due to their remarkably high thermal conductivity that is similar to some metals. These are commercially manufactured in large volumes as fibers using gel-spinning and ultra-drawing processes that impart a high degree of crystallinity and orientation to the polymer chains. As a result, these materials develop exceptionally high mechanical strength, elastic modulus, and thermal conductivity compared to conventional polymers. Therefore, UHMW-PE materials have found applications in commercial products like motorcycle gear and ballistic vests, but have not been commercially deployed for heat spreading and thermal management applications. While there has been much fundamental work on the development of high thermal conductivity fibers, effective translation of the high conductivity from individual fibers to macroscale (wearable) flexible fabrics has not been previously explored. The objective of this thesis is to obtain a fundamental understanding of the thermal transport properties of fabric materials constructed from

the high conductivity polymer fibers, and assess their applicability for potential heat spreading applications.

In the present work, commercially available high thermal conductivity fibers made of UHMW-PE are utilized to fabricate plain-weave fabrics prototypes, and the thermal properties of individual fibers, yarns, and woven fabrics are measured using a novel in-plane thermal measurement method. The characterization technique leverages infrared (IR) microscopy for a non-contact temperature sensing and is generally scalable for thermal characterization of the in-plane thermal-conductivity of materials across different length scales. Effective thermal conductivities on the order of $\sim 10 \text{ Wm}^{-1}\text{K}^{-1}$ are achieved along the in-plane dominant heat transport direction of the woven fabric, which is exceptionally high ($\sim 2\text{-}3$ orders of magnitude) compared to conventional clothing and textile-based materials. The thermal conductivity and mechanical flexibility of the UHMW-PE fabrics are benchmarked with respect to conventional materials and the effect of bend-stressing and thermal annealing of the fabrics is characterized using the developed metrology.

Additionally, a laser-based IR thermal metrology technique leveraging both non-contact heating and temperature sensing is conceptualized and validated using a numerical thermal modeling approach. The proposed technique provides an approach to estimate the in-plane heat spreading properties of anisotropic materials with direction-dependent thermal properties based on quantifying the surface temperature map of a sample subjected to periodic heating. Numerical simulations are leveraged to demonstrate the applicability of this method to enable measurement of a wide range of thermal properties indicating great potential to develop this further as a standardized robust method for in-plane anisotropic thermal characterization of materials such as fabrics and films.

This work sheds light on the high thermal conductivity of UHMW-PE materials that can be achieved using a scalable manufacturing process and describes the thermal metrology approaches to enable their characterization, thereby providing a foundation for the conceptualization and design of flexible substrate based thermal solutions in future wearable/flexible electronic devices.

CHAPTER 1. INTRODUCTION

1.1 Motivation and Background¹

Rapid advances in electronic device technology over the past decade have led to significant expansion of the field of flexible and wearable electronics ¹⁻⁵. The opportunity to integrate information processing and artificial intelligence into clothing and textiles to facilitate various consumer needs has resulted in next-generation interactive multifunctional devices as part of a wearable infrastructure ^{6,7}. Electronic devices have transformed from large, bulky systems to portable, thin, flexible systems over a very short period of time ⁸. This has also sparked both research and consumer interest in flexible and wearable products such as smart textiles, wearable/portable displays, high-performance sportswear with embedded sensors, and wearable health monitoring systems ^{9,10}. Such applications pose materials development and design challenges in order to realize electronic functionality in soft, flexible, and lightweight devices ^{2,11}.

Lightweight, soft, durable, and low-cost polymers have been commonly used as a material in various flexible device applications ¹². Being mechanically pliable and compliant, they are ideally suited as substrate materials. Recent studies have demonstrated various approaches for producing electrically conductive textiles and fabrics – typically either by deploying intrinsically conductive polymers (such as polypyrrole and polyaniline) as the constituent fibers¹³⁻¹⁵, or by constructing conductive polymer composites or fabrics using electrically conductive fillers or coatings ^{11,16}. Alternatively, electrically conductive components/devices are attached to conventional (electrically insulating) polymer substrates such as polycarbonate ¹⁷, polyimide ¹⁸, polyethylene terephthalate ¹⁹ and polyether sulfone ²⁰. In this case, heat removal is limited by the

¹ Portions of this section are reproduced from our work, Candadai *et. al* ¹¹⁰

low thermal conductivity polymers and becomes a crucial concern for device reliability and performance ²¹. Additionally, the miniaturization of electronic devices accompanied by changes in chip architecture lead to spatially non-uniform power dissipation and concentration of heat in localized regions called hotspots where temperatures can be significantly higher than average die surface temperatures ²². Although flexible and wearable electronic devices typically operate at low power, effective spreading of the heat generated in these devices is required to meet thermal design constraints driven by ergonomic considerations, namely that the surface of the device must be at a safe temperature to touch ^{8,23}.

The ability to spread heat is primarily dependent on the thermal conductivity of a material. Materials with a high thermal conductivity such as metals (typically $\sim 100 \text{ Wm}^{-1}\text{K}^{-1}$) are considered as good heat spreaders. However, the thermal conductivity of conventional polymer materials is very low (on the order of $0.1\text{-}0.5 \text{ Wm}^{-1}\text{K}^{-1}$) ²⁴⁻²⁷, which poses a severe challenge for heat dissipation applications in flexible and wearable electronics. Traditional approaches to enhance the thermal conductivity of polymers involve introduction of high conductivity fillers such as metals and carbon-based materials in the polymer matrix ²⁸⁻³¹. These methodologies are generally limited by the ability to maximize thermally conductive pathways in the material and achieve low thermal percolation thresholds in the polymer-filler composites ^{32,33}. There are also concerns related to flexibility and other mechanical properties of the composites being affected due to the introduction of the filler materials potentially hindering flexible device applications ²¹. A second route that has been explored to improve the thermal properties of polymers is focused on enhancing their intrinsic thermal conductivity using alignment and orientation of the polymeric chains ³⁴⁻³⁶. This method has shown great promise in significantly increasing the thermal conductivity of linear polymers such as polyethylene ³⁷.

Gel-spun, ultra-high molecular weight polyethylene (UHMW-PE) fibers produced via molecular chain alignment techniques have two orders of magnitude higher thermal conductivity as compared to that of bulk polyethylene^{38–40}. Recent studies exploring the thermal properties of individual microscale and nanoscale fibers, as well as ultra-drawn thin films made of UHMW-PE, have demonstrated thermal conductivities on the order of 10-100 Wm⁻¹K⁻¹ depending on the material form factor and length scale^{36,41–43}. Also, high thermal conductivity UHMW-PE strands are already manufactured commercially for use in lightweight armors and motorcycle gear owing to their mechanical strength. However, the thermal properties of macroscale substrates such as woven fabrics constructed from these high thermal conductivity fibers are yet unexplored.

Construction of fabrics from UHMW-PE fibers is very promising for flexible and wearable device applications as textile manufacturing processes are scalable to large areas and high volumes. But scaling up of the material from individual microfibers to yarns and ultimately to fabrics leads to a material that is not fully-dense while introducing numerous material interfaces and associated thermal resistances, all of which play a critical role in determining the effective heat transfer behavior. Thus, a systematic study of the effective thermal conductivity of UHMW-PE spanning across these different forms and length scales is crucial to understanding and assessing the potential of fabrics for thermal management applications.

UHMW-PE fibers are intrinsically anisotropic due to the nature of the manufacturing processes used for their production. Fabrics constructed from these fibers can potentially exhibit anisotropic thermal behavior along all three primary orthotropic directions depending on the different types of fibers used and the weave patterns employed. Therefore, suitable thermal metrology techniques must be developed to enable characterization of thermal properties across these forms and length scales. Though various conventional methods exist for thermal conductivity

measurement, they cannot be easily translated to allow such multi-scale characterization and there is great potential to augment these methods by leveraging non-contact temperature measurement methods.

1.2 Objectives and Major Contributions

The primary objective of this thesis is to understand the thermal transport properties of materials assembled from molecularly aligned polymers across different forms and length-scales, develop associated metrology techniques to enable thermal characterization, and assess the potential of such high-performance polymers for thermal management applications in flexible and wearable device platforms. The present work includes development of novel experimental methods and modeling analysis to enable an improved understanding of the thermomechanical properties of thermally conductive fibers and fabrics. Specifically, this work investigates the thermal properties of gel-spun ultra-high molecular weight polyethylene as it is scaled up from individual ultra-drawn fibers to macroscale woven fabrics that are of practical interest for wearable and flexible device applications. Further, a basic understanding of the bending behavior of the fabrics, and the effect of bend stressing and thermal annealing on the effective thermal properties of the fabrics is also developed. Additionally, a non-contact metrology technique to enable anisotropic characterization of thermal properties and device-level performance is demonstrated. Specific contributions of this work include:

- 1) Synthesis of current state of the art literature for both high thermal conductivity fiber materials and characterization methodologies
- 2) Conceptualization and development of a steady-state thermal measurement technique based on infrared thermography (IR) tools and associated modeling analysis to enable in-plane thermal property measurements

- 3) Demonstration of a woven fabric sample prototype constructed from twisted polymer yarns with high in-plane thermal conductivity
- 4) Design and implementation of bend testing metrologies to characterize fabric stiffness as a measure of mechanical flexibility; providing reliability characterization data of fabric thermal properties as a function of bend stressing (creasing) and thermal annealing
- 5) Development of transient IR thermal metrology based on laser heating to enable characterization of the in-plane thermal anisotropy of materials and simultaneous assessment of device-level performance
- 6) Demonstration and validation of the proposed experimental methodology using thermal modeling by leveraging numerical experiments

1.3 Outline of the Document

This document is organized into five chapters. *Chapter 1* included the motivation and background for this work, and introduced the major objectives and tasks that will be accomplished as part of this thesis. *Chapter 2* summarizes the relevant background literature associated with this study covering both the material science and heat transfer aspects. This includes a summary of the manufacturing techniques used to produce high thermal conductivity polymer fibers, a description of general thermal characterization techniques, followed by a summary of prior thermal literature on UHMW-PE. *Chapter 3* introduces a thermal characterization technique (steady-state) based on IR microscopy and the associated heat transfer model that were developed to enable in-plane thermal conductivity measurements. *Chapter 4* presents results on experimental thermal characterization of UHMW-PE fibers, yarns, and woven fabrics, and also provides a description of the reduced-order thermal model that is used to predict the effective thermal conductivity of fabrics. *Chapter 5* describes the thermal and mechanical characterization of UHMW-PE fabrics

and other conventional alternatives to assess the potential of these materials for wearable device applications. *Chapter 6* introduces a thermal characterization technique (transient) based on laser-heating and IR microscopy and discusses numerical simulations to demonstrate the measurement of in-plane thermal anisotropy of materials. Finally, *Chapter 7* contains the major conclusions of this thesis study and discusses potential avenues for future work in this area.

CHAPTER 2. LITERATURE REVIEW

This chapter reviews relevant background literature and presents an overview of the material and thermal science fundamentals related to the present study. The chapter is organized into three sections: Section 2.1 presents an overview of gel-spinning processes and description of process parameters that influence the final structure and thermal properties of UHMW-PE fibers. Section 2.2 presents an overview of the heat transfer fundamentals and general thermal conductivity measurement techniques. Section 2.3 reviews thermal characterization studies on high thermal conductivity UHMW-PE materials as a background for the chapters to follow.

2.1 Gel-Spun High-Performance Polyethylene Fibers

Polymer fibers are manufactured using a technique known as fiber spinning during which the polymer is converted into a fluid state either by melting or by dissolution in a solvent. This process is a modified form of extrusion, since the molten polymer is extruded through a spinneret, and is allowed to cool to a rubbery state and ultimately solidifies resulting in the formation of multiple continuous filaments ⁴⁴.

Gel spinning is being widely used today to produce high-performance polyethylene (PE) fibers characterized by very high strength and elastic modulus ⁴⁵. In this process, fibers are extruded in a gel-like, partially liquid state that keeps the polymer chains bound together. These fibers exhibit tensile strengths as high as 4 GPa ⁴⁶ and tensile moduli as high as 130 GPa ⁴⁷. Widely available UHMW-PE fibers are produced under the trade names of *Dyneema* and *Spectra*. They are made strong by stretching and orienting the molecular chains resulting in their high crystallinity (up to 85%). Such high degrees of extension and macromolecular orientation (up to 95%) are achieved by using a high extent of drawing (super-drawing or ultra-drawing) made possible by the

low degree of entanglement of the gel-spun material ⁴⁵. The high draw ratio used in this technique is the key to achieving unique mechanical and thermal properties. As a result, various studies in the literature are dedicated to investigating the effect of draw ratio and changes in processing parameters on the obtained mechanical and thermal properties ^{48,49}.

In the following sections, the processing details of the gel-spinning technique used to produce high modulus PE fibers are described. Further, the thermal aspects of processing and the conditions needed to produce high thermal conductivity fibers are emphasized. Finally, important considerations in thermal conductivity models that relate final thermal properties to draw ratio are discussed.

2.1.1 Gel Spinning Process

The concept of gel-spinning was inspired by the observations of Kennings and Peller ⁵⁰ who successfully demonstrated the production of continuous filaments using a surface spinning growth technique in a Couette-type apparatus shown in Figure 2.1a ⁵¹. They observed gel formation with very low entanglements leading to crystalline PE fibrils being formed on the surface.

The gel-spinning process was first developed by Smith and Lemstra (DSM) ^{52,53}. Figure 2.1b shows a schematic of their very first gel-spinning experiments. This setup was used to spin very high molecular weight PE filaments resulting in the formation of a highly viscous solution which is pumped through capillaries with diameter of the order of 1 mm. The spun liquid filaments are passed through a cold-water quenching bath to form a gel fiber, which is subsequently super-drawn in an oven circulated with hot air at 120°C at a strain rate of 1/sec. The final product is a highly oriented polyethylene fiber with unique mechanical and thermal properties.

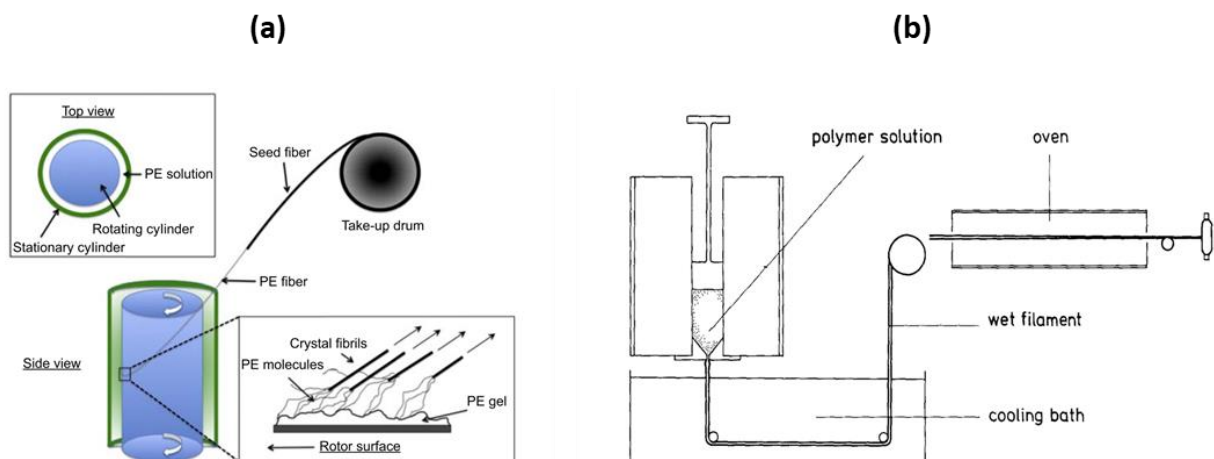


Figure 2.1: Schematic representation of (a) the surface spinning technique (reproduced from [51]); and (b) the gel-spinning and drawing process (reproduced from [52])

2.1.2 Desirable Process Parameters

- 1) Starting Polymer: The most common starting polymer for gel spinning processes to produce high performance fibers is PE because of its high intrinsic modulus, crystallinity and tenacity in a simple planar zig-zag structure. Molecular weight (greater than 1 million g/mol) and molecular weight distribution are important parameters that determine the performance of the final fiber. Very short chains will result in low strength fibers and very long chains can constrain the drawing process; achieving a good balance between the two is crucial ⁴⁵.
- 2) Spinning solution: An important aspect of the gel spinning process is the use of a dilute solution for fiber spinning in order to obtain a desirable amount of entanglements in the solution. The entanglement density is directly proportional to the concentration of the polymer and impacts its drawability. Melts or high concentration solutions have a very high entanglement density and as a result can be drawn to only about 5 times. On the other hand, a very dilute solution with low entanglement density makes it difficult to transfer tensile stress between molecules

and can lead to breakage of the gel fiber. Therefore, control of the entanglement density an important aspect and a semi-dilute polymer solution followed by gel formation after spinning leads to an ideal structure ⁵⁴ as illustrated in Figure 2.2a.

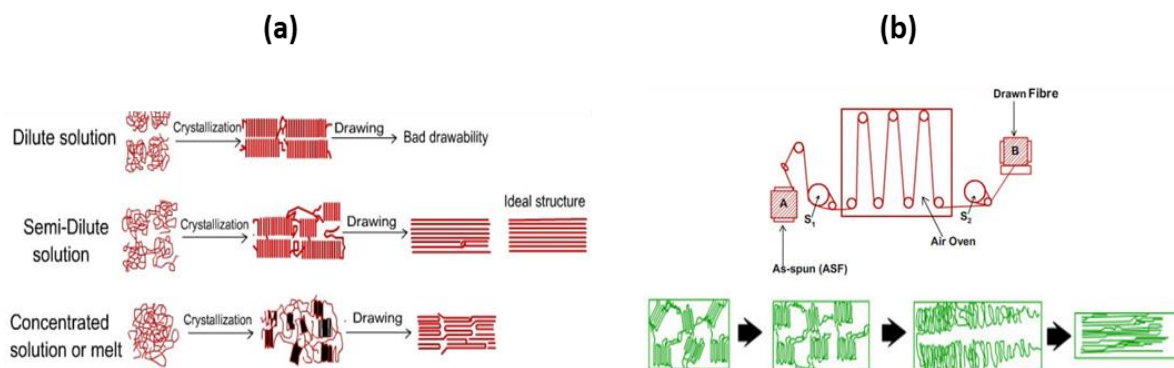


Figure 2.2: (a) Illustration of solution concentration affecting entanglement density and drawability. (b) Schematic of the drawing process and its physical effect on the polymer molecular chains. These figures have been reproduced from [55].

- 3) **Drawing:** The super-drawing stage of the gel spinning process has the most significant impact on the properties of the final product as the mechanical and thermal properties are directly related to the draw ratio. A schematic of a typical drawing process is shown in Fig. Figure 2.2b. The drawing process enables conversion of the random crystals and a major portion of the non-crystalline material by chain unfolding, resulting in the formation of oriented microfibrils ^{55,56}.

A greater degree of drawing of high molecular weight PE leads to higher orientation and therefore to a higher axial thermal conductivity. Studies have shown that, in addition to entanglement density, the temperature during the drawing process also greatly dictates the draw ratios that can be achieved. The optimum drawing temperatures are generally greater than 110°C, because the alpha relaxation of the PE molecules in the crystalline phase is thermally

activated at this temperature which allows for unfolding of polymer chains and promotes the growth of oriented microfibrils ^{49,57}.

Smith and Lemstra ⁵⁸ observed that fibers that were dried at room temperature after spinning to completely remove the solvent showed an increasing trend of maximum draw ratio with drawing temperature. On the other hand, wet fibers that were drawn immediately after spinning exhibited a maximum draw ratio for a given optimum temperature (around 110°C). However, the maximum possible draw ratios achieved for the wet gel-fibers in the temperature range of 90°C to 125°C were seen to be substantially higher. For wet gel fibers, the higher drawing ratios attainable at these temperatures is because the solvent has a plasticizing effect during drawing, whereas the rapid decrease in maximum draw ratios at higher temperatures can be attributed to lack of strength of the gels due to dissolution at these temperatures.

2.1.3 Thermal Conductivity Dependence on Draw Ratio

The axial thermal conductivity of PE increases with draw ratio and the transverse thermal conductivity decreases with draw ratio. This has been illustrated by Choy et al. ⁵⁹. Different models have been developed that aim to predict the variation of thermal conductivity with draw ratio based on the changes associated with polymer chain orientation and crystallinity.

In one of the early two-phase models proposed by Choy and Young ⁶⁰, a semi-crystalline polymer is treated as a combination of an amorphous medium of isotropic thermal conductivity, and a crystalline medium consisting of spherical crystallites with anisotropic thermal conductivity. This model quantifies the increase in thermal conductivity along the drawn direction by considering the effect of increased orientation of the polymer chains in the crystalline phase. In general, the model significantly under-predicts measured thermal conductivity data for higher

draw ratios because it does not consider the increase in crystallinity that can occur during orientation of the polymer chains due to morphological changes at these high draw ratios.

The Takayanagi model^{59,61,62} accounts for the morphological changes caused at higher draw ratios (>6) and is able to predict the thermal conductivity variation where the Choy and Young model breaks down. This model incorporates the increase in the crystallinity fraction by considering the formation of inter-crystalline bridges or taut tie molecules of high thermal conductance that connect the folded-chain crystalline blocks. Here, the polymer is considered as a network with a series combination of folded chain crystalline blocks and the amorphous region as the matrix phase, which is in parallel with the extended chain crystalline fiber phase. This model can therefore predict experimental results obtained for gel-spun UHMWPE fibers such as Dyneema and Spectra that undergo ultra-drawing and exhibit thermal conductivities in the range of $\sim 20\text{--}30 \text{ Wm}^{-1}\text{K}^{-1}$, provided the variation of the crystallite fractions can be accurately predicted.

More recent experimental studies demonstrating very high thermal conductivity for oriented UHMW-PE^{36,43} at extremely high draw ratios cannot be predicted using the described conventional thermal models considering changes in crystallinity and orientation of the molecular chains in the crystalline phase, as these indicate a saturation of thermal conductivity. Recent work⁴³ has shown that such observations can only be accurately corroborated by models that consider the role of the amorphous region at very high draw ratios. Very high levels of drawing result in some degree of orientation and order in the amorphous region which plays a key role in estimating thermal conductivity in these situations.

2.2 General Thermal Characterization Methods²

Thermal conductivity is the thermal transport property that determines the rate of conduction heat transfer in a given material and is defined based on Fourier's law of heat conduction ⁶³. The thermal energy flux (Wm^{-2}) at a given location in a material is proportional to the temperature gradient (Km^{-1}) at that location, and the constant of proportionality is defined as the material thermal conductivity (with units of $\text{Wm}^{-1}\text{K}^{-1}$). Thermal conductivity values for materials can span several orders of magnitude ranging from $\sim 0.1 \text{ Wm}^{-1}\text{K}^{-1}$ for polymers to $\sim 1000 \text{ Wm}^{-1}\text{K}^{-1}$ for hard crystalline materials such as diamond ⁶⁴. The knowledge of the thermal conductivity of a material is crucial for design of thermal engineering systems. In this section, the general categories of thermal measurement techniques are briefly reviewed in order to provide an understanding of the fundamentals, concepts, and experimental considerations involved in thermal characterization systems which will lay a foundation for the chapters to follow. A summary of this review is also provided in Table 2.1.

2.2.1 Steady State Methods

This category of measurement methods involves direct measurement of the thermal conductivity of a material without prior knowledge of other thermal transport properties. In these methods, the measurements are performed under a steady state temperature distribution of the system with no temperature variations with respect to time. Steady state methods can broadly be classified into three categories: absolute techniques, comparative techniques, and differential techniques ⁶⁵.

² Portions of this section are reproduced from our work, Candadai *et. al* ¹¹²

2.2.1.1 Absolute Techniques

In this set of techniques, described in Table 2.1, a measurable temperature gradient (dT/dx) is established across the sample of interest (oriented along the x direction) and the heat flowing through the sample (Q) is measured. The thermal conductivity (k) can then be determined by Fourier's law using $k = \frac{|Q|}{A} \left| \frac{dT}{dx} \right|$, where A is the sample cross-sectional area normal to the heat flow direction. A commonly used test setup that employs the absolute technique is the guarded-hot-plate apparatus ⁶⁶. In these techniques, there are several important aspects that need to be considered to obtain an accurate measurement of thermal conductivity. Since all the heat generated by the heat source (*e.g.*, laser-heating source or electrical Joule heating source) does not always completely flow through the sample, accurate measurement of heat flow through the sample and calibration of parasitic heat losses (conductive, convective and radiative) are challenging. In many cases, the experimental measurements may need to be performed in vacuum so as to minimize convection losses from the system that cannot always be accurately modeled ⁶⁷. Further, there may be conduction heat losses through thermocouple wires that are used as temperature sensors, which can cause significant error especially for measurements involving microscale samples. Measurements for such small samples also often require special attention to quantification of sample heat flow during the design and fabrication of specialized thermal characterization devices ^{68–70}.

2.2.1.2 Comparative Techniques

Comparative techniques overcome the main challenge of accurately quantifying the sample heat flow associated with absolute techniques by using a reference sample of known thermal conductivity. This reference sample is connected in series with the target sample, and temperature gradients in both materials are measured as shown in Table 2.1. Since equal amount of heat must

flow through the reference and target samples at steady state, direct measurement of heat flow through the target sample is not required to extract its thermal conductivity⁶⁵. The ASTM E1225 standard⁷¹ is commonly used to measure thermal conductivity using this technique. In these measurements, additional temperature sensors or thermocouples are required to accurately quantify the temperature gradients in the reference and target sample regions, which again presents a challenge for microscale samples. To overcome this challenge, recent work has focused on the development of non-contact temperature measurement techniques such as those based on infrared thermography to create miniaturized versions of established methods and standards that are suitable for measuring thermal conductivity of small length scale samples^{72–75}. An additional consideration in this set of techniques is to ensure proper mechanical attachment of the sample ends to a reference material. In particular, it is difficult to ensure that the interface with the reference sample maintains uniform heat transfer through the cross-section of the target sample, especially for in-plane characterization of cylindrical/rod-like samples such as fibers. Also, reference materials with comparable thermal conductivity to that of the target sample are required to obtain accurate measurements^{65,76}.

2.2.1.3 Differential Techniques

Various types of differential techniques have also been developed to measure the thermal conductivity of small samples to avoid the difficulties associated with temperature and heat flux measurement in systems involving millimeter or smaller scale samples. The parallel conductance method is one such technique in which the thermal conductivity of needle-like samples can be measured by performing two sequential experiments: first with a sample holder placed between hot side and cold side temperature ends; second with the target sample placed parallel to the sample holder between the two ends⁷⁷. This allows for extraction of the sample thermal conductance by

subtracting the effective thermal conductance measured from each experiment (with and without the sample). Other T-type and cross-beam methods are based on a similar principle and involve this two-step measurement approach to extract sample thermal conductivity ⁷⁸⁻⁸¹. However, in most cases, these require precise estimation of thermal contact resistance between the heater wire and the target sample to enable accurate measurement of thermal conductivity.

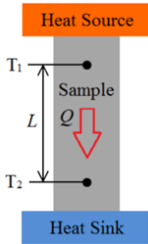
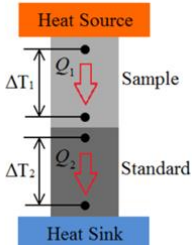
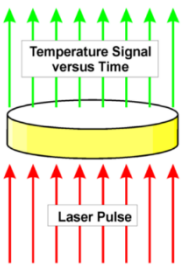
2.2.2 Transient Methods

A variety of transient techniques are commonly utilized to measure thermal conductivity of a material. These methods typically employ pulsed or periodic heat inputs which are used to induce a transient temperature distribution in the target sample and are generally associated with much faster measurement times as compared to steady state methods ⁶⁵. Also, transient methods help overcome some of the limitations associated with steady state techniques such as quantification of heat flow through the sample, heat losses, and thermal contact resistances. Since most transient measurement techniques are associated with complementary transient heat conduction models, thermal diffusivity is the transport property that can be directly extracted from such measurement. Therefore, in many situations, these methods can be restrictive because a priori knowledge of material density and specific heat is required to extract thermal conductivity from thermal diffusivity.

The laser-flash technique is the most widely used transient technique for determining the thermal diffusivity of a material. In this technique, a laser source heats up one face of a planar sample, while a detector captures the time-dependent temperature response on the opposite face of the sample. By fitting the experimental time dependent temperature profile to a transient heat conduction model, the thermal diffusivity of the sample can be obtained ⁸². However, this method

is typically restrictive for measurements of non-homogenous porous samples such as fibrous materials^{83,84}.

Table 2.1: Summary of general thermal measurement techniques

Method	Description
<i>Absolute Techniques</i>	
 <p>Zhao <i>et al.</i>⁶⁵</p>	<ul style="list-style-type: none"> Heat flowing through the sample is directly measured or calculated Generally valid only for very small temperature differences in the sample based on typical assumptions Requires thorough analysis of parasitic conduction losses for microscale samples and/or Differential techniques such as the T-type method involving temperature measurements with and without the sample are also used as an approach to quantify heat flow
<i>Comparative Techniques</i>	
 <p>Zhao <i>et al.</i>⁶⁵</p>	<ul style="list-style-type: none"> Reference sample with known thermal conductivity in series with the sample to be measured is used to quantify heat flow Requires good geometric compatibility and contact between the sample and reference Generally used for through-plane conductivity measurement and challenging for microscale samples for thermocouple contact-based temperature sensing Difficulties associated with maintaining uniform heat transfer at the interface for in-plane characterization
<i>Transient Techniques</i>	
 <p>Taken from ref⁸⁵</p>	<ul style="list-style-type: none"> Typically used to measure thermal diffusivity (α), which is a combination of thermal conductivity, density and specific heat: $k = \alpha \rho C_p$ These methods help overcome some typical challenges such as quantification of heat flow through the sample, heat losses, and thermal contact resistances Commercial methods such as laser-flash analysis typically require homogeneous samples Includes variety of approaches such as Angstrom's method, time-domain thermo-reflectance (TDTR), 3-omega, etc.

Another commonly used transient measurement technique is the Angstrom's method which was introduced in 1863⁸⁶ to measure the thermal diffusivity of a material. This method involves transient heating of one end of a long thin specimen using a periodic heating source. The measurement of the temperature oscillations and the phase delay associated with two different locations on the sample yields the thermal diffusivity of the sample. The analysis involves fitting of the experimental temperature measurements to a one-dimensional heat transfer model to calculate thermal diffusivity. Recent work by Hahn *et al.*⁸⁷ and Hu *et al.*⁸⁸ have focused on making this technique more broadly applicable and diverse with the availability of more data using infrared microscopy-based measurement approaches.

Two other transient measurement techniques that have been developed in recent times are the 3-omega and the time domain thermo-reflectance (TDTR) techniques^{89,90}. These techniques are very useful for determining both cross-plane and in-plane thermal conductivity of very thin film materials (thickness < 100 μm). While the 3-omega method is highly accurate especially for dielectric materials, some of the important considerations include sample preparation, device microfabrication and signal-to-noise ratio concerns. The TDTR method is very versatile in terms of enabling simultaneous measurement of thermal conductivity and interfacial thermal conductance in multi-layer thin films, but the accuracy of the measurement is typically limited due to uncertainties associated with the various model fitting material parameters⁸⁹. This presents additional challenges with respect to increased uncertainty for anisotropic materials with different conductivity values along each of the orthotropic directions due to greater number of model fitting parameters.

2.3 Related Work on High Thermal Conductivity UHMW-PE³

High-performance polymer fibers such as UHMW-PE are now commercially produced in large volume to achieve greatly enhanced mechanical strength and modulus as compared to conventional bulk polymers^{53,91}. As discussed in the previous section, this enhancement is primarily a result of increased crystallinity and orientation which also leads to improved thermal properties. Many studies in the literature have focused on thermal characterization of UHMW-PE materials of different forms such as fibers and thin-films. This section summarizes some of these important studies to provide an understanding of the relevant thermal literature on UHMW-PE.

Thermal characterization studies of UHMW-PE fibers have been largely limited to measurements of individual filaments and fiber-reinforced composites. Choy *et al.*⁶¹ fabricated fiber-reinforced composite sheets having differing fiber volume fractions; low-density PE was reinforced with commercial gel-spun polyethylene fibers (Spectra). The thermal conductivity of the individual fibers was estimated to be $\sim 38 \text{ Wm}^{-1}\text{K}^{-1}$ by extrapolating laser-flash measurements of the composite sheets to a volume fraction of 1. Further, an improvement in fiber axial thermal conductivity of up to a factor of 10 was predicted based on the modeling analysis presented in this work. Wang *et al.*⁴¹ employed time-domain thermorefectance to measure thermal conductivities of different individual microfibers with diameters of 10-30 μm by embedding them in an epoxy matrix. They measured a thermal conductivity of $\sim 15 \text{ Wm}^{-1}\text{K}^{-1}$ for Dyneema fibers, and $\sim 17 \text{ Wm}^{-1}\text{K}^{-1}$ for Spectra fibers. The axial thermal conductivity of the fibers was predicted to be inversely proportional to temperature (near room temperature). Also, their measurements indicated that liquid crystalline polybenzobisoxazole (PBO) fibers, commercially supplied as Zylon, have slightly higher thermal conductivity ($\sim 20 \text{ Wm}^{-1}\text{K}^{-1}$) than UHMW-PE fibers. Liu *et al.*⁹²

³ Portions of this section are reproduced from our work, Candadai *et. al*¹¹⁰

characterized the thermal diffusivity of UHMW-PE microfibers using a transient electrothermal technique. The thermal conductivity of the fibers was measured to be $\sim 23 \text{ Wm}^{-1}\text{K}^{-1}$ by evaluating the volumetric heat capacity of the fibers based on experimental measurements of the fiber crystallinity. A follow-up to this work ⁹² published by Zhu *et al.* ⁹³ reported that the thermal conductivity of these fibers can be enhanced to $\sim 51 \text{ Wm}^{-1}\text{K}^{-1}$ by means of heat stretching. Interestingly, this is accompanied by a slight decrease in crystallinity, and the thermal conductivity enhancement is attributed restructuring of the amorphous phase and alignment of amorphous molecular chains. Ma *et al.* ⁹⁴ measured the thermal conductivity of electro-spun PE nanofibers ($\sim 60 \text{ nm}$ diameter) based on a resistance thermometry technique by suspending the fiber in a microdevice and reported a thermal conductivity of $\sim 9.3 \text{ Wm}^{-1}\text{K}^{-1}$, and attributed the thermal conductivity enhancement to increased orientation and crystallinity induced by the electrospinning process which was corroborated by micro-Raman spectroscopy. More recently, Shen *et al.* ³⁶ used laser-induced heating and AFM cantilever deflection-based temperature sensing to demonstrate that a thermal conductivity of up to $\sim 104 \text{ Wm}^{-1}\text{K}^{-1}$ can be achieved for gel-spun and ultra-drawn PE nanofibers with diameters on the order of $\sim 100 \text{ nm}$. In addition, they also performed molecular dynamics simulations to estimate an upper bound thermal conductivity of $\sim 180 \text{ Wm}^{-1}\text{K}^{-1}$ based on the limit of a single perfect crystal of PE.

Thermal characterization of fiber bundles (yarns) consisting of 6000 monofilaments of commercial UHMW-PE fiber (Dyneema) was performed by Fujishiro *et al.* ^{95,96}. In this study, the authors implemented an absolute technique for thermal conductivity measurement of a fiber bundle by attaching the opposing ends of the bundle to a resistance heater and a refrigerated cold stage. Thermocouples bound by Cu wire were adhered to the bundle using silver paste to measure the temperature difference between two locations. The authors did not characterize parasitic

conduction losses through the attached Cu wires in their experiments, which would possibly lead to an overestimation of thermal conductivity in their measurements. A transient technique was also used to separately measure the thermal diffusivity of the yarns. Thermal conductivities of up to $60 \text{ Wm}^{-1}\text{K}^{-1}$ were reported for these yarns at temperatures below 260 K. The thermal conductivity of yarns was observed to increase with temperature, and an anisotropic ratio (ratio of thermal conductivity in axial to transverse direction) in the range of 10-30 was observed in the range of 10 K to 260 K.

In other recently reported studies by Ghasemi *et al.*⁴², Xu *et al.*⁴³, and Ronca *et al.*⁹⁷, ultra-oriented, thin PE films ($\sim 1\text{-}10 \text{ }\mu\text{m}$) have been fabricated using very high draw ratios to achieve thermal conductivities of $16\text{-}65 \text{ Wm}^{-1}\text{K}^{-1}$. Ghasemi *et al.*⁴² used a sol-gel based fabrication approach followed by ultra-drawing and mechanical stretching at high temperatures to fabricate thin films ($4\text{-}10 \text{ }\mu\text{m}$) with crystallinity of $\sim 99\%$ and a thermal conductivity of up to $\sim 16 \text{ Wm}^{-1}\text{K}^{-1}$ at high draw ratios. The thermal diffusivity of the films was measured using a transient technique (Angstrom's method), and the thermal conductivity was extracted using theoretical values of density and specific heat. Ronca *et al.*⁹⁷ used a solid state, solvent-free process to synthesize UHMW-PE and subjected the produced samples to a two-step rolling and stretching process to produce films with a high degree of orientation. An in-plane laser flash measurement technique is used to measure the thermal diffusivity of the stretched films, and the thermal conductivity is extracted from bulk values of density and specific heat. A thermal conductivity of $\sim 65 \text{ Wm}^{-1}\text{K}^{-1}$ is achieved for relatively higher molecular weight UHMW-PE at the highest draw ratio. Xu *et al.*⁴³ performed a similar study on ultra-drawn films at high draw ratios produced from commercial semi-crystalline PE powder subjected to solvent based extrusion followed by mechanical drawing in a scalable roll-to-roll manufacturing platform⁹⁸. Thermal conductivity was measured as a

function of draw ratio using a steady state measurement method, and values of up to $62 \text{ Wm}^{-1}\text{K}^{-1}$ were reported at the highest draw ratio with a final drawn film thickness of $\sim 1 \text{ }\mu\text{m}$. The authors also demonstrated that the manufacturing process aligned the amorphous polymer chains in the material resulting in an amorphous phase thermal conductivity of $\sim 16 \text{ Wm}^{-1}\text{K}^{-1}$ at the highest draw ratio, which was separately extracted using model-based fitting of small-angle X-ray scattering measurements. This is a remarkable fraction ($\sim 25\%$) of the total film thermal conductivity contributed by the amorphous phase, which shows great potential for engineering the intrinsic molecular structure of polymers to obtain even further enhancement in the thermal conductivity of UHMW-PE.

2.4 Related work on high-performance fabrics⁴

Many studies have focused on developing and characterizing the properties of thermoregulation textiles based on moisture wicking^{99,100}, liquid cooling^{101–103}, and radiation cooling mechanisms^{104–106}. While moisture management and radiation cooling mechanisms are available for personal thermal management, they are less relevant for heat dissipation from wearable electronic devices. Active cooling strategies such as liquid-cooled garments can be bulky, expensive, and power consuming¹⁰⁶. To overcome some of these limitations, recent work has focused on developing *thermally conductive* polymer-based textiles as substrates for thermal management^{107–111}. For example, Gao *et al.*¹⁰⁷ demonstrated 3D-printed fabrics constructed from aligned boron-nitride (BN) /poly-vinyl alcohol composite fibers for personal cooling applications with enhanced heat spreading properties and ~ 2 times higher thermal conductivity compared to conventional textiles. Wang *et al.*¹⁰⁸ produced nanocomposite textiles consisting of boron nitride

⁴ Portions of this section are reproduced from a recently submitted journal paper that is currently under review

nanosheets and polyimide fibers with a thermal conductivity of $\sim 13 \text{ Wm}^{-1}\text{K}^{-1}$. Gong *et al.*¹⁰⁹ reported an in-plane thermal conductivity of $\sim 4 \text{ Wm}^{-1}\text{K}^{-1}$ for graphene woven fabric-reinforced polymer composites. Our recent work¹¹⁰ showed that fabrics woven from ultra-high molecular weight polyethylene (UHMW-PE) fibers exhibit an in-plane thermal conductivity up to $\sim 10 \text{ Wm}^{-1}\text{K}^{-1}$. More recently, Tang *et al.*¹¹¹ constructed electronic textiles using ultrasonication of non-woven fabric in a dispersion of carbon nanotubes, and measured a thermal conductivity of $\sim 3 \text{ Wm}^{-1}\text{K}^{-1}$. These prior studies demonstrate great promise of engineered textiles for heat spreading, which has also led to emerging of commercial fabrics in this material space. Considering this trend, there is a need for exploration of the interrelated thermal and mechanical properties of these commercially produced polymer-based materials for flexible heat spreading applications, and to obtain an understanding of their properties compared to conventional alternatives.

CHAPTER 3. INFRARED MICROSCOPY-ENHANCED CHARACTERIZATION: IN-PLANE HEATER WIRE METHODS

This chapter presents two experimental methodologies based on infrared (IR) microscopy that can be used to characterize the thermal transport properties of materials. Section 3.1 briefly describes the experimental principles of a transient method based on the Angstrom's method to measure the thermal diffusivity of rod-like structures such as fibers. This technique was developed by Hahn *et al.*⁸⁷. The thermal diffusivity of UHMW-PE fibers is measured using this technique (results in Chapter 4). Section 3.2 details a steady state technique using the same experimental facility that enables direct characterization of the thermal conductivity of a specimen and can be broadly applied for in-plane thermal characterization of different material forms and geometries. The effective thermal conductivities of individual UHMW-PE fibers, twisted yarns and woven fabrics constructed from twisted yarns are measured using this method (results in Chapter 4). *The content in Section 3.2 was published in the IEEE ITherm (May 2019) conference proceedings*¹¹² *as part of this work.*

3.1 Micro-IR Angstrom Measurement Technique

Recently, Hahn *et al.*⁸⁷ employed the measurement principles of the Angstrom method to develop a miniaturized version of this technique that is enhanced using IR microscopy. The principle of this micro-IR Angstrom method is illustrated in Figure 3.1a. IR imaging allows for capturing the complete temperature profile along the length of the sample, as compared to just two discrete locations in the traditional Angstrom method. This facilitates measurement of possible variation of thermal diffusivity along the length of the sample, and also allows measurement of microscale samples due to no requirement of thermocouples or contact-based temperature sensing.

Figure 3.1b shows photographs of the experimental equipment used in these measurements. An IR microscope (Quantum Focus Instruments Corporation) is used to visualize the quasi-steady spatial temperature distribution in the sample as a function of time when an electrical heating wire is oriented perpendicularly in contact with the sample at its center. The sample is subjected to periodic Joule heating using an electric circuit consisting of a power supply, relay switch and function generator to regulate the heating frequency. The heater-sample arrangement is placed in a vacuum chamber to minimize the experimental impacts associated with convective heat transfer at the same frequency as the heating source ⁸⁷.

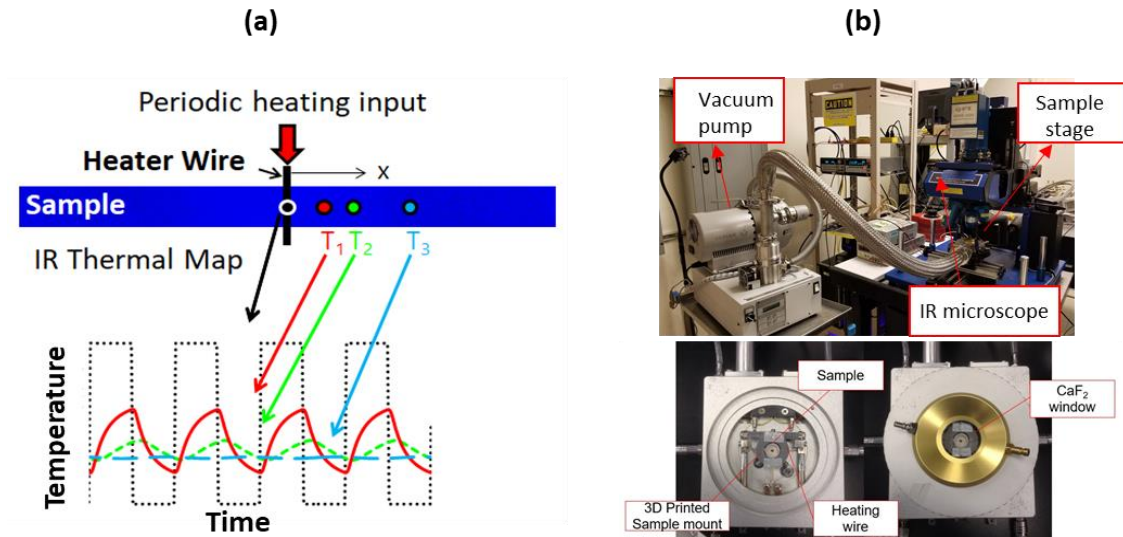


Figure 3.1: (a) Illustration of the principle of the micro-IR Angstrom method. (b) Experimental equipment showing the IR microscope, vacuum pump and sample stage employed in the thermal diffusivity measurements.

This method has been applied by Hahn *et al.* ⁸⁷ to measure the thermal properties of various polymer filaments and reasonably good agreement with other data in the literature is obtained. Further details of the experiments and the data analysis are provided in ⁸⁷ and ¹¹³. In the present work, this technique is employed to characterize the thermal diffusivity of individual UHMW-PE fibers.

3.2 Steady State Thermal Conductivity Measurement Technique

The IR-based Angstrom's method described in the previous section cannot be directly applied to measure the thermal conductivity of a material; this must be extracted from the measured thermal diffusivity using known values of material density and specific heat capacity. For porous material forms such as fibers, yarns and fabrics, these properties are not always well defined and accurate extraction of thermal conductivity is a challenge. To address this aspect as well as some of the other challenges associated with general measurement techniques (described in Section 2.2), a simple measurement method is required to enable direct measurement of material thermal conductivity across different length scales.

In this chapter, a steady state method based on infrared microscopy for measuring the effective in-plane thermal conductivity of a material is described. As shown in Figure 3.2, a suspended heater wire contacts an orthogonal sample in a suspended cross-structure arrangement and this assembly is attached to a circular heat sink. A complementary one-dimensional heat transfer model is developed to extract the thermal conductivity of the sample based on the experimentally measured temperature profiles. A unique feature of this method is that the contact resistance between the wire and the target sample is not needed to obtain the thermal conductivity of the sample. The proposed technique is validated using reference samples of known thermal conductivity and an uncertainty analysis is conducted to assess the confidence level associated with the measured thermal properties.

3.2.1 Methods

3.2.1.1 Experimental Facility Details

An IR thermal microscope (Quantum Focus Instruments Corporation; see Figure 3.1) having a temperature resolution of $\sim 0.1^{\circ}\text{C}$ and a spatial resolution of $\sim 12.2\text{ }\mu\text{m}$ measures the temperature

profile during the experiment. Schematic drawings of the experimental setup are shown in Figure 3.2. The sample to be characterized is suspended across the middle of an annular-ring-shaped heat sink (~1 cm inner diameter) and is heated at its lengthwise center by an orthogonally-aligned nichrome heater wire (30 AWG). The sample and wire are suspended in a vacuum chamber (Linkam Scientific Instruments TS1500V) with both ends attached to a 3D printed circular heat sink. A turbomolecular pump (Varian TPS Bench-9698215) is connected to the vacuum stage to maintain a pressure of 1×10^{-5} mbar in order to minimize any convection losses from the system. A DC power source (Keithley 2420) supplies current to the nichrome wire via the electrical feedthroughs of the vacuum chamber. The electrical resistance per unit length of the wire is measured *ex situ* for 6 different wire lengths and the mean resistance (R_l) is $22.44 \pm 0.07 \, \Omega\text{-m}^{-1}$ at room temperature. During the experiment, the electrified wire heats up due to Joule heating; heat is conducted in the wire both to the sink at either end and to the center, where the sample is attached, establishing a non-linear temperature profile in the wire at steady state. In the sample, heat is conducted from the central contact with the wire to the sink at both ends; at steady state, this establishes a linear temperature gradient in both halves of the sample.

Prior to experiments, the emissivity of the nichrome wire and the target sample are calibrated *ex situ*. For all experiments, the nichrome wire is first coated black with a colloidal graphite solution to reduce its reflectivity. The wire and sample are then fixed to a temperature-controlled heating stage maintained at a uniform temperature (in the range of 60°C-80°C). The IR microscope detector measures the radiative heat flux, within the spectral range of the detector, from the wire and the sample to determine their emissivity values based on the known stage temperature. The uncertainty in emissivity is also determined based on a standard deviation in the spatial mean of the extracted emissivity maps. Based on these calibrated emissivities, a constant

emissivity value is assigned in the appropriate regions of the wire/sample during the actual thermal measurements to extract the corresponding temperature profiles.

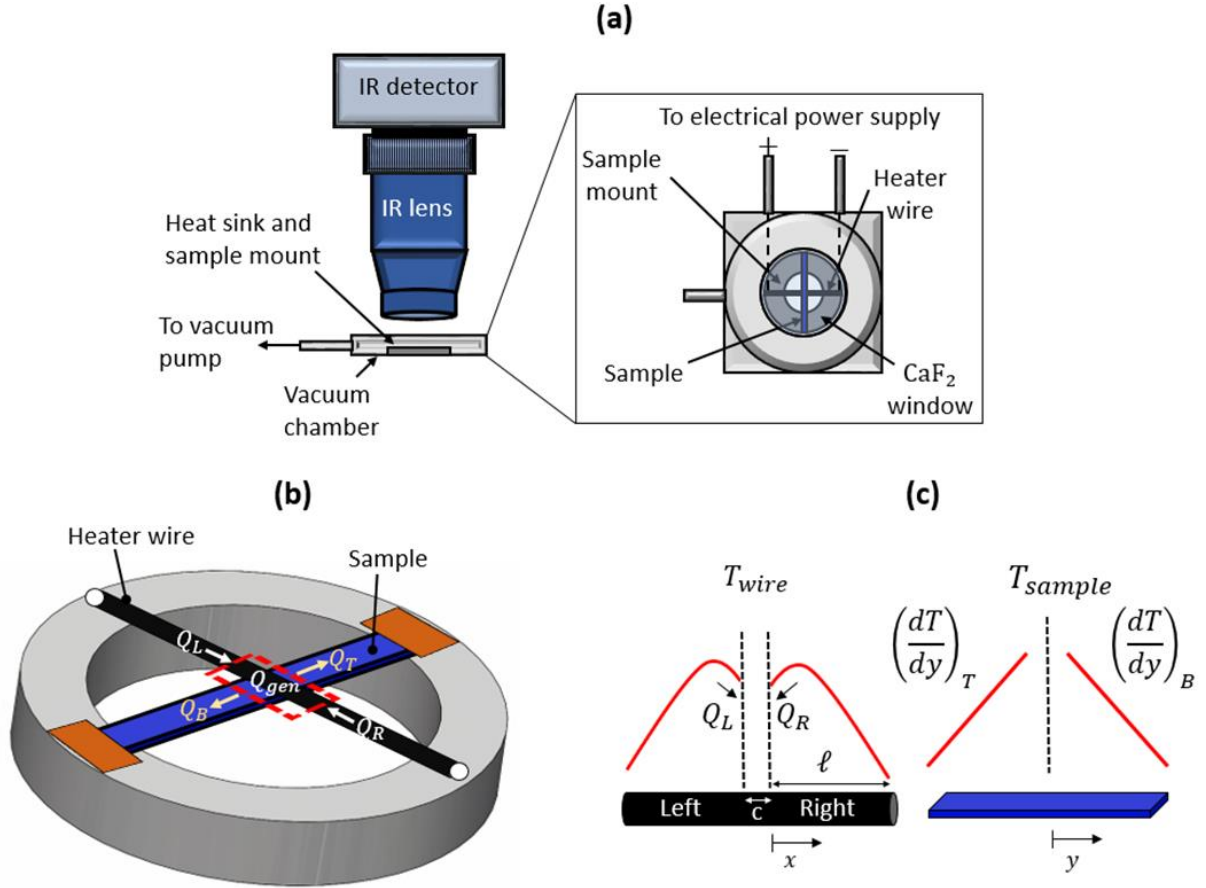


Figure 3.2: Schematics of the experimental setup. (a) The assembly consisting of the crossing sample and heater wire on a heat sink with a circular opening are placed in a vacuum chamber to minimize convection losses (see top-down view in inset). (b) Illustration of the energy balance in the wire–sample cross-structure arrangement; all of the heat conducted into the junction from the left and right sides of the heater wire (Q_L and Q_R , respectively) and the heat generated in the junction region (Q_{gen}) conducts into the sample (Q_T and Q_B). (c) Expected temperature profiles of the wire and the sample which are measured during the IR experiments.

The heat rates (Q_L and Q_R) and temperature gradients $((dT/dy)_T$ and $(dT/dy)_B$) are calculated from these profiles.

3.2.1.2 Thermal Characterization Methodology

Measurement principle. The effective thermal conductivity of the target specimen is determined based on Fourier's law, which relates heat flow (Q) to the thermal conductivity (k), temperature gradient (dT/dy) and cross-sectional area (A):

$$|Q| = kA \left| \frac{dT}{dy} \right| \quad (3.1)$$

Considering a control volume around the central contact region between the wire and the junction, as shown in Figure 3.2b, we define Q_L and Q_R as the heat rates entering this control volume through the wire, and Q_T and Q_B as the heat rates leaving this control volume through the sample. There is also heat generation in the central region of the wire within the control volume, $Q_{gen} = I^2 R_l c$, where I is the current supplied to the wire, R_l is the measured electrical resistance per unit length of the wire, and c is the length of the wire within the control volume. From an energy balance in this control volume, the total amount of heat leaving the wire at the wire-sample junction must flow into the sample at steady state:

$$Q_L + Q_R + Q_{gen} = Q_T + Q_B, \quad (3.2)$$

where the subscripts L , R , T , and B indicate the left, right, top, and bottom, respectively. Because the sample has no heat generation and minimal losses, we can express the total heat flow through both sides of the sample in terms of the corresponding temperature gradients using eq. (3.1):

$$Q_T + Q_B = k_s A_s \left| \frac{dT}{dy} \right|_T + k_s A_s \left| \frac{dT}{dy} \right|_B, \quad (3.3)$$

where k_s and A_s are the thermal conductivity and cross-sectional area of the sample, respectively. Note that the temperature difference across the wire-sample junction is related to the thermal contact resistance (R_c) at the junction and this rate of heat flow:

$$Q_L + Q_R + Q_{gen} = \frac{T_w - T_s}{R_c}, \quad (3.4)$$

where T_w and T_s are the temperatures of the wire and the sample, respectively, at the contact point. It is critical to note that neither eq. (3.4) nor the wire–sample thermal contact resistance is needed or used in the analysis, as the temperature gradient in the sample is measured outside of the contacting region. Thus, the axial thermal conductivity of the target sample can be directly calculated, provided that the heat rates leaving the wire and the temperature gradients in the sample can be measured:

$$k_s = \frac{Q_L + Q_R + Q_{gen}}{A_s \left\{ \left| \frac{dT}{dy} \right|_T + \left| \frac{dT}{dy} \right|_B \right\}}. \quad (3.5)$$

The temperature gradients in the target sample are measured from the infrared images, and the heat rates from the wire, Q_L and Q_R , are determined from temperature measurements of the wire combined with a one-dimensional heat transfer model, described below. Measurements are taken at several power levels to improve accuracy and two infrared images are taken at each power level. Note that, depending on the thermal conductivity and dimensions of the sample being measured, in some cases the radiation losses from the sample need to be considered to obtain an accurate measurement of sample thermal conductivity. Also, radiation losses from the wire region inside the control volume are generally very small compared to the total heat rate, $Q_L + Q_R + Q_{gen}$, but may be important in some cases when low thermal conductivity samples are being measured. A discussion on the consideration of radiation losses is provided in a later section below.

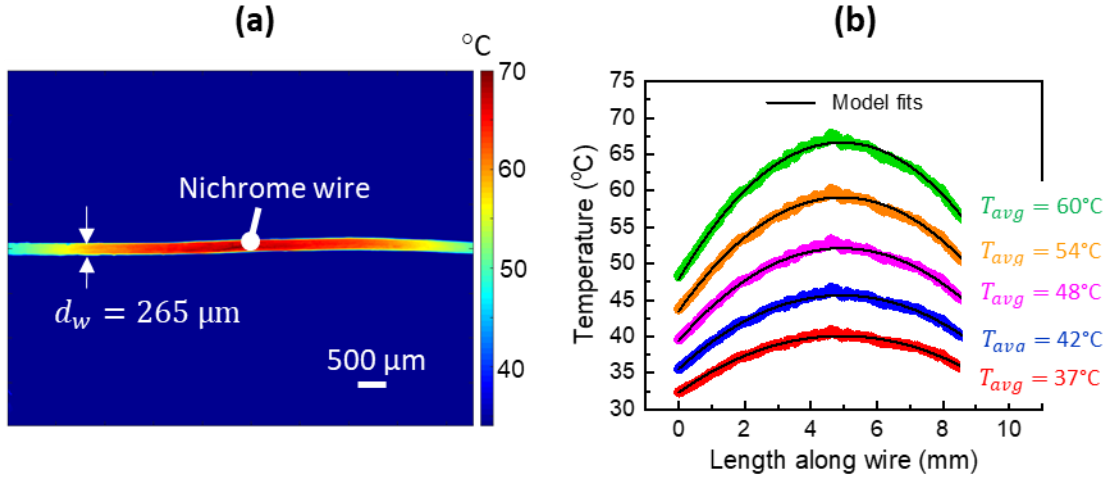


Figure 3.3: (a) IR temperature map of the wire calibration experiment at a current input of 220 mA, corresponding to $T_{avg} = 60^\circ\text{C}$. (b) Experimental and fitted temperature profiles of the nichrome wire at all power levels (best fit: $k_w = 10.9 \text{ Wm}^{-1}\text{K}^{-1}$). The error in experimental temperature data is smaller than the size of the data points shown (in the range of $\pm 0.5\text{-}0.9^\circ\text{C}$ depending on temperature).

Calibration of the wire thermal conductivity. The thermal conductivity of the nichrome wire is first calibrated in a standalone experiment. For this purpose, a graphite-coated nichrome wire is placed in the experimental setup without the sample as shown in Figure 3.3 and electrically heated. The experimental temperature profile of the wire is obtained at steady state by capturing temperature maps using the IR camera at multiple power levels. This temperature profile is dictated by heat generation in the wire and by radiation losses to the surroundings. The governing energy equation and boundary conditions representing this situation are given as

$$\frac{\partial^2 T}{\partial x^2} - \frac{h_r P(T - T_{sur})}{k_w A} + \frac{q'''}{k_w} = 0 \quad (3.6)$$

$$x = l: T = T_0 \quad (3.7)$$

$$x = \frac{l}{2}: kA \left| \frac{dT}{dx} \right| = 0, \quad (3.8)$$

where T_{sur} is the temperature of the surroundings, q''' is the heat generation rate in the wire, P is the wire perimeter, A is the wire cross-sectional area, h_r is the linearized radiation heat transfer coefficient, l is the length of the wire, T_0 is the known temperature boundary condition, and k_w is the wire thermal conductivity. Note that $q''' = (I^2 R_l)/A$, where I is the supplied current. The value of T_0 is fixed at steady state for each side of the wire at a given input current, and is determined from the measured IR temperature map. The effective surrounding temperature for radiation heat transfer from the wire, T_{sur} is estimated to be 23°C with an uncertainty of $\pm 2^\circ\text{C}$ to account for the maximum possible span between the measured ambient temperature and the temperature inside the chamber enclosure. Also, we assume $h_r \sim \sigma \epsilon (T_{avg}^2 + T_{sur}^2)(T_{avg} + T_{sur})$ ⁶³, where T_{avg} is the average (measured) wire temperature, ϵ is the wire emissivity, and σ is the Stefan-Boltzmann constant. The emissivity is taken as the calibrated value of the carbon-coated wire (0.64), which is a good assumption because the IR detector operates in the 2-5 μm wavelength range, close to the peak emission wavelength in the Planck distribution at the wire temperature. The solution for the differential eq. (3.6) with the boundary conditions (3.7) and (3.8) yields the following expression for the wire temperature profile:

$$T(x) = \frac{1}{m^2 k_w (e^{ml} + 1)} \left(e^{m(l-x)} \{ m^2 k_w (T_0 - T_{sur}) - q''' \} + e^{ml} \{ m^2 k_w T_{sur} + q''' \} \right. \\ \left. + e^{mx} \{ m^2 k_w (T_0 - T_{sur}) - q''' \} + m^2 k_w T_{sur} + q''' \right), \quad (3.9)$$

where $m^2 = (h_r P)/(k_w A)$. All other parameters in the above equation are known except for k_w , which can therefore be determined using a single-parameter least squares fit of the measured and theoretical temperature profiles.

An example IR temperature map obtained from the wire calibration experiment is shown in Figure 3.3a. The temperature reaches a maximum at the center of the wire and the temperature distribution is approximately symmetric about this location. The experiments are conducted at 5 different levels of input current and 5 temperature maps are obtained at steady state. These data are analyzed to obtain the temperature profiles along the length of the wire for all power levels, which are fit simultaneously with the model described by eq. (3.9), with all input parameters set to their nominal values. As seen in Figure 3.3b, this single fit provides a very good match with the model across all power levels for a wire thermal conductivity of $10.9 \text{ Wm}^{-1}\text{K}^{-1}$. This also indicates that the temperature dependence of thermal conductivity of the wire is not significant in the range of operating temperatures. Further, fitting the same experimental data with the model, but neglecting radiation losses (only considering heat conduction), overestimates the thermal conductivity by $\sim 15\%$. Therefore, it is important to consider the effect of radiation losses from the wire in the measurement.

Sample thermal conductivity measurement. Next, the target sample is attached perpendicular at the center of the heater wire, as shown in Figure 3.2b, and the experiments are conducted in this cross-structure arrangement across a range of applied powers. Steady state infrared images are recorded that include both the wire and the sample.

For the heater wire, a dip in the temperature profile is observed at the center due to the heat removed by the sample at the wire–sample junction. In this situation, the governing eq. (3.6) remains valid for each side of the suspended region of the wire, but the boundary conditions are modified due to heat loss at the center of the wire. Focusing on the region of the suspended wire to the right of the junction, the boundary conditions become:

$$x = \ell: T = T_0 \quad (3.10)$$

$$x = 0: kA \left| \frac{dT}{dx} \right| = Q_R, \quad (3.11)$$

where ℓ now represents the length of the wire on the right side of the sample. Thus, $x = 0$ represents the edge of the wire domain near the wire–sample junction where a heat rate of Q_R flows out of the wire. The expression for the wire temperature profile on the right side is then given by:

$$\begin{aligned} T(x) = & \frac{e^{-mx}}{m^2 k_w A (e^{2m\ell} + 1)} \left(A e^{m(2x+\ell)} \{m^2 k_w (T_0 - T_{sur}) - q'''\} \right. \\ & + A e^{m(2\ell+x)} \{m^2 k_w T_{sur} + q'''\} - m Q_R e^{2m\ell} + m Q_R e^{2mx} \\ & \left. + A e^{m\ell} \{m^2 k_w (T_0 - T_{sur}) - q'''\} + A e^{mx} \{m^2 k_w T_{sur} + q'''\} \right). \end{aligned} \quad (3.12)$$

The only unknown parameter in the above equation is Q_R , which is determined by fitting eq. (3.12) to the experimental data. The analogous Q_L is determined in the same manner. In practice, the edge of the fitted region might not extend to the central junction contact point exactly, in part because the sample blocks the view. Thus, the actual heat rate leaving the wire is determined by adding the heat generated in the central region of the wire, as discussed earlier. The edge of the wire domain where the heat flux boundary condition is applied can be moved away from the junction to ensure that one-dimensional heat transfer assumptions are accurate in the modeled region, and the heat rates at the junction can still be calculated using the heat generation term inside the control volume. Therefore, this method does not make any assumptions regarding the nature of contact between the wire and the target sample, and the heat flow rates into the sample can be accurately determined independent of any contact resistance. The analysis also does not require symmetry of the experimental wire temperature profiles on each side, as the heat rates Q_L and Q_R are determined independently.

The final step in the calculation of sample thermal conductivity is determination of the temperature gradients on each side of the sample, $|dT/dy|_T$ and $|dT/dy|_B$. This involves analysis of the steady state temperature maps of the sample corresponding to the wire temperature profiles. In the sample region, conduction is the only mode of heat transfer and radiation loss is neglected due to the low temperature difference between the sample and the surroundings. Therefore, a linear temperature profile is expected on each side of the sample as shown in Figure 3.2c, and the temperature gradients can be trivially determined from the slope of the profiles. Ultimately, the thermal conductivity of the sample is determined using eq. (3.5).

Radiation Loss Consideration. The thermal conductivity measurement technique described above considers the effect of radiation losses from the suspended region of the heated wire through the associated heat transfer model (eq. (3.12)), but does not include radiation losses from the samples. Radiation losses in the sample region are significant only when relatively low thermal conductivity samples are used. Additionally, we note that a linear temperature profile is generally observed in the sample region for most experiments in this study, which demonstrates that the radiation losses from this region are not significant, and the temperature profile is solely dictated by conduction.

However, in cases where the thermal conductivity of the sample may be low, these radiation losses in the sample region can be included to obtain a more accurate thermal conductivity measurement. The governing equation for heat transfer in the sample region (on each side of the heater wire) based on a linearized radiation heat transfer model is given as:

$$\frac{\partial^2 T}{\partial y^2} - \frac{h_r P_s (T - T_{sur})}{k_s A_s} = 0, \quad (3.13)$$

where k_s is the sample thermal conductivity, h_r is the linearized radiation heat transfer coefficient, T_{sur} is the temperature of the surroundings, P_s is the sample perimeter, A_s is the sample cross-

sectional area, and y is the direction along which the length of the sample is oriented. As seen from eq. (3.13), the sample temperature profile becomes non-linear only when $\frac{h_r P_s (T - T_{sur})}{k_s A_s}$ is significant, which occurs for low thermal conductivity samples. Solving eq. (3.13) based on a one-dimensional fin analysis with known temperature boundary conditions T_{L_T} at the end of the sample, and T_{b_T} at the base near the contact with the heater wire, yields the following solutions for the total heat transfer rate to the top side of the sample (Q_T) and the sample temperature profile ($T_T(y)$)⁶³:

$$Q_T = \sqrt{h_r P_s k_s A_s} \theta_{b_T} \left(\frac{\cosh(mL_T) - \theta_{L_T}/\theta_{b_T}}{\sinh(mL_T)} \right) \quad (3.14)$$

$$\frac{\theta_T}{\theta_{b_T}} = \left(\frac{(\theta_{L_T}/\theta_{b_T}) \sinh(my) + \sinh m(L_T - y)}{\sinh(mL_T)} \right). \quad (3.15)$$

Here, L_T is the sample length on the top side between the two boundary temperature locations, $\theta_T = T_T(y) - T_{sur}$, $\theta_{b_T} = T_{b_T} - T_{sur}$, $\theta_{L_T} = T_{L_T} - T_{sur}$, and $m^2 = (h_r P_s)/(k_s A_s)$. Note that analogous equations are valid on the bottom side of the sample which has a heat rate of Q_B flowing through it a steady state. Based on the heat transfer model described above, $Q_T + Q_B$ is known from the temperature profile in the heater wire and the heat generation in the central control volume and therefore, the sample thermal conductivity can be determined by solving for m from eq. (3.14) and its analogous form that applies to the bottom side of the sample. The temperature profile in the sample region can then be determined using eq. (3.15) and compared to the experimentally measured temperature profiles. This offers an approach to take into account radiation losses when important for certain samples and demonstrates the generality of the developed measurement technique.

In Figure 3.4, we plot the temperature profiles in the sample region as a function of sample thermal conductivity as extracted from the above model to illustrate that radiation losses are

important only for low thermal conductivity samples. The input parameters for the above equations are chosen such that they are representative of the fabric experiment (details in the following chapter, Section 4.2.2) in terms of geometry, surface properties, etc. The radiation losses in the sample region only result in a significant deviation from a linear temperature profile for values of $k_s < \sim 1 \text{ Wm}^{-1}\text{K}^{-1}$. For conductivities on the order of the fabric samples ($\sim 10 \text{ Wm}^{-1}\text{K}^{-1}$) characterized in this work, it is appropriated to neglect radiation losses.

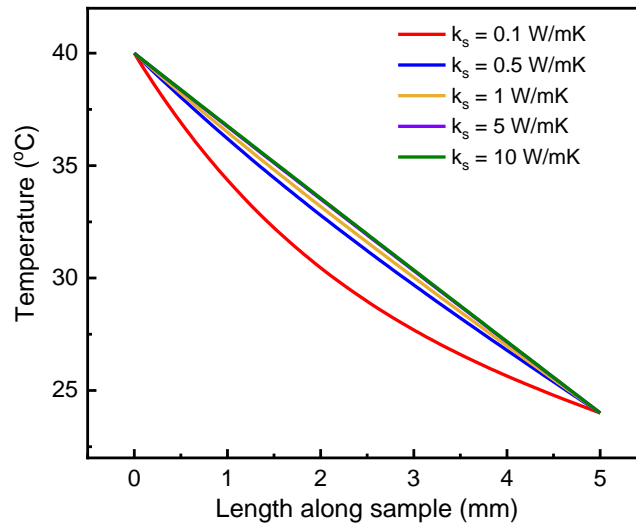


Figure 3.4: Temperature profile in the sample for several different assumed sample thermal conductivities when radiation losses in the sample region are included (sample width = 2 mm, sample thickness = 650 μm , emissivity = 0.6, $T_b = 40 \text{ }^\circ\text{C}$, and $T_L = 24 \text{ }^\circ\text{C}$).

Radiation losses from the heater wire comprise two components: radiation losses from the suspended regions on each side of the sample; radiation losses from the region inside the central control volume considered for the energy balance at steady state. The radiation losses from the suspended region are incorporated in the heat transfer model that dictates the wire temperature profile. On the other hand, the radiation losses from the central wire region are generally very low (less than $\sim 1\%$) compared to the total heat conducted from the wire into the sample for the yarn and fabric experiments presented in the next chapter. This component (Q_{rad}) is dependent on the

thermal properties of the sample and is significant for relatively low thermal conductivity samples. The experimental temperature profile of the wire in the central region can be used to determine Q_{rad} based on the radiation heat transfer between the wire and the surroundings in this region. When important, this can simply be incorporated in the thermal conductivity calculation via energy balance as follows:

$$k_s = \frac{Q_L + Q_R + Q_{gen} - Q_{rad}}{A_s \left\{ \left| \frac{dT}{dy} \right|_T + \left| \frac{dT}{dy} \right|_B \right\}} \quad (3.16)$$

3.2.2 Validation of the Measurement Technique

In order to validate the proposed measurement technique, experiments are performed using reference samples having known thermal conductivity. Two different materials are chosen because they have a similar geometry as the yarn and fabric samples characterized in this work (in the following chapter): a nichrome wire (circular cross-section similar to the yarn) and a bulk HDPE film (rectangular cross-section) of width comparable to the fabric sample.

3.2.2.1 Nichrome Wire

Experiments are performed using a reference nichrome wire as the “sample”. Specifically, a carbon-coated nichrome wire heater is oriented perpendicularly to contact another similar nichrome wire; the experiments and model fitting are otherwise performed in an identical manner as detailed in the measurement methodology. As illustrated in Figure 3.5, the linear fit of the experimental data yields a thermal conductivity of $11.8 \text{ Wm}^{-1}\text{K}^{-1}$. This result is within 10% of the value determined from the standalone thermal conductivity calibration of the nichrome wire. Also, this is in good agreement with thermal conductivity values of standard nichrome alloys published in the literature, which are on the order of $11\text{-}13 \text{ Wm}^{-1}\text{K}^{-1}$ ^{63,114–116}.

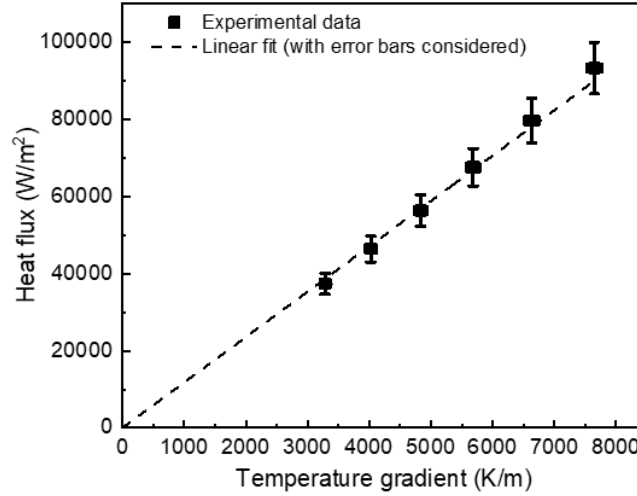


Figure 3.5: Heat flux as a function of the sample temperature gradients for a validation experiment using a nichrome wire as the sample. The best-fit “sample” wire thermal conductivity is $k_w = 11.8 \text{ Wm}^{-1}\text{K}^{-1}$.

3.2.2.2 High Density Polyethylene Sheet

Experiments are performed using a high density polyethylene (HDPE) sheet (width of ~ 2 mm and thickness of $\sim 381 \mu\text{m}$) as a reference sample. The emissivity of the black HDPE film (as received) is calibrated to be 0.81 ± 0.01 . Due to the relatively low thermal conductivity of this sample, radiation losses from the sample region must be considered in this case. These losses are incorporated to obtain an accurate measurement of thermal conductivity, and are included using the approach described in Section 3.2.1.2.

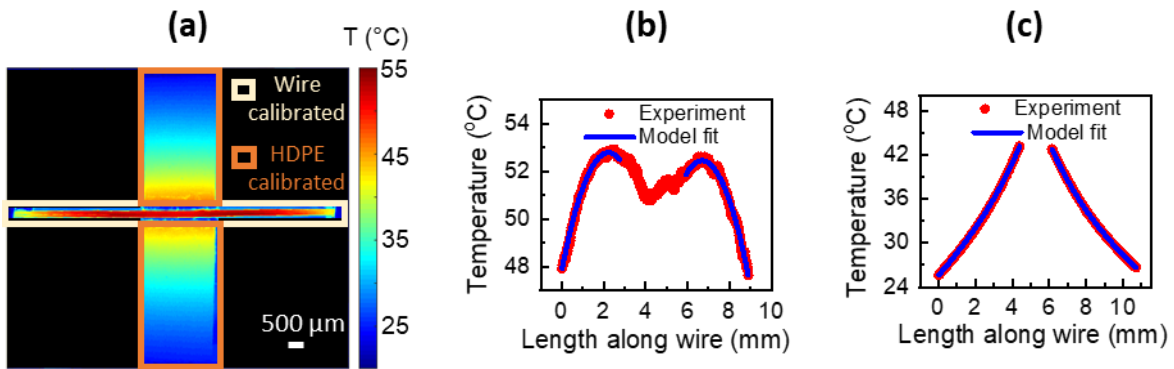


Figure 3.6: (a) IR temperature map of the experiment with the HDPE sample at an input electrical current of 240 mA. Experimental and modeled temperature profiles of the (b) wire in the suspended region and (c) the HDPE sample including radiation losses from the sample.

Figure 3.6a shows a representative IR temperature map for this experiment. Note that the temperatures of the HDPE sheet are higher than those in the fabric sample at similar applied powers (see Figure 4.5a in the following chapter), which is an indication of its lower thermal conductivity. The relatively lower thermal conductivity also leads to a shallower dip in the wire temperature profile, as seen in Figure 3.6b, when compared to the case of the woven fabric sample (see Figure 4.5b in the following chapter). The total heat rate conducting into the sample is determined using the energy balance approach described in Section 3.2.1.2. The temperature profiles in the sample region seen in Figure 3.6c have an exponential profile because the radiation losses from the sample are significant. Figure 3.6c also indicates that a good match is obtained between the experimental temperatures and the fin model (eq. (3.15)). Based on these measurements, the sample thermal conductivity is extracted using eq. (3.14).

The average value of sample thermal conductivity based on measurements at five different power levels is determined to be $0.49 \pm 0.02 \text{ Wm}^{-1}\text{K}^{-1}$, which is in excellent agreement with the known thermal conductivity of high density polyethylene^{117–119}.

3.2.3 Uncertainty and Sensitivity Analysis

Various input parameters are involved in analysis of the experimental data; assessing the sensitivity of the measurements to these parameters and the total uncertainty associated with the results is important in understanding the accuracy of the measurement. Therefore, a thorough model uncertainty and sensitivity analysis is conducted to estimate our confidence in the measured thermal conductivity. Here, the uncertainty analysis is described the validation experiment with the nichrome wire reference sample. The nominal values of all the known parameters and their estimated uncertainties are summarized in Table 3.1. The uncertainty for the input heater wire thermal conductance is estimated based on standard uncertainty propagation¹²⁰, applied to the

wire-only calibration experiment. Specifically, the total uncertainty in the calibrated wire thermal conductance is calculated using

$$\Delta(k_w A) = \sqrt{\sum_j^n \left(\frac{\partial(k_w A)}{\partial j} \Delta j \right)^2}, \quad (3.17)$$

where j refers to each of the four parameters involved in the calibration experiment ($T_{sur}, R_l, \epsilon_w, d_w$). Note that the extraction of the heat transfer rates and error propagation is based on the conductance ($k_w A$) and not conductivity (k_w); this is done to reduce the total error because the area of the wire is not required to extract the calibrated conductance.

The total uncertainty associated with the measurement technique is evaluated by first calculating the total error associated with each data point (with respect to both coordinates) in the linear fit of Figure 3.5. These error values are calculated based on applying eq. (3.17) to the calculation of the total heat flux and the sum of the temperature gradients. Error in the temperature gradient (horizontal-axis error bars) is only due to uncertainty in the sample emissivity, while error in the heat flux (vertical-axis error bars) is due to uncertainties in all the other known parameters. The total uncertainty is equal to the estimated error in the slope of the linear fit performed using a weighted regression analysis with uncorrelated errors along the horizontal and vertical axes ^{121,122}.

Table 3.1: Nominal value and uncertainty in experimental and modeling parameters for the validation measurements (validation sample is another nichrome wire with same emissivity and diameter as the heater wire)

Parameter	Nominal value	Uncertainty (\pm)
T_{sur}	23°C	2°C
R_l	22.44 Ωm^{-1}	0.07 Ωm^{-1}
ϵ_w	0.64	0.02
d_w	265 μm	10 μm
kA_w	$5.99 \times 10^{-7} \text{ WmK}^{-1}$	$0.7 \times 10^{-8} \text{ WmK}^{-1}$
$\epsilon_s = \epsilon_w$	0.64	0.02
$d_s = d_w$	265 μm	10 μm

The model sensitivity analysis is performed for the validation experiment with the wire reference sample to understand the individual effect of each model parameter on the measurement results. The thermal conductivity of the sample is extracted with a given parameter changed by its uncertainty value while all other parameters are fixed at their nominal values. Consequently, the fitted heat rates, Q_L and Q_R , and the temperature gradients, $|dT/dy|_T$ and $|dT/dy|_B$ are altered, and the resulting thermal conductivity is determined. This is repeated for all the parameters listed in Table 3.1, and the absolute change in thermal conductivity, $|\Delta k|$ is evaluated in each case.

Using the approach described above, the total absolute uncertainty in the thermal conductivity measurement of the reference sample is calculated to be $0.4 \text{ Wm}^{-1}\text{K}^{-1}$ which corresponds to an uncertainty of only $\sim 3.5\%$. The same analysis approach is used to calculate the total uncertainty for the other experiments (fiber, yarn and fabric samples) characterized in this

study. The uncertainties in these measurements are generally slightly higher and depend on the various experiment and model parameters in each case.

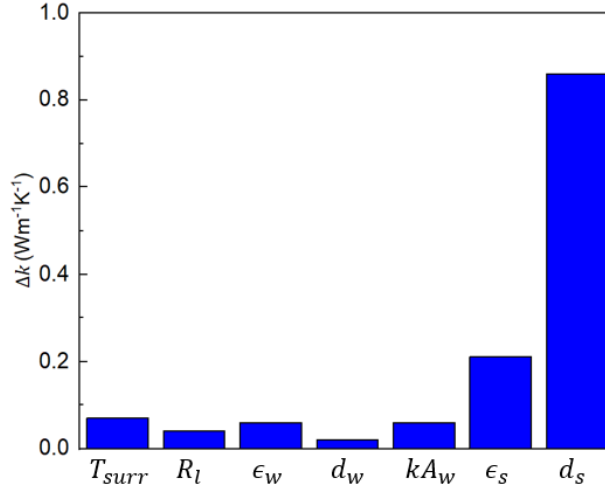


Figure 3.7: Sensitivity analysis of experimental and modeling input parameters for the validation experiment with the nichrome wire reference sample. Each parameter is varied by its uncertainty amount and the resulting absolute change in thermal conductivity, $|\Delta k|$ is shown in the vertical axis.

The results of the sensitivity analysis for the wire reference sample are shown in Figure 3.7. The measurement is most sensitive to the sample diameter, because this directly influences the extraction of thermal conductivity calculation as seen from eq. (3.5). For the actual fiber and yarn samples characterized in this work, the effect of this parameter is expected to be even greater due a higher uncertainty in the effective diameter of these samples compared to the reference nichrome wire. We note that the process of performing the experiments and analysis at multiple power levels to extract a single measurement for thermal conductivity helps to greatly reduce the total uncertainty associated with the measurement technique.

3.2.4 Summary of the Developed Technique

An infrared microscopy technique for measuring the in-plane thermal conductivity of different materials has been demonstrated. The presented approach is based on simple energy

balances, and the associated experiments are implemented by contact heating of the target specimen using a nichrome wire suspended in a vacuum chamber. A one-dimensional steady state heat conduction model, incorporating radiation losses, is used to analyze the experimental temperature maps and extract the thermal conductivity. The technique is validated by performing measurements with standard reference samples and a detailed uncertainty analysis is performed. Additionally, this method is not dependent on the nature of thermal contact at the junction between the heating wire and the contacting target sample; eliminating the need for estimating this contact resistance to extract the sample conductivity is a major advantage of this approach compared to other characterization techniques. Further, the developed technique is generally scalable for in-plane thermal characterization of samples across different length scales and ranges of thermal conductivity.

CHAPTER 4. THERMAL CHARACTERIZATION OF ULTRA-HIGH MOLECULAR WEIGHT POLYETHYLENE: FROM FIBERS TO FABRICS

In this chapter, the thermal conductivity of UHMW-PE fibers, yarns formed from twisting these fibers, and woven fabrics are experimentally characterized. Plain-weave type fabrics are constructed from UHMW-PE yarns with a relatively higher density of yarns along one direction of the fabric. Such multi-scale thermal characterization of the different forms of UHMW-PE is achieved using we the in-house IR steady-state thermal conductivity measurement method described in Chapter 3. The axial thermal conductivity of the fibers and yarns, and the in-plane effective thermal conductivity of the fabric in the dominant heat conduction direction are measured. The resulting findings help understand the effective thermal behavior as a function of scaling-up the high conductivity fibers, and indicate very promising thermal properties for the woven fabrics for applications as a flexible/wearable heat spreader. In addition, a reduced-order heat conduction model is also developed to estimate the effective in-plane thermal conductivity of plain-weave fabrics, which serves as a simple confirmation of the key conclusions from the experimental data. *The content in this chapter was published in ACS Appl. Polym. Mater.*¹¹⁰ *as part of this work.*

4.1 Methods

The UHMW-PE material used in this study was acquired in the form of a flat yarn (DSM Dyneema SK75; Atkins and Pearce Inc.) with a linear density of 0.044 g/m. The fibers in the flat yarn are twisted together using a drop spindle tool which produces a well-bound twisted yarn (see Figure 4.1) that is suitable for weaving.

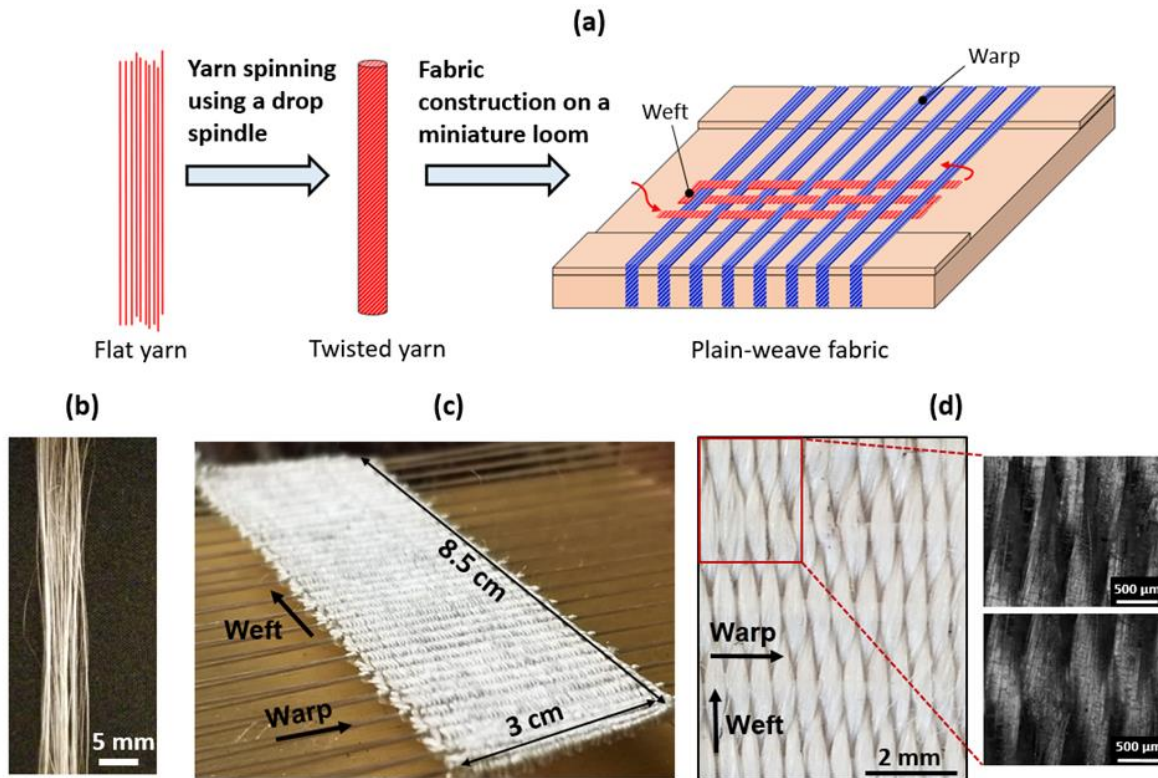


Figure 4.1: (a) Overview of the procedure for construction of plain-weave fabrics from flat yarn (Dyneema). Photographs of the (b) flat yarn (as received) with loosely bound individual fibers and (c) a woven fabric prototype sample when held in the miniature loom with warp and weft directions identified. (d) Top-view photograph of the woven fabric with inset showing optical microscope images of portions of the weave at high magnification. The weft yarn number density is 4-5 times higher compared to that of the warp yarns resulting in a weft-faced plain-weave pattern in which the warp is almost completely covered by the weft. Thermal characterization is conducted along the high density weft yarn direction.

The twisted yarns are used to construct a swatch of woven fabric on a miniature weaving loom (Wee Weaver; Purl & Loop) with a gauge specification of 12 grooves per inch. The warp yarn is first wound through the grooves on both ends of the loom and held taut. The weft yarn is interlaced over and under each successive row (thread) of warp yarn, as illustrated in Figure 4.1a, and then is similarly interlaced back through the fabric in the opposite direction after it passes through the last warp thread. Successive rows of weft threads are compressed together such that the weft number density is ~4-5 times that of the warp. Ultimately, a plain-weave fabric pattern

with a high density of threads in the weft direction (*i.e.*, weft-faced weave) is constructed, as seen in the photographs and optical microscope image in Figure 4.1c and Figure 4.1d.

Thermal measurements are performed for individual fibers pulled out from the flat yarns, twisted yarns, and the woven fabric based on the measurement methodology detailed in Chapter 3, Section 3.2. For the fabric samples, thin strips of material must be cut without fraying of the fabric. Fabric strips ~2 cm long (parallel to the weft) and ~2.5 mm wide are cut using a CO₂ laser (ULS PLS6MW) while the fabric is held under tension in the loom. This fuses the cut edges of the strips and prevents unraveling of the yarns. Note that the width of the fused region is very small compared to the width of the fabric and does not influence the thermal measurements for the fabric strip.

4.2 Results and Discussion

In this section, the infrared thermal characterization results of the Dyneema yarn and woven fabric are presented, followed by the thermal measurement results for the individual fibers. The trends in effective thermal conductivity as the material is scaled from fibers to yarns to fabric are explained using reduced-order thermal models. Finally, the key findings of this work are compared with related studies on UHMW-PE materials.

4.2.1 Effective Thermal Conductivity of Yarns

A yarn sample with an effective diameter of ~370 μm is mounted on the heat sink inside the vacuum chamber such that the nichrome heating wire is threaded through the fibers of the bundle to obtain more uniform heating throughout the yarn cross-section. Figure 4.2a shows an example IR temperature map obtained from the measurements in the wire–yarn cross-structure arrangement. Two different temperature maps are obtained at each level of supplied current, one

based on the calibrated emissivity of the wire (in the wire region), and the other based on the calibrated emissivity of the yarn (in the yarn region). These are analyzed to fit for the heat rates Q_L , Q_R , and the temperature gradients in the yarn as shown in Figure 4.2b.

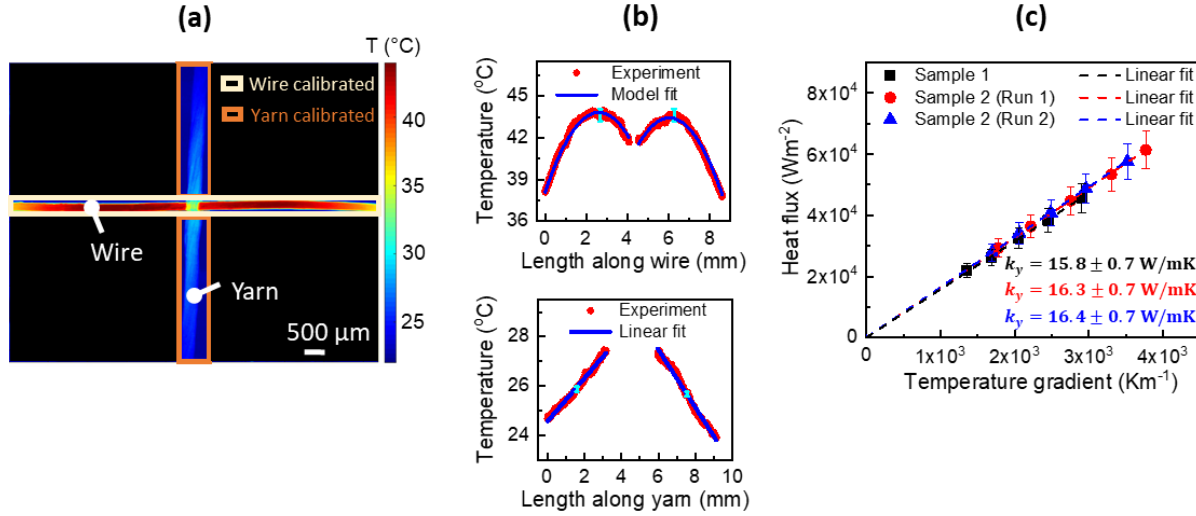


Figure 4.2: (a) IR temperature map of the wire–yarn experiment at a current input of 220 mA. Temperatures shown are based on corresponding emissivity values of the nichrome wire and the yarn, within the regions as indicated. (b) The corresponding temperature profiles used to extract the heat rates and sample temperature gradients are also shown. Representative error bars in the experimental temperature data are shown in cyan near the center of each profile. (c) Heat flux as a function of sample temperature gradient at different levels of input current for two different yarn samples. The slope of the linear fit across all power levels yields the thermal conductivity of the yarn sample. Error bars indicate the calculated uncertainty in heat flux and temperature gradient. Note that uncertainty in the sample temperature gradient is smaller than the data point width.

The heat generation in the junction region of the wire Q_{gen} is also calculated to determine the total heat flux flowing into the yarn sample. This is repeated at five different levels of supplied current. Because the total heat flux ($\{Q_L + Q_R + Q_{gen}\}/A_s$) at each power level is linearly proportional to the sum of the temperature gradients ($|dT/dy|_T + |dT/dy|_B$) on each side (see eq. (3.5)), a single value of thermal conductivity is obtained from the measured slopes by fitting the experimental data to a straight line passing through origin, as shown in Figure 4.2c. This

procedure reduces the measurement uncertainty associated with the experiments. Given the nominal values of all input parameters to the model (e.g., diameter, emissivity, etc.), the thermal conductivity of the yarn (Dyneema SK75) is determined to be $15.8 \pm 0.7 \text{ Wm}^{-1}\text{K}^{-1}$ for a first sample and 16.3 ± 0.7 and $16.4 \pm 0.7 \text{ Wm}^{-1}\text{K}^{-1}$ for two repeated trials of a second sample. As illustrated in Figure 4.2c, the thermal conductivity values measured from the two trials using the second yarn sample are in excellent agreement, indicating good repeatability.

Based on previous studies related to yarn structures ^{123–125}, we note that the level of yarn twist and orientation of fibers within the yarn are important factors that could influence the effective properties of the yarn. With increase in yarn twist, two key mechanisms may affect the heat conduction behavior: (i) increased effective packing of the fibers within the yarn due to compaction, which would lead to an increase in the yarn effective thermal conductivity; and (ii) an increased length of individual fibers per unit of apparent axial conduction length (i.e., an extended path-length for heat conduction following the spiral of the fiber), which leads to a decrease in the yarn effective thermal conductivity. A decrease in yarn thermal conductivity with increasing twist was predicted in ¹²³ by considering the varying helix angle of fibers from the core to the surface of the yarn for an assumed packing arrangement. However, this model only accounts for the increased conduction length due to the oblique orientation of the fibers with respect to the principal yarn axis, without considering the effect of increased compaction ^{124,125}.

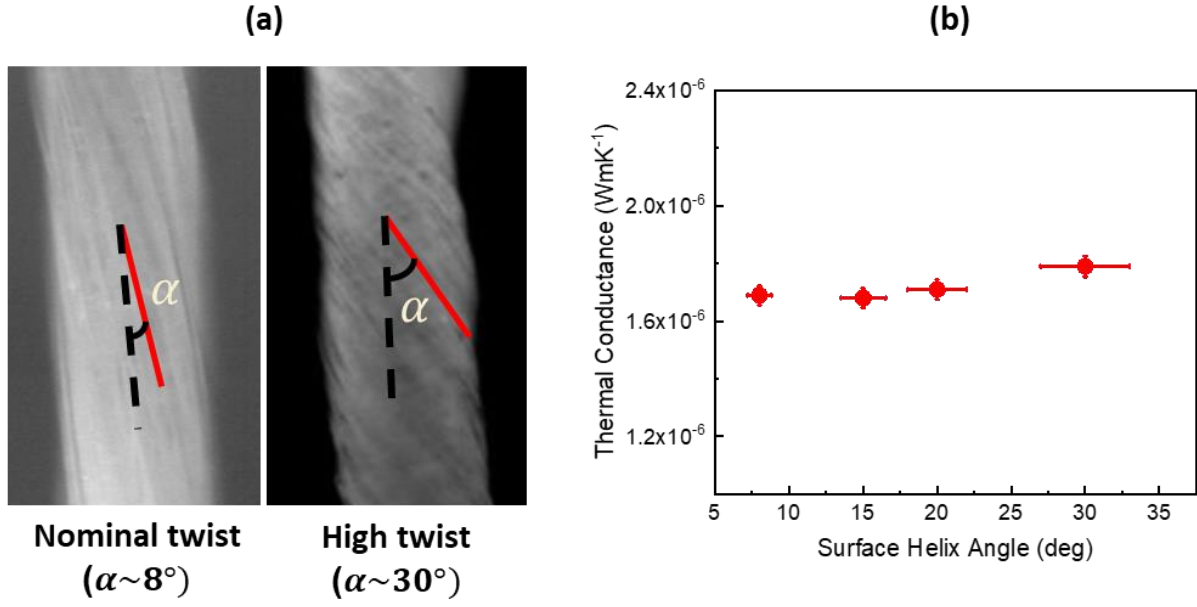


Figure 4.3: (a) Representative *in situ* IR images of yarns in the experimental setup at two different twist levels characterized by a surface helix angle of $\sim 8^\circ$ (low twist) and $\sim 30^\circ$ (high twist). (b) Thermal conductance (product of yarn thermal conductivity and cross-sectional area, $k_y A_y$) measured as a function of surface helix angle of the yarn. Variation of thermal conductance with twist is not very significant ($< 6\%$) for the range of twist levels evaluated.

In the present study, we perform thermal measurements with the twisted yarns to explore the effect of yarn twist on the effective thermal conductance (per unit length) of the yarn. Note that the yarn effective thermal conductance per unit length (with units of WmK^{-1}) is defined as the product of the effective thermal conductivity and the yarn cross-sectional area. This parameter is of interest for fabric construction because it directly influences the in-plane effective thermal properties of fabrics woven from the twisted yarns. The effective thermal conductance can be easily extracted from our measurements without having to consider changes in the effective yarn cross-sectional area at different twist levels. We investigate the effect of yarn twist by performing the IR experiments for four different twist levels characterized by the average surface helix angle of the yarn, as illustrated in Figure 4.3a. The extracted thermal conductance, increases by only $\sim 6\%$ from the lowest to the highest twist level considered here, spanning a surface helix angle

change of about $\sim 20^\circ$, as shown in Figure 4.3b. We conclude from these experiments that the change in yarn thermal conductance is not significant for the range of twist levels characterized here, which is also representative of the twist level of the yarns in the constructed woven fabric.

4.2.2 Effective Thermal Conductivity of Fabrics

A strip of woven fabric having a width of ~ 2.1 mm and thickness of ~ 660 μm is characterized. In order to achieve uniform heating across the fabric thickness and obtain good thermal contact conductance with the heating wire under vacuum conditions, a small piece of copper tape is wound around the fabric in the contact region and a thermal gap pad is placed between the wire and the fabric sample. A schematic drawing of this experimental configuration for fabric testing has been included in Figure 4.4 for clarity. The thermal gap pad helps in conducting a greater amount of heat into the sample at a given level of electrical power input, but does not influence the measured sample thermal conductivity.

A representative IR temperature map for the wire–fabric experiment is shown in Figure 4.5a and the corresponding temperature profiles of the wire and the fabric in Figure 4.5b. For the fabric, a sharp dip in the wire temperature profile is observed on either side of the contact region, which contrasts the wire temperature profile seen for the yarn test in Figure 4.2b. This occurs due to the larger amount of heat being removed by the fabric sample due to its higher thermal conductance as compared to the yarn sample. Analogous to the analysis for the yarn, the total heat flux flowing into the fabric, and the temperature gradients in the fabric region, are obtained for each level of input electrical power. The effective thermal conductivity of the fabric is extracted from the linear fit shown in Figure 4.5c. The radiation losses from the control volume in the central

region of the wire are verified to be negligible ($\sim 1\%$) compared to the total heat rate, $Q_L + Q_R + Q_{gen}$.

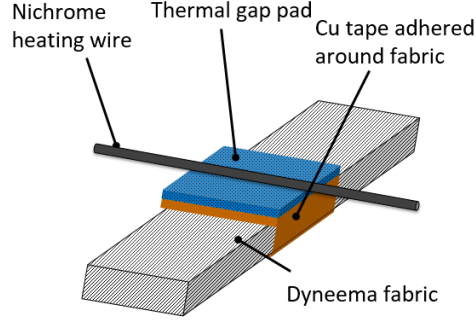


Figure 4.4: Schematic of the experimental configuration used for the thermal measurements for the woven fabric sample.

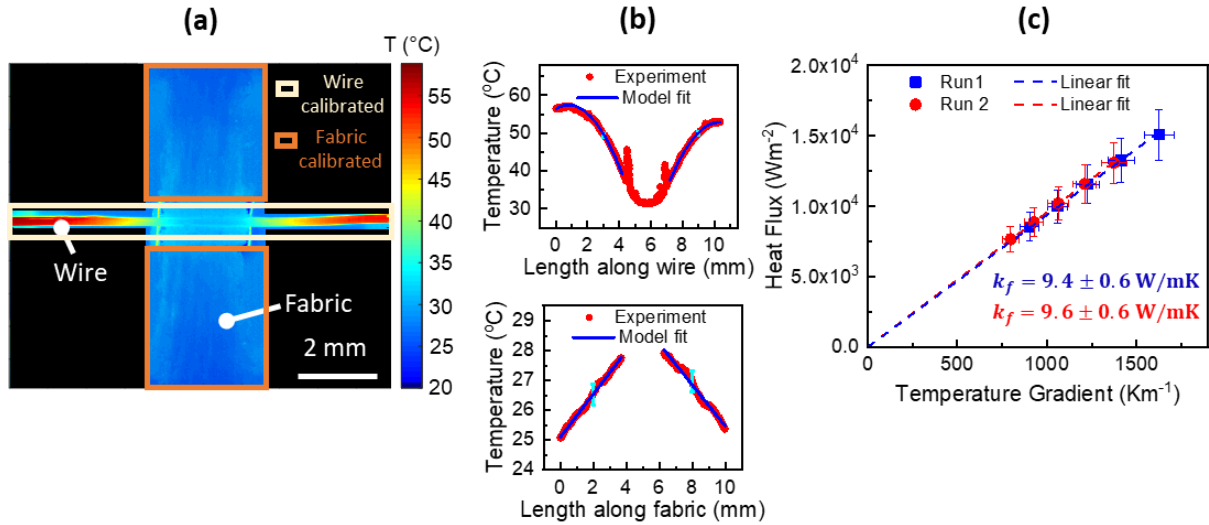


Figure 4.5: (a) IR temperature map of the wire–fabric experiment at a current input of 300 mA. Temperatures shown are based on corresponding emissivity values of the nichrome wire and the fabric, within the regions as indicated, and (b) the corresponding temperature profiles. Representative error bars in the experimental temperature data are shown in cyan near the center of each profile. (c) Heat flux as a function of sample temperature gradient at different levels of input current for different experimental trials: Run 1 is performed with the thermal gap pad between the wire and fabric for enhanced thermal contact, while Run 2 is performed without this pad. The slopes of the linear fit from both runs are extracted to calculate an average fabric thermal conductivity of $\sim 9.5 \pm 0.6 \text{ Wm}^{-1}\text{K}^{-1}$.

The effective thermal conductivity of the fabric is determined to be $9.5 \pm 0.6 \text{ Wm}^{-1}\text{K}^{-1}$ based on the two experimental trials shown in the Figure 4.5c. The first trial (Run 1) is performed with the thermal gap pad placed in between the wire and the fabric to enhance thermal conductance at the junction, while the second trial (Run 2) is performed without the use of this pad. The results from these two independent runs yield the same value of thermal conductivity to within measurement uncertainty, which further demonstrates that the developed characterization technique is independent of the junction thermal contact resistance.

In order to obtain an estimate of effective fabric thermal conductivity to compare with our experimental results, and to also understand the effect of yarn density on fabric conductivity, we have developed a reduced-order heat conduction model. In this model, a full nodal-network-based analysis similar to the approach implemented for modeling conduction through foam structures in ¹²⁶ is performed. Effective fabric thermal conductivity along a given direction of interest is calculated by assigning constant temperature boundary conditions T_H and T_C to the associated opposite fabric ends, while insulating the other two sides as shown in Figure 4.6a. As a result, heat is conducted at steady state along one set of orthogonal yarns (blue yarns) oriented in the y direction. The model considers the thermal resistance to heat flow through yarn segments between cross-over locations and defines a node temperature at each cross-over. The nodal temperature at some cross-over location (node ‘P’) for a given yarn is related to the neighboring nodal temperatures along the same yarn (nodes ‘N’ and ‘S’) via segment thermal resistances, and to the nodal temperature of the orthogonally oriented yarn (node P’) via a contact thermal resistance.

Energy balance equations are written at each node of the resistance network to obtain a system of linear equations which is solved to obtain all nodal temperatures based on the fixed

boundary conditions. Finally, the effective fabric thermal conductivity in the direction of interest (along y) is obtained as follows:

$$k_{eff} = q \left\{ \frac{l_{eff}}{(T_H - T_C)A_{eff}} \right\}, \quad (4.1)$$

where q is the rate of heat flow along the y direction, l_{eff} is the total length of heat flow in the considered network, and A_{eff} is the effective cross-sectional area of the network defined as the area of the rectangular envelope around the fabric weave as shown in the cross-section depictions in Figure 4.6b. Note that the calculated effective thermal conductivity becomes independent of the size of the nodal network and the input boundary temperatures. Further, for a plain-weave fabric, the effective thermal conductivity in the direction under consideration is independent of the inter-yarn thermal contact resistance at the nodal locations, because the yarns oriented perpendicular to the direction of heat flow (along x) are insulated at their end and therefore non-participating. As a result, an inter-yarn thermal contact resistance between orthogonal yarns does not need to be specified in this case.

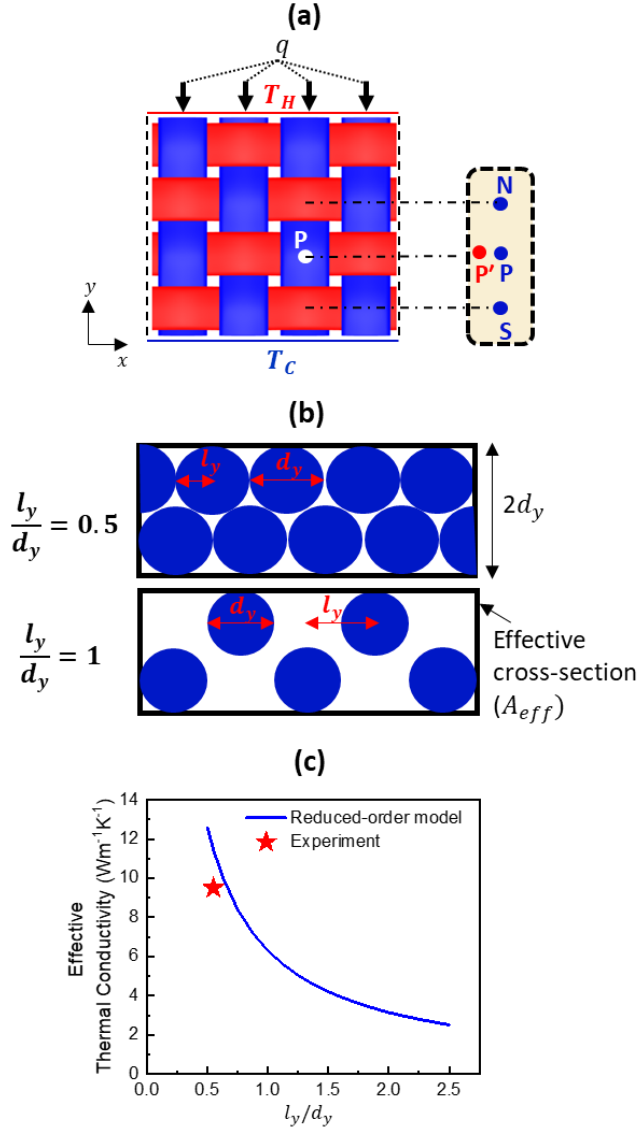


Figure 4.6: (a) Schematic drawing (top-view) of a plain-weave fabric showing the heat transfer nodal-network associated with the reduced-order model to calculate the effective thermal conductivity of the fabric in the y direction (along the blue yarns). The neighboring nodes associated with a node 'P' on a particular blue yarn are also shown in the inset to illustrate node connectivity. (b) Schematic drawings of the plain-weave fabric cross-section, showing only the blue yarns that participate in heat conduction. These drawings illustrate the effective area-based packing fraction for a loose fabric ($l_y/d_y = 1$) as compared to a tight fabric ($l_y/d_y = 0.5$). (c) Effective thermal conductivity as a function of l_y/d_y as predicted by the reduced order model. The measured fabric thermal conductivity from the experiments is shown as a 'star' symbol and agrees well with the prediction from the reduced-order model.

Based on the results from the reduced-order model, the effective fabric thermal conductivity of the plain-weave fabric is dependent on three model input parameters: the yarn thermal conductivity (k_y), the center-to-center spacing between adjacent parallel yarns (l_y), and the effective yarn diameter (d_y). The schematics in Figure 4.6b portray the effective cross-sections of a fabric with a high packing density ($l_y/d_y = 0.5$) and low packing density ($l_y/d_y = 1$) of yarns parallel to the heat flow direction. From this model, the effective thermal conductivity is determined to be directly proportional to the cross-sectional area-based packing fraction of the yarns oriented along the direction of heat flow. Specifically, as illustrated in the plot in Figure 4.6c, the effective fabric thermal conductivity is inversely proportional to l_y/d_y for a given value of k_y , which is taken to be $16 \text{ Wm}^{-1}\text{K}^{-1}$ based on the results obtained from the yarn characterization experiments. From inspection of the images of the woven fabric shown in Figure 4.1d, a value of $l_y/d_y \sim 0.5\text{-}0.6$ is representative of the experimentally characterized woven fabric. At this packing density, the estimate of effective fabric conductivity from the reduced-order model matches well with the result from the thermal characterization experiment, as shown in Figure 4.6c. Further, the results obtained from the reduced-order model also offer quantitative understanding of the effect of yarn packing in the fabric weave on effective fabric thermal conductivity.

4.2.3 Thermal Characterization of Fibers

The thermal measurements for individual UHMW-PE fibers are based on the same measurement principle as that of the yarns and the fabrics. However, because the diameter of an individual fiber is $\sim 20 \text{ }\mu\text{m}$, which is an order of magnitude smaller than that of the yarns, a higher magnification IR lens with a pixel resolution of $3.03 \text{ }\mu\text{m}$ is used in these measurements. Additionally, a nichrome heater wire with a much smaller diameter is needed to achieve the

required sensitivity in the measurements in terms of obtaining a measurable dip in the wire temperature profile to quantify the heat flow into the sample. The wire is coated by dipping in a colloidal graphite solution to increase its emissivity, and the diameter of the wire after coating is ($\sim 80\text{ }\mu\text{m}$) measured *in-situ* during the IR measurement. The fiber is not coated because the coating procedures used for the individual fibers significantly increase the effective fiber diameter which would impact its measured effective thermal conductivity.

Due to the much smaller length scales involved, these measurements are more challenging in terms of sample preparation (coating procedures) and sample setup (placing the individual fiber in proper orthogonal contact with the heater wire). Also, individual fibers have a relatively low surface emissivity (~ 0.27 in the associated IR range), and appropriate emissivity calibration must be used to extract the temperature maps without the aid of a high emissivity coating. Further, the field of view of the experimental cross-structure arrangement in these IR measurements is limited to an area of $\sim 3.1\text{ mm} \times \sim 3.1\text{ mm}$ around the central region of the wire and fiber. Therefore, the suspended length on each side of the wire and sample available for extraction of temperature profiles is only $\sim 1.5\text{ mm}$ (see Figure 4.7). For this reason, the temperature rise due to heat generation on each side of the wire is very small ($\sim 1\text{-}2^\circ\text{C}$), and the heat rate conducted into the fiber is low, on the order of $0.01\text{-}0.1\text{ mW}$ across all power levels. Therefore, the estimation of heat rates leaving the wire based on fitting the experimental temperature profiles to a heat transfer model (as done in case of the yarn and fabrics) involves higher uncertainty and sensitivity.

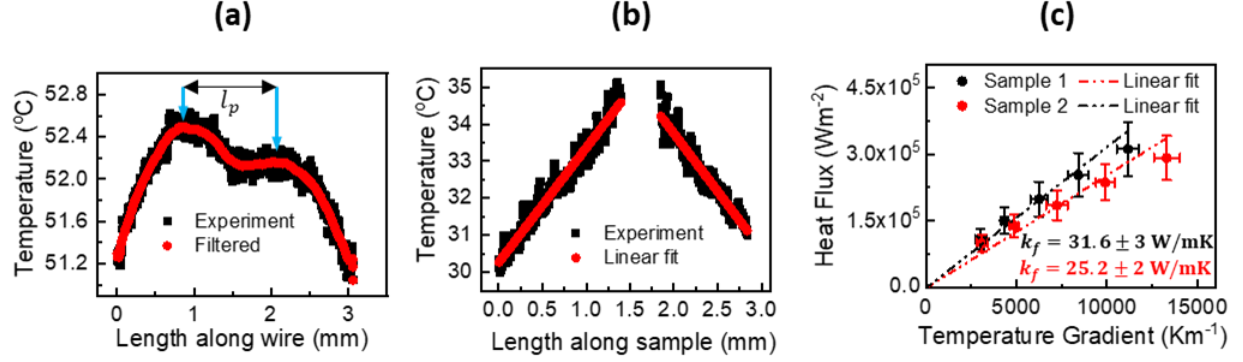


Figure 4.7: (a) Representative experimental and filtered (based on a moving average) temperature profiles of the nichrome wire at an electrical power input of 14 mA. The peak-to-peak distance, l_p is shown, which is used to extract the heat rate entering the fiber, and (b) corresponding experimental temperature profiles and linear-fits of the two sides of the fiber sample. (c) Heat flux as a function of the sample temperature gradient. The linear fit across power levels yields fiber thermal conductivity.

To address some of these challenges, we use a simpler analysis to extract the heat transfer rate from the wire to the fiber sample that avoids the need to perform the wire-only calibration experiment, which helps in reducing the uncertainty involved in this case. We find that a measurable peak is obtained in the experimental temperature profiles on each side of the wire. The heat rate conducted out of the wire can be extracted based on the heat generation within the region between the peaks on each side of the wire. All the heat generated in this region (after appropriately accounting for radiation losses) must flow into the fiber sample at steady state; the heat generated in the region outside the peaks is conducted out to the heat sink and does not flow into the fiber sample. Specifically, because the electrical resistance of the wire is known by measurement, and the electrical current supplied to the wire is known, the total heat generation in the region between the peaks is given by $Q_{gen} = I^2 R_l l_p$, where l_p is the distance between the temperature peaks on each side of the wire. The total heat transferred to the sample is then given by $Q = Q_{gen} - Q_{rad}$, where Q_{rad} is the radiation loss from this region of length l_p . Note that $Q_{rad} = \sigma \epsilon_w \pi d_w l_p (T_{avg}^4 -$

T_{surr}^4), where T_{avg} is the average wire temperature in this region and ε_w is the surface emissivity of the wire. The temperature gradients on each side of the sample are determined from the temperature profiles of the fiber and the thermal conductivity of the fiber (with cross-sectional area A_f) is calculated as:

$$k_f = \frac{Q}{A_f \left\{ \left| \frac{dT}{dy} \right|_T + \left| \frac{dT}{dy} \right|_B \right\}} \quad (4.2)$$

Figure 4.7a shows the wire temperature profile extracted from the IR temperature map in the available field of view for a given power level. The peak-to-peak distance in the temperature profile l_p is determined from this plot as shown. The associated uncertainty in this calculation is also estimated based on observing the change in l_p when using differing window sizes to filter the experimental wire temperature profiles. Figure 4.7b shows the corresponding temperature profiles of the fiber sample based on its calibrated emissivity. As in the experimental procedure described for the yarns and fabrics, the measurements are performed at five different power levels and the total heat flux and temperature gradient are extracted at each power level. The thermal conductivity of the fiber is determined from the slope of the linear fit across the different power levels as shown in Figure 4.7c. Based on measurements performed for two different fiber samples, an average thermal conductivity of $28.4 \pm 3 \text{ Wm}^{-1}\text{K}^{-1}$ is obtained. The thermal diffusivity of the individual fibers is also measured using the micro-IR Angstrom method described in Chapter 3, Section 3.1. Individual filaments are setup to be orthogonally oriented in contact to a nichrome wire, and a periodic square wave electrical power input is applied to the wire. The measurements are performed at different levels of electrical current at a fixed periodic heating frequency of 100 mHz. The thermal diffusivity of the fibers is extracted using the amplitude ratio and phase lag as a function of the length of the sample. The results of these measurements are shown in Figure 4.8 at

different values of temperature amplitude which arise due to the different levels of electrical power input.

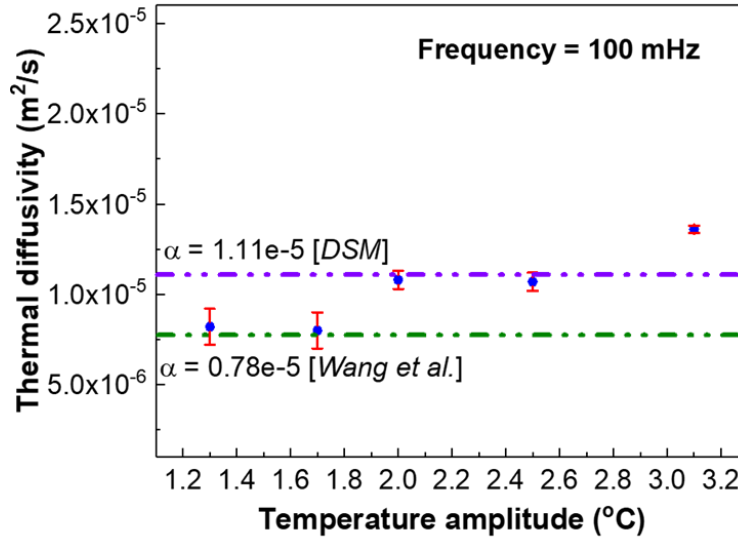


Figure 4.8: Measured thermal diffusivity as a function of temperature amplitude as a result of different levels of electric current supplied to the heater wire. The dashed lines show a comparison from two other references ([41], [46]) based on the extracted thermal diffusivity (from measured thermal conductivity) using standard values of density and heat capacity for UHMW-PE.

The measured thermal diffusivity is in the range of $\sim 0.78 \times 10^{-5} \text{ m}^2/\text{s}$ to $\sim 1.35 \times 10^{-5} \text{ m}^2/\text{s}$ which corresponds to a thermal conductivity range of 15 to 24 $\text{Wm}^{-1}\text{K}^{-1}$ based on standard values of density and specific heat capacity specified for UHMW-PE materials. This is in generally good agreement with measured values of thermal conductivity for similar fibers ^{41,46}, and with the direct thermal conductivity measurements performed using the steady state IR technique described in this work. Slight discrepancies may be due to the assumption of standard values of specific heat and density to extract thermal conductivity from thermal diffusivity which can potentially vary across fiber samples.

4.2.4 Discussion

The results from the thermal characterization study presented in the previous sections indicate a very high measured thermal conductivity for UHMW-PE yarns and fabrics, especially considering that these are constructed out of polymer fibers. To interpret these measured thermal conductivities, we have also characterized the individual fibers (monofilaments with diameter $\sim 20\ \mu\text{m}$) that comprise the yarn and fabric as detailed in the previous section. In this section, we compare the results from this work to other relevant thermal studies on UHMW-PE materials.

Consider the thermal conductivity of oriented UHMW-PE as the material is scaled from fibers to fabrics, as illustrated in Figure 4.9a. Our measurements in this work reveal that the effective thermal conductivity of UHMW-PE only reduces by a factor of ~ 3 as microfibers are scaled up to woven fabrics. This reduction is attributed mainly to the packing density of individual fibers within a yarn, and the packing density of yarns within a fabric. The effective density of yarns, based on measuring the yarn linear density and assuming a circular cross-section, is determined to be $\sim 460\ \text{kg/m}^3$, which is lower than the specified density of an individual fiber by a factor of ~ 2 . This is the same factor of reduction in effective thermal conductivity from fibers to yarns as measured. Further, the results from the reduced-order fabric thermal conductivity model explain this same reduction due to packing density from the yarns to the woven fabric. Nevertheless, given these fabrics are a macroscale material, their effective thermal conductivity ($\sim 10\ \text{Wm}^{-1}\text{K}^{-1}$) is remarkable compared to a bulk form of polyethylene ($\sim 0.5\ \text{Wm}^{-1}\text{K}^{-1}$ for HDPE).

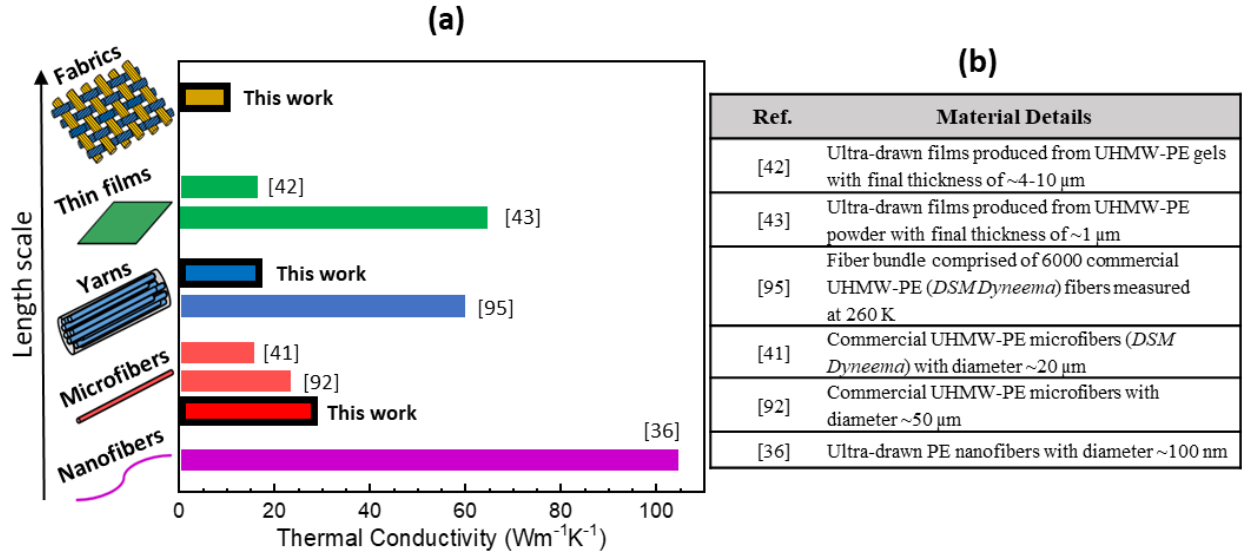


Figure 4.9: (a) Thermal conductivity of various forms of UHMW-PE measured in the literature and the present study. The thermal conductivity for each material is reported using a bar along the horizontal axis scale, with bars organized into groups of similar form and groups shown in order of increasing length scale. Details of the materials are listed in (b).

Comparing to the values in literature, as apparent from Figure 4.9, our measured thermal conductivity of the individual fibers is generally in good agreement with other studies^{41,92}. The thermal conductivity of fiber bundles measured in⁹⁵ are much higher compared to our measurement for the yarns. However, we note that radiation losses and parasitic conduction losses were not considered in the conventional steady-state measurement technique used in this previous study⁹⁵, which would tend to overestimate the thermal conductivity. Further, as pointed out in [41], the value of thermal conductivity directly measured for the fiber bundle ($\sim 60\text{ Wm}^{-1}\text{K}^{-1}$) in⁹⁵ does not agree with the thermal conductivity extracted from the thermal diffusivity measurement ($\sim 36\text{ Wm}^{-1}\text{K}^{-1}$) in the same work⁹⁵, as well as with that extrapolated from the measurement of the fiber-reinforced plastic (in⁹⁵) comprising of the same fibers ($\sim 33\text{ Wm}^{-1}\text{K}^{-1}$). Our measurements for yarns also corroborate the measurements of individual microfibers^{41,61,92}, as a reduction in

effective conductivity (and not an increase) is expected for yarns when compared to individual fibers due to a decrease in effective density.

Figure 4.9 also indicates that ultra-drawn oriented thin films^{42,43} can have a similar thermal conductivity to individual fibers. The recent study by Xu *et al.*⁴³ demonstrates great potential for scalability of these films along the drawing direction, but the drawing process required to obtain such high thermal conductivity also greatly reduces the thickness. Therefore, even though the thermal conductivity of the fabricated films increases from $0.38 \text{ Wm}^{-1}\text{K}^{-1}$ to $62 \text{ Wm}^{-1}\text{K}^{-1}$ as the draw ratio increases to 110, the thermal conductance (per unit length) of these films across all draw ratios is limited to relatively low values in the range of $2.9 \times 10^{-7} \text{ WmK}^{-1}$ to $3.9 \times 10^{-7} \text{ WmK}^{-1}$. To address this scalability limit in the thickness direction, Xu *et al.*⁴³ also demonstrated construction of a $150 \text{ }\mu\text{m}$ -thick laminate by hot-pressing many films produced at a high draw ratio of 50, and measured the in-plane thermal conductivity of the laminate to be $\sim 33 \text{ Wm}^{-1}\text{K}^{-1}$. The thermal conductance of this fabricated 100-layer laminate (in⁴³) is $\sim 5 \times 10^{-6} \text{ WmK}^{-1}$, while the conductance of the single-layer woven fabric test strip (from this work) is $1.3 \times 10^{-5} \text{ WmK}^{-1}$. The woven fabric strip has a thermal conductance 2.6 times greater primarily due to its higher length scale compared to the film laminate. We note that while the high thermal conductivity of the laminate is very promising for heat spreading applications, effective scaling-up of these structures while maintaining these properties is crucial for such applications. The ultra-drawing process constrains the cross-sections that can be achieved for the produced films, whereas single-layer weaves can easily be scaled along the width and length directions. Also, laminates of larger thickness prepared in this manner may be stiffer as compared to woven materials which can potentially limit their usage in flexible device applications.

Based on the results of the current study, woven fabrics show great promise for scalable fabrication of a high effective thermal conductivity material because weaves with lengths and widths on the order of meters, and thicknesses on the order of ~ 0.5 -1 mm, can easily be produced by a large-scale textile manufacturing process. Further, the in-plane thermal conductivity of UHMW-PE fabrics is more than two orders of magnitude higher than conventional fabrics such as cotton (0.03 - $0.07 \text{ Wm}^{-1}\text{K}^{-1}$), silk ($0.09 \text{ Wm}^{-1}\text{K}^{-1}$), and wool ($0.04 \text{ Wm}^{-1}\text{K}^{-1}$)^{127–129}. Therefore, UHMW-PE fabrics are ideally suited to wearables and other flexible device applications where good heat spreading functionality is desired. Additionally, complex weaves and multi-layer fabric stacks provide an avenue to tailor the high thermal conductivity of these materials to a particular application.

CHAPTER 5. THERMAL AND MECHANICAL CHARACTERIZATION OF COMMERCIAL HIGH-PERFORMANCE POLYMER FABRICS

In this chapter, we explore high-performance polymer-based engineered textile materials with specific interest in their heat conduction behavior, while also considering relatively mechanically flexible materials. Based on a survey of commercially available materials, we first identified and acquired several commercial fabrics consisting of UHMW-PE (Dyneema®) to characterize their properties that are relevant for wearable heat spreading applications. Specifically, the effective thermal conductivity and bending stiffness of these commercial Dyneema®-based are measured using custom-developed thermal and mechanical metrology techniques. We also perform measurements for an in-house woven fabric constructed entirely from Dyneema® fibers, as well as other conventional materials, in order to benchmark their performance. Further, we experimentally investigate the impact of creasing and thermal annealing of the fabrics on their effective thermal behavior to develop a better understanding of their potential for long-term use in wearable device applications. *The content in this chapter has been adapted from a recent manuscript draft submitted for publication and currently under review.*

5.1 Materials Survey and Selection

In this section, the reported thermal and mechanical properties of commercially available polymer materials are surveyed, which serves as the basis for selection of the fabrics characterized in this study. Commercially available high-performance fiber materials that could potentially be integrated in advanced textiles are first identified. Then, a material having desirable properties for

applications in wearable device thermal management is selected. Finally, existing textile/fabric products constructed from these fibers are acquired for subsequent characterization.

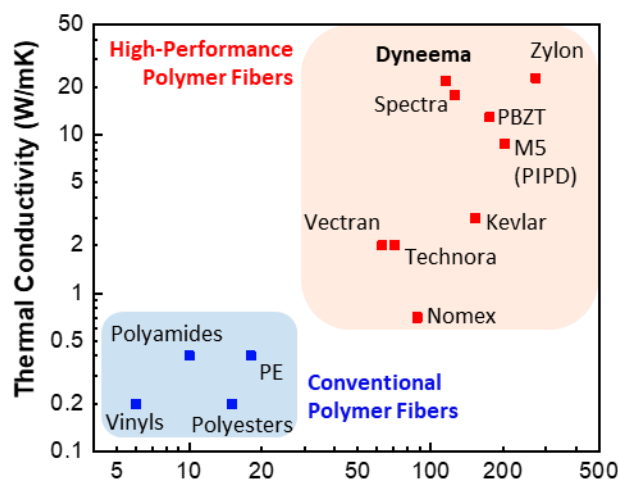


Figure 5.1: Elastic modulus and thermal conductivity of conventional polymer fibers (in blue) and commercially produced high-performance polymer fibers (in red). The high-performance polymer fibers typically have ~1-2 orders of magnitude higher thermal conductivity and elastic modulus (note the log scales). Data compiled from references with details for the high-performance fibers summarized in Table 5.1.

The two primary properties of interest are the elastic modulus and thermal conductivity. These properties are cataloged for various commercially produced high-performance fibers in Figure 5.1, with details summarized in Table 5.1. Compared to conventional polymers, these materials have over an order of magnitude higher elastic moduli and thermal conductivities, typically greater than 50 GPa and $1 \text{ Wm}^{-1}\text{K}^{-1}$, respectively. Among these materials, we identify Dyneema®, a commercial gel-spun microfiber made of UHMW-PE, as a suitable starting material for the current study due to its standout thermal conductivity ($20\text{-}30 \text{ Wm}^{-1}\text{K}^{-1}$) and availability. The relatively lower elastic modulus of Dyneema® as compared to other highest thermal conductivity materials, such as Zylon®, is also an advantage in applications involving flexible substrates and devices.

The identified commercial Dyneema®-based fabrics, the in-house fabricated sample constructed entirely from Dyneema® fibers, and benchmarking materials considered in the present study are summarized in Table 5.2, along with a sample identifier used for each material. The commercial fabrics include two types of Dyneema® denim fabrics (labelled “Dyneema® Black” and “Dyneema® BW”) and a Dyneema® composite fabric (labelled “Dyneema® Composite”) acquired from Rockywoods Fabrics LLC. As illustrated in Figure 5.2a, the denim fabrics consist of a specially engineered double-warp weave configuration comprising Dyneema® yarns along the warp and weft directions of the fabric, and cotton yarns along the warp. The composite fabric is made up of a grid of Dyneema® fibers sandwiched between polymer films to form a UHMW-PE composite laminate, with a polyester weave is attached on one face (see Figure 5.2b). The in-house fabricated sample (100% Dyneema®) is a plain-weave Dyneema® fabric constructed entirely from Dyneema® SK75 microfibers (Atkins and Pearce Inc.) as described in our previous work ¹¹⁰. Additionally, we acquire some conventional materials with no UHMW-PE content for benchmarking purposes: EeonTex®, a non-woven fabric that is commonly used as a heater fabric in electronic textiles; a high-density polyethylene (HDPE) flexible sheet (McMaster-Carr); and a typical cotton twill weave fabric (tested for mechanical properties only).

Table 5.1: Details of the different high-performance polymer fibers (shown in Figure 1)

Fiber	Fiber Type	Fabrication Method	Tensile Modulus (GPa)	Ref	Axial Thermal Conductivity ($\text{Wm}^{-1}\text{K}^{-1}$)	Ref	General Properties
Dyneema®	Ultra-High Molecular Weight Polyethylene (UHMW-PE)	Gel-spinning process using spinneret (super drawing, heating, elongating, and cooling)	101 113	41 131	14.2 23.6 28.4 22.5	41 130 110 132	High strength to weight, abrasion resistance, mechanical strength, thermal conductivity
Spectra®	Ultra-High Molecular Weight Polyethylene (UHMW-PE)	Gel-spinning process	118 113	41 131	15.8 20	41 93	High strength to weight, abrasion resistance, mechanical strength, thermal conductivity
Zylon®	Polybenzoxazole (PBO)	Spun from Polyphosphoric acid (PPA) solutions via dry-jet wet spinning	275 270	41 133	23 22.6	41 130	Very high mechanical strength, excellent heat resistance; very low thermal conductivity
PBZT	Poly (p-phenylene benzobisthiazole)	Dry-jet wet spinning	202 150	41 134	12.5	41	High modulus and high strength
PIPD (M5)	Polyhydroquinone-diimidazopyridine	Condensation polymerization followed by extrusion	76 330	41 133	8.8	41	High strength, modulus, and thermal stability
Kevlar®	Aromatic polyamide (para aramid)	Liquid-crystalline polymer produced by wet/dry-jet wet spinning	120 185	41 133	3.1	41	High strength, toughness, thermal stability, flame resistance
Vectran®	Aromatic polyester	Melt spinning / extrusion from liquid crystal polymer	60 65	41 133	1.7 2.5	41 135	High tensile and impact strength, abrasion resistance
Technora®	Aromatic copolyamide (para aramid)	Condensation polymerization followed by spinning and drawing	71	133	1.98	136	High heat and chemical resistance, strength, and dimensional stability
Nomex®	Meta aramid	Condensation reaction followed by spinning and drawing	88	137	0.65	136	Intrinsically flame resistant, high temperature resistant

Table 5.2: Summary of the materials considered in this study

Material Category	Sample Identifier	Description
Dyneema® (UHMW-PE) fabrics	100% Dyneema®	Plain-weave fabric woven in-house, consists of Dyneema® SK75 yarns along warp and weft directions, with 4-5 times higher yarn density along weft
	Dyneema® Black	Commercial double weave denim consisting of Dyneema® and cotton warp yarns, and Dyneema® weft yarns (<i>Supplier Specification: 62% Dyneema®, 38% cotton</i>)
	Dyneema® BW	Commercial double weave denim consisting of Dyneema® and cotton warp yarns, and Dyneema® weft yarns; some amount of polyamide and elasthane are present to provide stretch (<i>Supplier Specification: 52% Dyneema®, 37% cotton, 9% polyamide, 2% elasthane</i>)
	Dyneema® Composite	Dyneema® fiber-reinforced polymer composite with polyester weave (<i>Supplier Specification: 15% Dyneema®, 65% polyester, 20% other polymer film</i>)
Benchmarking Materials (No UHMW-PE)	EeonTex®	Non-woven conductive e-textile heater fabric consisting of a polyester/nylon blend
	HDPE sheet	Bulk material sheet made of high-density polyethylene
	Cotton	Conventional cotton cloth

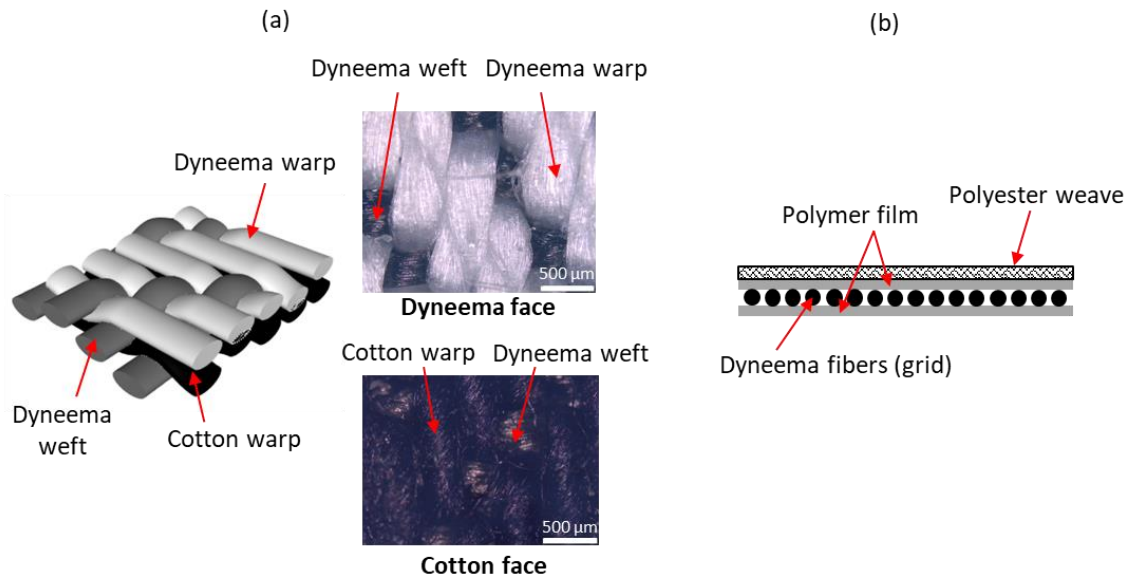


Figure 5.2: Representative schematics of the commercial Dyneema® fabric samples: (a) the Dyneema® denim fabric weave structure consisting of Dyneema® and cotton yarns, with optical micrographs of the Dyneema® and cotton faces for the Dyneema® Black fabric shown as an example. (b) the Composite Dyneema® fabric sample consisting of a grid of Dyneema® fibers sandwiched between polymer films, with a polyester weave attached on one face.

5.2 Experimental Methods

5.2.1 Thermal Metrology

The in-plane thermal conductivity of the fabrics is measured using an in-house thermal measurement technique based on infrared microscopy. A brief description of this method is provided here and details of this technique are reported in our recent work ¹¹². As seen in Figure 5.3a, the fabric sample is heated using a current-carrying nichrome wire placed orthogonally in contact with a strip of the fabric. The simultaneous measurement of the wire and fabric sample temperature profiles using a high-resolution infrared microscope (Quantum Focus Instruments) in a vacuum environment enables extraction of the effective in-plane thermal conductivity of the sample. For each fabric sample, five steady-state temperature datasets are recorded at different power levels (in the range of ~75-175 mW) to extract a single, average value of thermal conductivity so as to improve confidence and reduce uncertainty in the measured results. The approach for calculation of uncertainties in the measured thermal conductivity is described in ¹¹². These measurements yield the in-plane thermal conductivity of the fabric samples.

5.2.2 Mechanical Metrology

To quantify the mechanical flexibility of the fabric samples, we characterize the bending stiffness (or flexural rigidity), which is a measure of the resistance to bending offered by the fabric material. We use an experimental approach for measuring fabric bending stiffness in accordance with the principle of the Pierce Cantilever Test and the ASTM D1388 standard ¹³⁸. For this purpose, a bending test fixture is designed and fabricated.

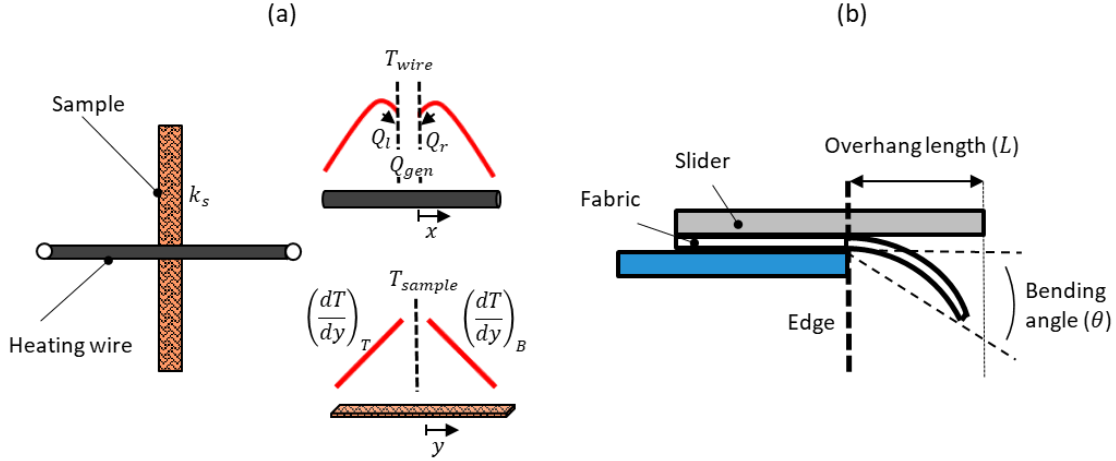


Figure 5.3: (a) Schematic representation of the thermal metrology setup showing a heating wire orthogonally oriented in contact with the test sample to be measured (left). Representative temperature profiles of the wire and sample shown (right) are captured using an infrared microscope. Heat rates (Q_l and Q_r) are determined from the wire temperature profile, and the temperature gradients ($(\frac{dT}{dy})_T$ and $(\frac{dT}{dy})_B$) in the sample are used to calculate the sample thermal conductivity k_s . (b) Illustration of the principle of the bend testing metrology, where the overhang length L and bending angle θ of a fabric under its own weight enables quantification of the bending stiffness.

In this test, a fabric sample is placed under a weighted slider and manually slid over the edge of the fixture until the end of the fabric bends under its own weight to a prescribed angle (typically 41.5°). The bending stiffness of the fabric is quantified based on the overhang length and bending angle as illustrated in Figure 5.3b. We note that the most recent version of the ASTM standard ¹³⁸ includes unexplained and ambiguous constants, as also discussed by Lammens *et al.* ¹³⁹. Therefore, in this work, the bending stiffness (G) (units of Nm) is calculated based on the traditional Pierce equation as follows:

$$G = WC^3, \quad (5.1)$$

where W is the weight per unit area (in N/m^2) and C is the bending length (in m). The overhang length (L) shown in Figure 5.3b is measured to determine the horizontal length moved when the sample reaches the specified bend angle. This length is then used to calculate the bend length, C :

$$C = f(\theta)L, \quad (5.2)$$

where θ is the bend angle at which the overhang length is measured and $f(\theta)$ is given by

$$f(\theta) = \left[\frac{\cos(\frac{\theta}{2})}{8 \tan(\theta)} \right]^{\frac{1}{3}}. \quad (5.3)$$

The two key parameters, L and θ , are measured using scale rulers attached to components of the cantilever test fixture. To measure the overhang length (L), a weighted slider with an attached scale is always kept in contact with the fabric during the test. The displacement of the slider is the overhang length of the fabric, which is read from the scale at the end of the test. For the bending angle (θ), two sets of protractors are etched into transparent acrylic plates on both sides of the overhanging fabric sample. The uncertainties in this measurement are calculated via a standard propagation of errors in the measurement of the overhang length, $L (\pm 1 \text{ mm})$ and bending angle, $\theta (\pm 2^\circ)$. Additionally, a validation of the measurement approach is provided in Appendix A by comparing the measurements for a Kapton® (polyimide) film to the calculated value from plate theory.

5.3 Results and Discussion

5.3.1 Thermal Conductivity

In this section, we report the results of the thermal conductivity characterization for the samples in Table 5.2. The HDPE, EeonTex®, and Dyneema® composite samples are isotropic in the in-plane direction, while the woven Dyneema® denim and 100% Dyneema® fabrics are anisotropic due to differing yarn materials and densities along the warp versus weft directions. For these fabrics, the thermal conductivity is measured along the high-density direction of constituent

yarns, which is along the weft for the 100% Dyneema® fabric and along the warp for the Dyneema® denim fabrics.

During the thermal measurements, the in-plane heat spreading behavior of the sample can be qualitatively understood from the steady state temperature profiles. In the wire-sample arrangement, a higher thermal conductivity sample will dissipate more heat from the heater wire at the same input power. This is observed as a relatively steeper temperature drop in the wire in the direction toward the point of contact with the sample. Additionally, a higher thermal conductivity sample will exhibit a more linear temperature profile in the sample due to heat conduction along the sample dominating compared to radiation loss to the surroundings¹¹⁰. These heat transfer mechanisms (conduction and radiation) are of comparable magnitude for a low conductivity sample leading to a non-linear decaying temperature profile. These qualitative trends are illustrated in Figure 5.4a and Figure 5.4b, which show representative temperature profiles of the heater wire and the fabric sample for experiments with Dyneema® BW and EeonTex® samples at the same total input power of ~100 mW. The temperature of the heater wire (Figure 5.4a) is significantly lower for the Dyneema® BW fabric compared to the EeonTex®, and the temperature gradient approaching the contact region with the sample is steeper. Further, the temperature of the sample (Figure 5.4b) is also lower on average and has a near-linear profile for the Dyneema® BW fabric, whereas there is a clear exponential trend in temperature (and higher average) for the EeonTex® sample.

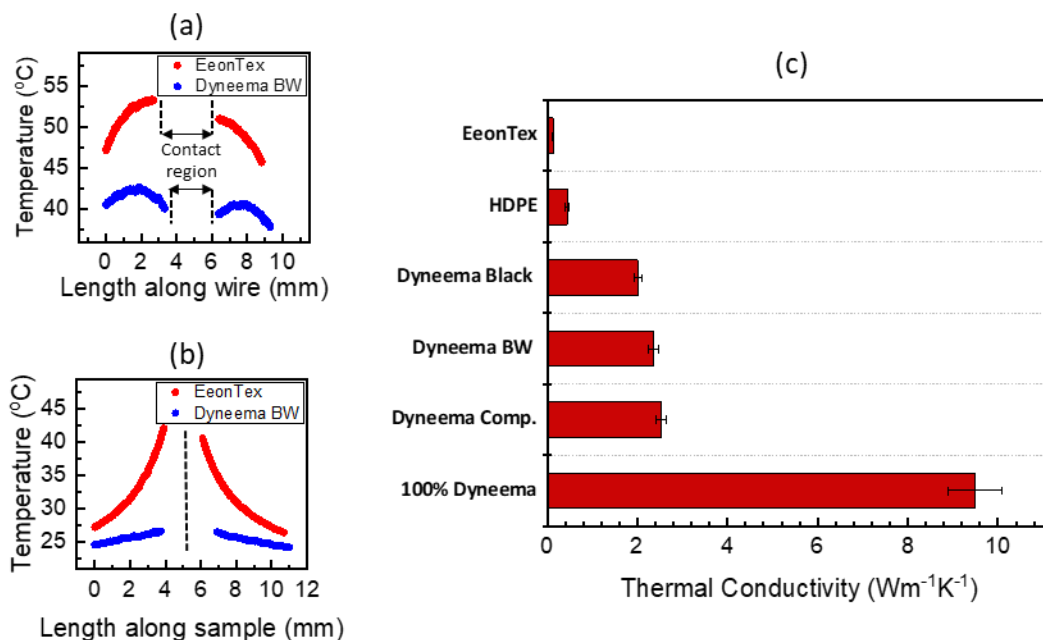


Figure 5.4: Representative temperature profiles of (a) the heating wire and (b) fabric sample obtained from IR thermal measurements of the Dyneema® BW and EeonTex® samples at the same electrical power input. The Dyneema® BW sample exhibits significantly lower wire and sample temperatures, a steeper temperature gradient in the wire approaching the central region, and a relatively more linear sample temperature profile, which all are indicative of a higher in-plane thermal conductivity. (c) Measured effective in-plane thermal conductivity for the different samples.

Based the measurements, the effective in-plane thermal conductivity for each sample is calculated, and these results are summarized in Figure 5.4c. The commercial Dyneema®-based fabrics have thermal conductivities in the range 2-2.5 Wm⁻¹K⁻¹, and the 100% Dyneema® fabric has a thermal conductivity of 9.5 Wm⁻¹K⁻¹. This is a significantly higher conductivity compared to the HDPE sheet (0.45 Wm⁻¹K⁻¹), and more than an order of magnitude higher than EeonTex® (0.13 Wm⁻¹K⁻¹), which is a typical electrically conductive textile material. Further, typical textiles such as cotton have a conductivity on the order of 0.05 Wm⁻¹K⁻¹ ¹²⁹, demonstrating remarkable potential for Dyneema®-based fabrics to be integrated into wearable-device heat spreading applications.

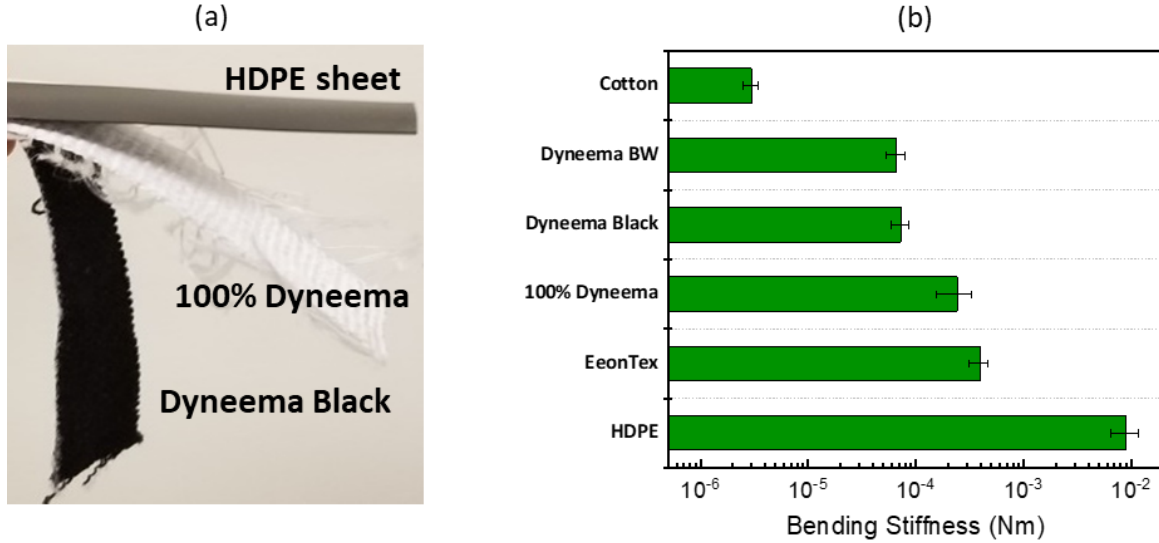


Figure 5.5: (a) Photograph of three different fabrics bending under their own weight. The stiff HDPE sheet does not visibly bend under its own weight, the Dyneema® Black fabric is much more flexible as seen from its extent of bending, and the 100% Dyneema® lies in between. (b) Measured average bending stiffness (flexural rigidity) based on the described bend testing metrology.

5.3.2 Bending Stiffness

The bending stiffness provides a way of quantifying and comparing mechanical compliance and flexibility, which is an important consideration for wearable electronics-based substrates. Using the procedure described above, we quantify bending stiffness by measuring the overhang length at two different bending angles of 41.5° and 7.1° . The choice of these two angles is based on the value of $f(\theta)$, which is ~ 0.5 and 1 at these respective angles and typically in literature^{138,139}. The results of the measurements are reasonably consistent at the two bending angles (See Appendix A). We note two extreme cases of measurement: the HDPE sheet being relatively stiff is tested only at a bend angle of 7.1° as the higher 41.5° bend angle is not achieved solely due to bending under its own weight even at high overhang lengths. In contrast, cotton being highly flexible reaches a high bending angle for a very small overhang length, and so it is measured

only at the bend angle of 41.5° . Figure 5.5a shows a photograph that illustrates the relative flexibility of the HDPE film, 100% Dyneema® fabric, and the Dyneema® Black fabric.

The average value of the bending stiffness measured from the different bend angles is plotted in Figure 5.5a, with higher values indicating lower flexibility. This measure spans over three orders of magnitude with the cotton sample and HDPE sheet representing the extremes. The Dyneema®-based fabrics exhibit an intermediate level of flexibility and are more flexible than EeonTex®.

5.3.3 Crease Testing

An important aspect related to flexibility is the durability of these fabrics (in terms of retaining their excellent thermal conductivity) as they will potentially undergo varying degrees of bending when used in practical applications. To evaluate durability under bending for the commercial Dyneema®-based fabrics, the effect of creasing on the effective thermal properties is explored. Creasing, that is sharp folding of the fabric at a point by 180° , represents an extreme bending case. In these experiments, a swatch of fabric is suspended in a fixture and a nichrome heating wire is attached across the center of fabric. As illustrated in Figure 5.6a, infrared thermal measurements are performed to view the temperature profile in the sample perpendicular to the wire before and after creasing the fabric at a specific location along its length. The creasing is achieved by folding the fabric by $\sim 180^\circ$ about this location while the fabric remains in place within the setup and then bending it back to the original position. The temperature is measured for the initial sample before creasing and after repeating the creasing multiple times (1, 5, 20, and 100 crease cycles). Steady state temperature maps shown in Figure 5.6b, captured before and after multiple crease cycles indicate that the temperature profile along the fabric length is not

significantly affected by creasing. As a point of reference, we perform a separate test to show that the temperature profile is significantly affected in an extreme case when the fabric is scored using a razor blade. We conclude from these observations that wrinkling or creasing the fabric, without damaging the weave structure or the individual yarns, will not significantly impact its effective thermal conductivity.

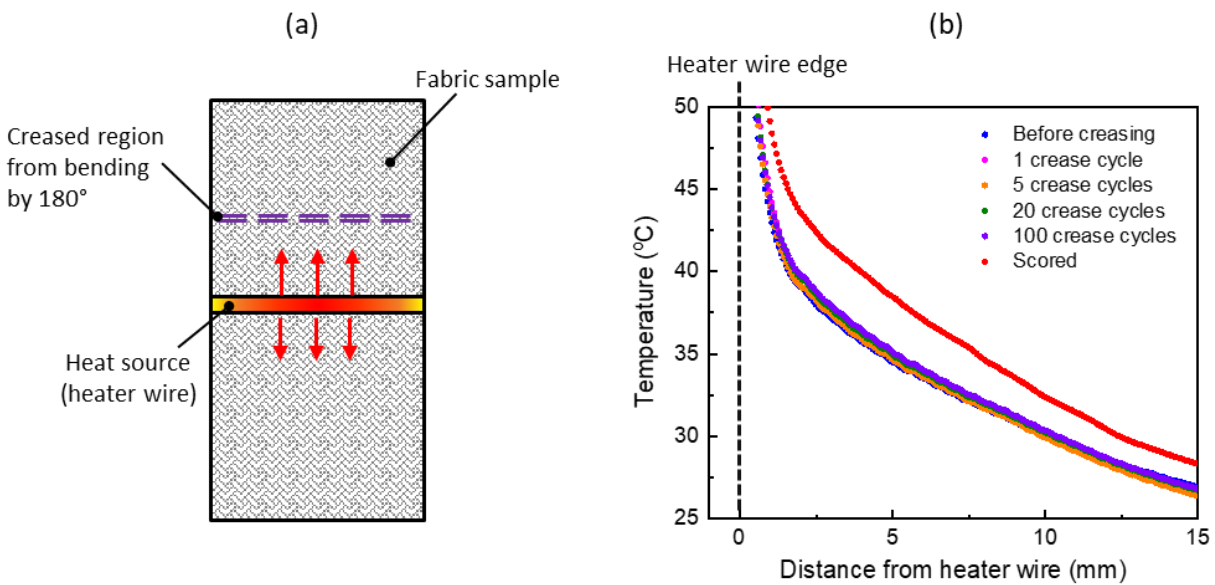


Figure 5.6: (a) Schematic diagram showing the top-view of the testing configuration to assess impact of creasing on thermal performance. The fabric sample is creased by bending by 180° at a specific location as indicated, and infrared temperature maps are captured before and after creasing. (b) Steady state temperature profile as a function of distance from the heater wire on the creased side of the fabric swatch, shown for increasing number of crease cycles and after scoring. The temperature profiles indicate no significant change in heat spreading properties except for the extreme scenario of scoring to purposely damage the individual yarns.

5.3.4 Thermal Annealing

Practical application of Dyneema®-based fabrics in wearable devices must also consider the effect of exposure to high temperatures on the heat spreading performance of the fabrics. Previous studies on UHMW-PE fibers reveal a melting range of 147-152°C^{140,141}. We perform differential scanning calorimetry (DSC) measurements to verify that the melting ranges for as-received Dyneema® SK75 fibers and the Dyneema® Black denim fabric are in the expected range for UHMW-PE materials (see Appendix B). Also, other studies on UHMW-PE indicate respective long-duration and short-duration temperature limits of ~70°C and ~100-130°C¹⁴². These limits are based on evaluation of thermal stability at different aging times based on retention of mechanical properties such as modulus and tenacity. To the best of our knowledge, there has been no evaluation of the thermal stability of these materials as it pertains to the thermal conductivity.

To assess the impact of thermal annealing, we first anneal the Dyneema® Black fabric samples in an oven (Binder ED 023) at different temperatures approaching the melting point (100, 115, 130, 145°C) for 1 hour, and perform DSC measurements after annealing. DSC can give a rough indication of the crystallinity of the sample by evaluation of the melting curves¹⁴³, which directly relates to thermal conductivity, as the high thermal conductivity of UHMW-PE fibers is due to enhanced crystallinity and alignment as a result of the drawing process. Comparison of the DSC results after annealing with those of a control (as-received) fabric sample indicate that the DSC response does not change significantly for the annealing temperatures below 145°C for a 1-hour duration (see Appendix B). Therefore, we use fabric samples annealed at this highest 145°C temperature condition for comparison of the in-plane thermal conductivity with a control fabric sample, using the measurement technique described previously.

The thermal conductivity of a single strip of control fabric is first measured in the in-plane test setup. Then, that same sample is annealed (145°C for 1 hour) and the thermal conductivity is measured again. The thermal conductivity of the fabric sample before and after annealing is measured to be $2.57 \pm 0.1 \text{ Wm}^{-1}\text{K}^{-1}$ and $2.12 \pm 0.1 \text{ Wm}^{-1}\text{K}^{-1}$, respectively. We note that, during this annealing process, the sample is very close to the melting point of Dyneema® and undergoes some curling and deformation, even when the edges of the sample are constrained with tape. This is more pronounced for annealing of a thin strip (it is not observed for larger samples), and leads to fraying and unraveling of some of the yarns from the woven fabric, lowering the effective packing of yarns and thereby the effective thermal conductivity. Therefore, the measured 20% reduction in thermal conductivity can be regarded as an extreme scenario for the potential deleterious effects of annealing.

To eliminate these edge effects due to fraying and unraveling, a thin fabric strip cut out from a larger sample of annealed fabric (145°C for 1 hour) is also considered, and the thermal conductivity of this strip is demonstrated to be similar to that of a control (as received) fabric sample. This is facilitated using a simple experimental method that also enables qualitative visualization of the in-plane heat spreading of the two samples. In this approach, simultaneous transient and steady state IR temperature maps are captured for both samples (as received and annealed) when placed adjacent to each other and heated uniformly at one end. The relative in-plane thermal conductivity of the two samples is quantified based on fin heat conduction analysis (see Appendix C for details). From these different thermal measurements, it can be concluded that exposure of the fabrics to high temperatures does not significantly impact their heat spreading ability for the conditions considered in this study.

5.3.5 Thermal and Mechanical Property Assessment

It is valuable to assess the effective thermal and mechanical properties of the fabrics characterized in this study in the context of a broader set of materials that would be considered for similar applications. The inherent tradeoff between material thermal conductivity and flexibility is illustrated in Figure 5.7, which catalogs these properties a broader set of standard materials that are typically used either for heat spreading or in wearable devices. The flexibility parameter shown here is the inverse of the bending stiffness. For the standard materials shown that are not characterized in this study, the bending stiffness is estimated using plate theory for a fixed thickness of 500 μm .

In general, conventional heat spreaders such as metals sheets and carbon-based materials possess low flexibility due to their high elastic modulus, while conventional polymer and fabric materials offer high flexibility at very low thermal conductivity. The UHMW-PE (Dyneema®) fabrics stand as outliers that break free from this tradeoff in thermal versus mechanical properties. They possess significantly higher thermal conductivity relative to polymers and conventional textiles, while retaining similar levels of mechanical flexibility.

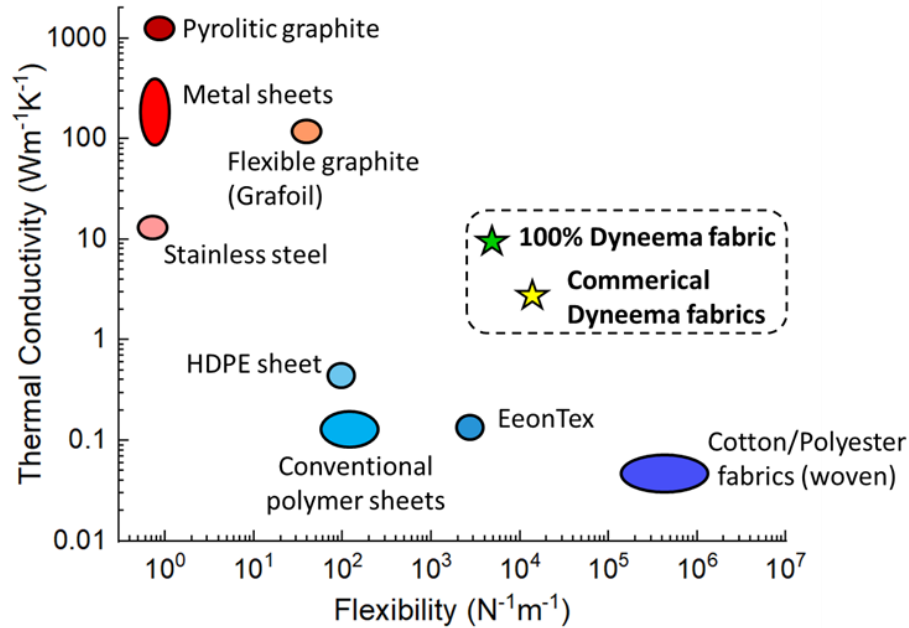


Figure 5.7: Thermal conductivity versus flexibility (inverse of bending stiffness) for different materials. The materials shown in shades of red (top left) are conventional heat spreaders and possess low flexibility, while those shown in shades of blue (bottom center-right) represent conventional polymer and fabric materials with high flexibility and low thermal conductivity.

Dyneema® fabrics (stars) break the trend by demonstrating significantly higher thermal conductivity relative to polymers, while retaining good mechanical flexibility. Data for standard materials (not characterized in this study) taken from references ^{144–148}.

CHAPTER 6. INFRARED-MICROSCOPY ENHANCED CHARACTERIZATION: IN-PLANE LASER-ANGSTROM METHOD

In this chapter, a characterization technique that enables measurement of the in-plane heat spreading properties and anisotropy of a material is presented. This method leverages a laser for transient heating and infrared microscopy for non-contact temperature sensing. The proposed technique builds upon the principles of the IR-based Angstrom method (described in Chapter 3, Section 3.1) that focuses on heat conduction in one-dimension and translates it into a multi-dimensional analysis to develop a novel approach with the ability to characterize in-plane anisotropic thermal properties of materials such as fabrics and films. The principle of this technique, its experimental implementation, and associated numerical models to extract the desired material properties are detailed in the following sections.

6.1 Concept and Experimental Methodology

The proposed method is essentially a radial (two-dimensional) version of the traditional linear Angstrom method and determines the in-plane thermal properties of a material based on extracting its two-dimensional surface temperature map when subjected to periodic heating. In this method, the basic principle of the Angstrom's method which relates the amplitude and phase of the temperature oscillations of a rod-like sample at quasi-steady state to the thermal diffusivity of the sample is leveraged to develop an approach that can be extended to in-plane anisotropic thermal property characterization for samples such as fabrics and films. Essentially, this involves using the transient surface temperature profile of the sample to extract the in-plane thermal conductivity of the sample, while accounting for any orthotropic direction dependence, using an associated heat transfer model. The scope of this method involves enabling measurement of in-plane anisotropic

materials with the anisotropy defined based on different thermal conductivities along the orthotropic directions.

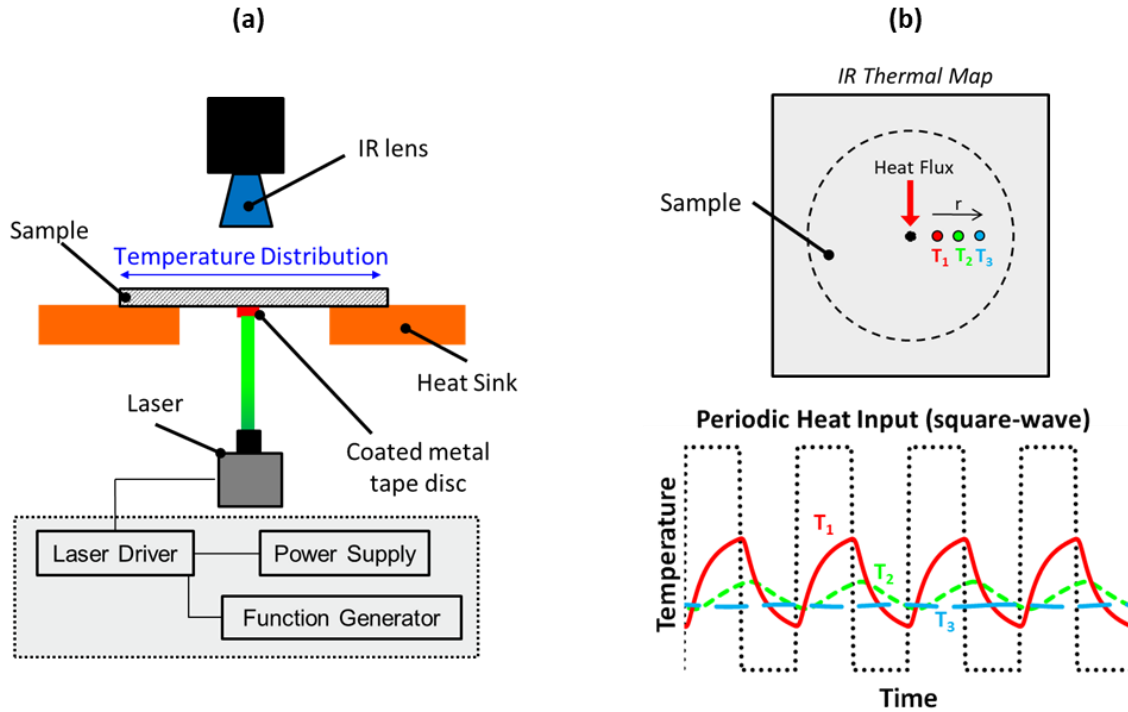


Figure 6.1: (a) Schematic of the experimental setup of the Laser-Angstrom method. A periodic heat input is supplied to the center of the bottom surface of a sample using a laser source and transient temperature movies of the top surface are captured using an IR microscope lens. (b) Illustration of amplitude of temperature oscillations at three different points away from the location of laser heat input. The quasi-steady oscillations exhibit decreasing amplitude and increasing phase lag with distance from the center.

Figure 6.1a shows a schematic of the experimental setup. The sample to be characterized is suspended over a heat sink fixture with a cylindrical hole (~ 30 mm in diameter) at the center that maintains the outer portion of the sample close to room temperature, while allowing the central region of the sample to be heated using a laser beam (445 nm laser wavelength, spot size ~ 1 mm, and maximum power of 2 W). A laser driver connected to a function generator (Hewlett Packard 33120A) provides a modulated square-wave periodic heat input to the bottom surface of the sample, while the transient thermal response of the top surface is captured using an infrared

microscope (QFI Infrascopes). The 1/6th magnification IR lens with a pixel resolution of $\sim 75 \mu\text{m}$ provides a sufficiently large field of view ($\sim 77 \text{ mm} \times 77 \text{ mm}$) to measure the surface temperature response of the sample. A graphite-coated circular metal tape ($\sim 6.3 \text{ mm}$ in diameter) is attached to the bottom surface of the sample to act as an absorber for the laser beam. This serves several practical purposes: (1) to act as an indirect heat source by absorbing the incident laser power to heat up the sample by conduction; (2) to ensure the heating source is approximately circular mitigating the effect of any eccentricity of the beam spot; and (3) to prevent any laser light leaking through porous samples such as fabrics and damaging the infrared detector.. This experimental setup not only allows for non-contact heating and temperature sensing during the radial laser-Angstrom test, but also enables device-like transient performance characterization of materials as the laser power and frequency can be adjusted to assess and compare their heat spreading performance.

During a measurement, the sample is heated at a particular frequency and laser power that are controlled using the frequency generator and by adjusting the potentiometer of the laser driver, respectively. The sample is then allowed to reach quasi-steady state ($\sim 5\text{-}10$ mins). Transient temperature data in the form of infrared temperature movies are then captured at a specific delay time between frames based on the heating frequency to ensure sufficient temporal resolution. Typically, $\sim 5\text{-}10$ cycles of oscillation are recorded to perform the associated modeling and data analysis. As illustrated in Figure 6.1b, temperature oscillations at locations away from the point of laser incidence will exhibit gradually decreasing amplitude and increasing phase lag as a function of distance from the center. The results from processing this experimental data of the top surface of the sample using an associated thermal model yield the in-plane thermal properties of the sample independent of the laser power and the periodic heating frequency.

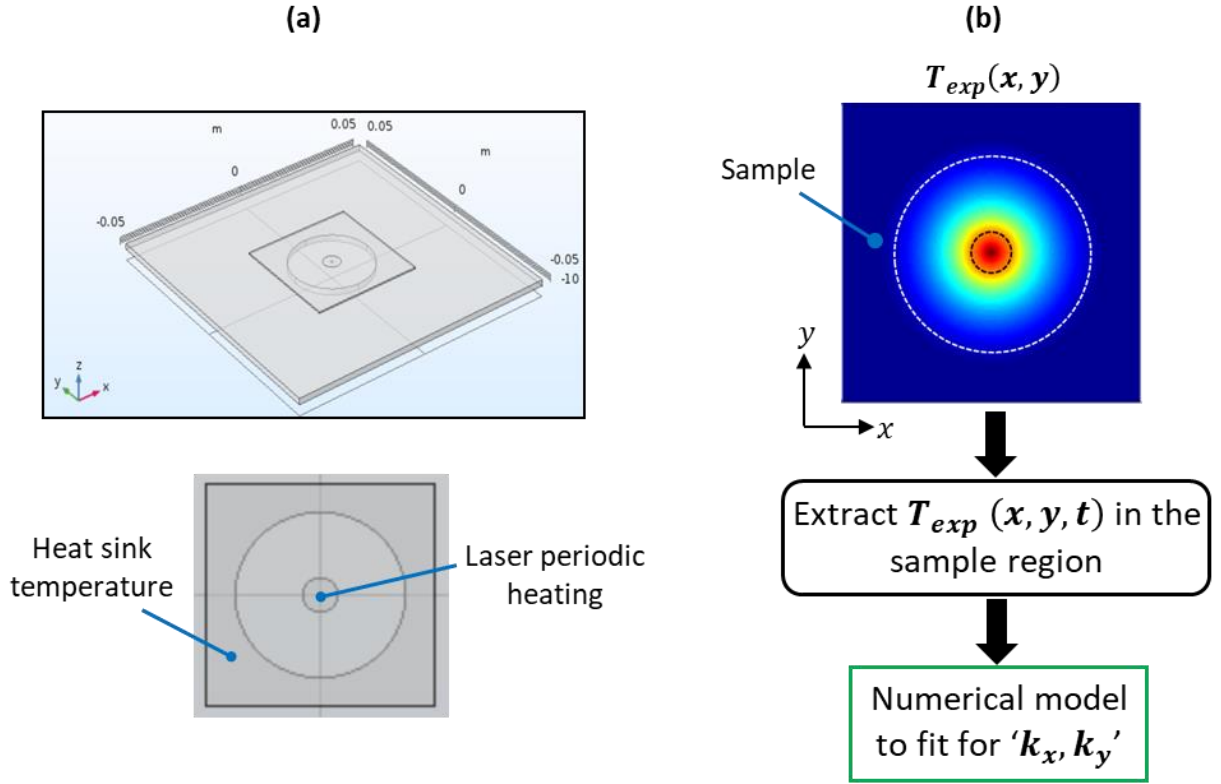


Figure 6.2: Overview of the numerical experiments. (a) Numerical model geometry and boundary conditions simulated in COMSOL Multiphysics. (b) Overall approach illustrating the use of numerical experiments to aid the development of a numerical model for data analysis

6.2 Numerical Experiments

In order to understand the measurement considerations for the proposed experimental methodology and develop an approach for the associated thermal modeling, numerical experiments are performed using COMSOL Multiphysics to simulate the true experimental conditions. A 3D model geometry of the experimental setup including the sample and an aluminum heat sink with a cylindrical hole is created with appropriate boundary conditions as shown in Figure 6.2a. An aluminum disc (~6.3 mm in diameter) is attached to the bottom surface of the sample which acts as the indirect heat source. Note that the absorption properties of this material are not important, as the in-plane thermal properties of the sample are determined from the transient thermal response independent of the input or absorbed laser power. A constant

temperature (293.15 K) boundary condition is assigned to the aluminum heat sink and a periodic heat flux condition of the form $q(t) = q_o''(1 + \sin(2\pi ft))$, where q_o'' is the laser heat flux, f is the periodic heating frequency, and t denoting time, is applied to the central ~1 mm diameter region of the aluminum disc to simulate the periodic heating of laser spot. The material properties of the sample including its density (ρ), specific heat (C_p), and thermal conductivity along different primary (orthotropic) (k_x , k_y , and k_z) are specified as inputs to the model. Here k_x and k_y represent the thermal conductivities along the x and y in-plane orthotropic directions, while k_z represents the through-plane thermal conductivity which is along the z direction. The output of the simulated experiments is the temperature data of the top surface of the sample at specified regular grid of points (200×200 grid) as a function time. As illustrated in Figure 6.2b, the numerical experiments provide a framework to develop a numerical approach with the objective of extracting the in-plane thermal conductivities of the sample, k_x and k_y , by knowing only the simulated transient surface temperature map $T_{exp}(x, y, t)$, similar to what would be measured in a real experiment. Therefore, this framework provides a validated numerical modeling approach to determine the orthotropic in-plane thermal conductivities of a material (independent of its through-plane conductivity) using the proposed measurement technique. The details of this numerical methodology and the technical considerations under which it is valid are discussed in the following sections.

6.3 Numerical Analysis and Property Extraction

In this section, a numerical analysis methodology is presented to allow extraction of thermal property data of a sample. This involves consideration of appropriate governing equations and boundary conditions to model the transient temperature profile of the sample and fit for the in-

plane thermal properties without prior knowledge of the laser power input and through-plane thermal conductivity.

6.3.1 Generalized Numerical Approach

The transient temperature profile, $T(x, y, t)$ of the top surface of the sample in the suspended region outside of the central metal disc (in the region between the black and white dashed concentric circles shown in Figure 6.2b) is modeled based on the governing equation for two-dimensional transient heat conduction:

$$\frac{\partial}{\partial x} \left(k_x \frac{\partial T}{\partial x} \right) + \frac{\partial}{\partial y} \left(k_y \frac{\partial T}{\partial y} \right) = \rho C_p \frac{\partial T}{\partial t}. \quad (6.1)$$

Due to the periodic heating of the laser, a time-periodic solution in temperature can be assumed for the sample. This can be written in complex form in the frequency domain as:

$$T(x, y, t) = [P(x, y) + iQ(x, y)] e^{i\omega t}, \quad (6.2)$$

where $P(x, y)$ and $Q(x, y)$ represent the real and imaginary parts of the complex amplitude, and the $e^{i\omega t}$ accounts for the periodic behavior of the solution with $\omega = 2\pi f$ representing the angular frequency of the periodic heat input. Substituting this general solution for temperature into eq. (6.1), and equating the real and imaginary coefficients, we obtain the following set of partial differential equations for P and Q :

$$k_x \frac{\partial^2 P}{\partial x^2} + k_y \frac{\partial^2 P}{\partial y^2} = -\rho C_p \omega Q, \quad (6.3)$$

$$k_x \frac{\partial^2 Q}{\partial x^2} + k_y \frac{\partial^2 Q}{\partial y^2} = \rho C_p \omega P. \quad (6.4)$$

The above equations are valid at each point in the domain and can be solved as simultaneous algebraic equations based on discretization of the second order derivatives for P and Q to obtain a

map of (k_x, k_y) at each point. Alternatively, these can also be solved as a system of discretized equations across all the grid points in the domain (say n points) as shown below:

$$\begin{bmatrix} \frac{\partial^2 P_1}{\partial x^2} & \frac{\partial^2 P_1}{\partial y^2} \\ \ddots & \ddots \\ \frac{\partial^2 Q_1}{\partial x^2} & \frac{\partial^2 Q_1}{\partial y^2} \\ \ddots & \ddots \end{bmatrix}_{2n \times 2} \begin{bmatrix} k_x \\ k_y \end{bmatrix} = \rho C_p \omega \begin{bmatrix} -Q_1 \\ \ddots \\ P_1 \\ \ddots \end{bmatrix}_{2n \times 1} \quad (6.5)$$

The simulated quasi-steady temperature response of the sample $T_{exp}(x, y, t)$ is processed using a Fourier transform at each point in the domain at the fundamental frequency (frequency of periodic laser heating) to obtain the in-phase and out-of-phase components which correspond to the spatially varying real (P) and imaginary (Q) parts of the temperature amplitude signal at each grid point. Using numerical gradient computations of the P and Q matrices, the second order derivative estimators P_{xx} , P_{yy} , Q_{xx} , and Q_{yy} can be obtained. These can be processed at all chosen points in the domain to solve for k_x and k_y using eq. (6.5). This is solved using MATLAB's optimization solver which outputs the values of k_x and k_y that minimizes the objective function given by $\|[\mathbf{PQ}] \cdot [\mathbf{k}] - [\mathbf{pq}]\|$, where $[\mathbf{PQ}]$ represents the coefficient matrix on the left hand side of eq. (6.5), $[\mathbf{k}]$ represents the orthotropic thermal conductivity matrix $\begin{bmatrix} k_x \\ k_y \end{bmatrix}$, $[\mathbf{pq}]$ represents the matrix on the right hand side of eq. (6.5), and '||' denotes the Euclidean norm. This numerical solution approach is similar to the approach presented in Christov *et al*¹⁴⁹. Confidence intervals (95%) for the best-fit thermal conductivity values can also be obtained using the associated *nlparci* function in MATLAB. The difference between the fitted thermal conductivity results determined using this numerical approach starting from the simulated transient thermal response of the sample, and the

true input values of k_x and k_y provides a method of estimating the total error associated with the proposed measurement technique.

The numerical approach described above is valid assuming the temperature gradients along the through-thickness direction of the sample away from the heat source are negligible compared to the gradients in the in-plane direction of the sample. An advantage of this approach is that the boundary conditions do not need to be specifically accounted for in the model provided the region of analysis does not closely approach the boundaries. Therefore, the points chosen to fit for the in-plane thermal conductivities should be sufficiently far away from the inner and outer boundary conditions. The validity of these assumptions relates to various parametric considerations relating to the sample and the measurement setup which will be discussed in Section 6.3.

6.3.2 Reduced Analytical Model for Isotropic Case

The general case of an anisotropic material has no simple analytical solution, and the analysis technique described in section 6.2.2 must be used. But if the thermal conductivity is isotropic in-plane, then, an analytical solution in radial coordinates can be used for fitting for thermal conductivity. In this case, due to uniform heat spreading across all radial directions of the sample when subjected to periodic heating at a centrally located circular spot, circular isotherms will be observed at quasi-steady state with decreasing amplitude and increasing phase of the temperature response as a function of radial distance from the center. Therefore, the model of the linear-Angstrom method described by Hahn *et al.*⁸⁷ can be extended to a radial coordinate system to determine the in-plane thermal diffusivity (and therefore thermal conductivity) of the sample using an analytical approach.

The one-dimensional transient heat conduction equation in radial coordinates is given below:

$$\frac{\partial^2 T}{\partial r^2} + \frac{1}{r} \frac{\partial T}{\partial r} = \frac{1}{\alpha} \frac{\partial T}{\partial t}. \quad (6.6)$$

Considering temperature oscillation boundary conditions in complex form with fixed amplitudes T_a and T_b at two radial locations $r = a$ and $r = b$ corresponding to the inner and outer boundaries of the sample domain, and a phase lag ϕ_b between them as shown below:

$$T(r = a, t) = \frac{T_a}{2} e^{i\omega t} + \frac{T_a}{2} e^{-i\omega t}; \quad T(r = b, t) = \frac{T_b}{2} e^{i(\omega t - \phi_b)} + \frac{T_b}{2} e^{-i(\omega t + \phi_b)}, \quad (6.7)$$

a general periodic solution for the temperature profile in frequency domain can be written as

$$T(r, t) = T_1(r) e^{i\omega t} + T_2(r) e^{-i\omega t}. \quad (6.8)$$

Here $T_1(r)$ and $T_2(r)$ represent general complex functions which can be solved by substituting back into the governing equation and are in the form of Bessel's functions J_0 and Y_0 of the periodic heating frequency ω and the sample in-plane thermal diffusivity α (See Appendix D for details). Therefore, an analytical solution for the temperature profile can be obtained if the parameters T_a , T_b , and ϕ_b are known. These parameters can be determined based on experimental data for a given sample of interest to obtain an analytical solution of the quasi-steady state temperature profile as a function of radial position. By comparing the analytical solution to the experimental temperature profile at a given periodic heating frequency based on the quasi-steady amplitude $A(r)$ and phase $\phi(r)$ of the temperature oscillations, we can fit for the in-plane thermal diffusivity α and therefore determine the in-plane thermal conductivity (k) of the sample. In this approach, a fitting function that combines $A(r)$ and $\phi(r)$ of the form $f\{(r - r_0)^2\} = \ln [A_0/A(r)][\phi_0 - \phi(r)]$ similar to that used by Hahn *et al.*⁸⁷ based on the experimental and analytical model data can yield the thermal diffusivity of the sample.

6.4 Results and Discussion

In this section, the results of the proposed measurement method and numerical approach are presented by analyzing representative numerical experiments for different sample and measurement parameter inputs. The validity of the numerical approach and the associated technical considerations for experimental measurements are discussed using representative cases in the following subsections.

6.4.1 Representative Analysis for Validation of the Method

An example of an in-plane anisotropic sample, 500 μm thick, with thermal conductivities $k_x = 2 \text{ Wm}^{-1}\text{K}^{-1}$, $k_y = 6 \text{ Wm}^{-1}\text{K}^{-1}$, and $k_z = 0.5 \text{ Wm}^{-1}\text{K}^{-1}$, density (ρ) of 970 kg m^{-3} , and specific heat capacity of $1950 \text{ J kg}^{-1}\text{K}^{-1}$ is considered. Numerical simulations are performed as described in Section 6.2.1. An input heat flux of $q_o'' = 5 \times 10^5 \text{ Wm}^{-2}$ and a frequency of $f = 25 \text{ mHz}$ are used as input parameters to specify the periodic heat input boundary condition, and a total of 25 periods of oscillation with 100 time steps in each period are simulated. The temperature response of the top surface of the sample extracted on a 200×200 grid with a pixel spacing of $200 \mu\text{m}$ is shown in Figure 6.3a with the elliptical isotherms indicating the in-plane anisotropy of the sample. The two depicted inner and outer dashed circles represent the boundaries of the domain corresponding to the edge of the metal disc absorber and the edge of the heat sink platform respectively. The temperature as a function of time at two points (1 and 2) halfway between the inner and outer boundaries along the in-plane orthotropic directions of the sample is plotted in Figure 6.3b. The periodic temperature response at quasi-steady state is observed due to the periodic nature of the laser heat input. Also, the temperature profile at point 2 displays a higher mean temperature and amplitude of oscillations due to the three-times higher in-plane thermal conductivity along the y direction. The transient temperature information of the top surface of the

sample is used to extract the spatially varying real and imaginary parts of the complex temperature amplitude, P and Q at each point on the grid as described in Section 6.2.2. These are then used to simultaneously solve the discretized form of eq. (6.3) and eq. (6.4) to obtain a map of thermal conductivities, k_x and k_y at each grid point which are plotted in Figure 6.3c and Figure 6.3d respectively. Since the central region of the laser spot (~ 0.5 mm radius) is subjected to a periodic heat flux boundary condition and the assumed solution for the temperature profile is periodic in temperature, grid points close to the outer perimeter of the laser spot (generally within a radial distance 6-7 times the laser spot radius) should not be included. In this case, these are automatically excluded as such points lie within the region of the metal tape disc. Also, there is intrinsic noise present in the numerical gradient approximation used for discretization which is relatively significant near boundaries where the geometry and mesh change. Therefore, grid points close to the inner and outer dashed circles are also not included as illustrated in Figure 6.3c and Figure 6.3d. For the calculated maps of k_x and k_y shown, the average extracted values across all grid points are $2.01 \text{ Wm}^{-1}\text{K}^{-1}$ and $6.13 \text{ Wm}^{-1}\text{K}^{-1}$ respectively. However, the calculated standard deviations are very high ($>100\%$ in each case) due to the nature of the point-by-point computation. At many individual points, the extracted k_x and k_y have extremely high errors as also apparent from the contour plots in Figure 6.3c and Figure 6.3d. These contour maps are useful to graphically illustrate the computed values of thermal conductivity at each point in the domain, but ultimately, we consider a single fit of k_x and k_y based on the numerical solution approach presented in eq. (6.5). Considering all the points in the domain to solve the system of equations to extract a single value for both k_x and k_y , the inaccuracies are almost entirely resolved. The extracted values based on eq. (6.5) are $1.98 \text{ Wm}^{-1}\text{K}^{-1}$ for k_x and $6.22 \text{ Wm}^{-1}\text{K}^{-1}$ for k_y , with 95% confidence intervals of (1.975, 1.987) and (6.208, 6.234) respectively. Therefore, in-plane orthotropic thermal

conductivities of the sample are determined to within 4% error for both directions using the proposed measurement approach.

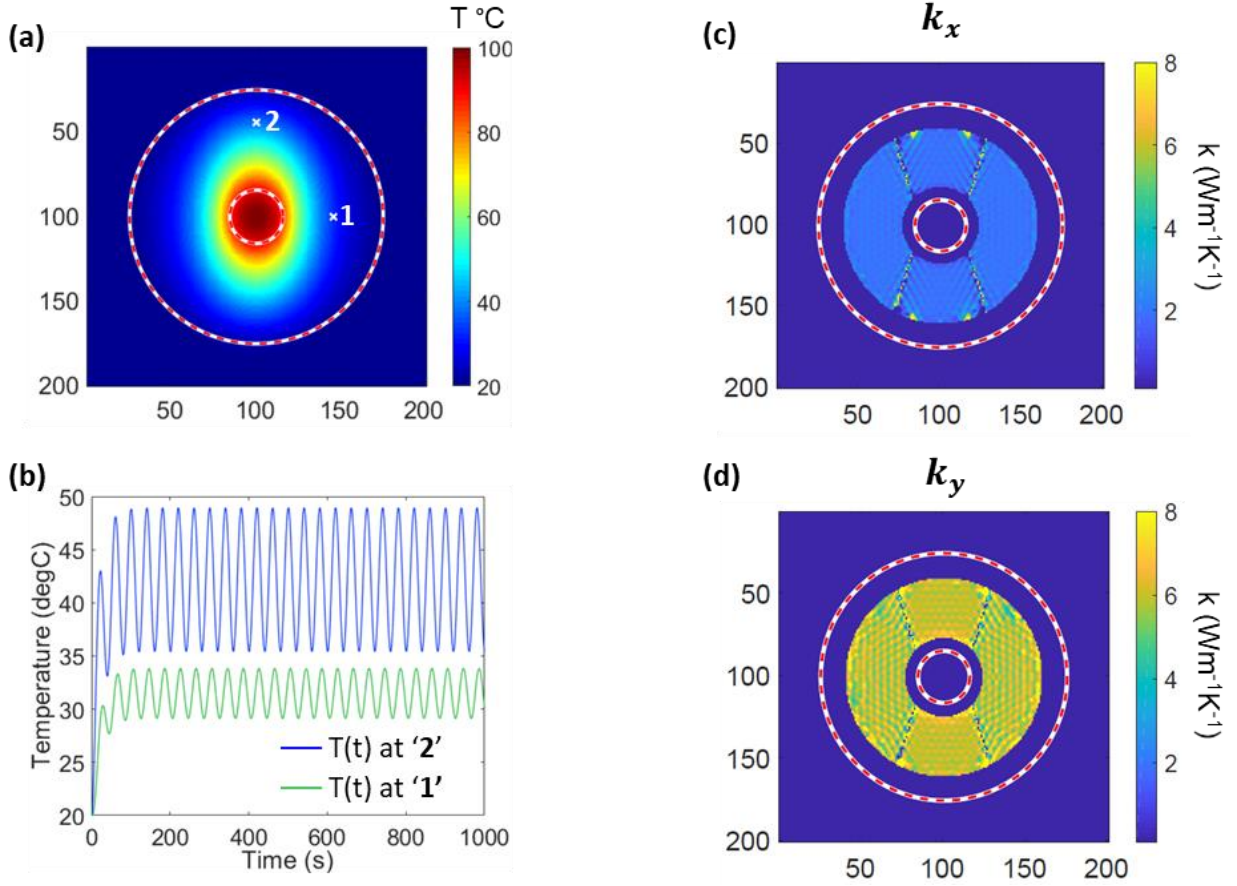


Figure 6.3: Representative analysis of numerical simulations for an in-plane anisotropic sample with $k_x = 2 \text{ Wm}^{-1}\text{K}^{-1}$ and $k_y = 6 \text{ Wm}^{-1}\text{K}^{-1}$ depicting the (a) simulated top surface temperature map at a given time instant at quasi-steady state with the evolution of temperature with time for two specific points plotted in (b). The extracted contour maps of k_x and k_y obtained individually at each point are plotted (c) and (d) respectively. The red-dashed circles indicate the inner and outer boundaries representing the edge of the metal tape disc and the edge of the heat sink.

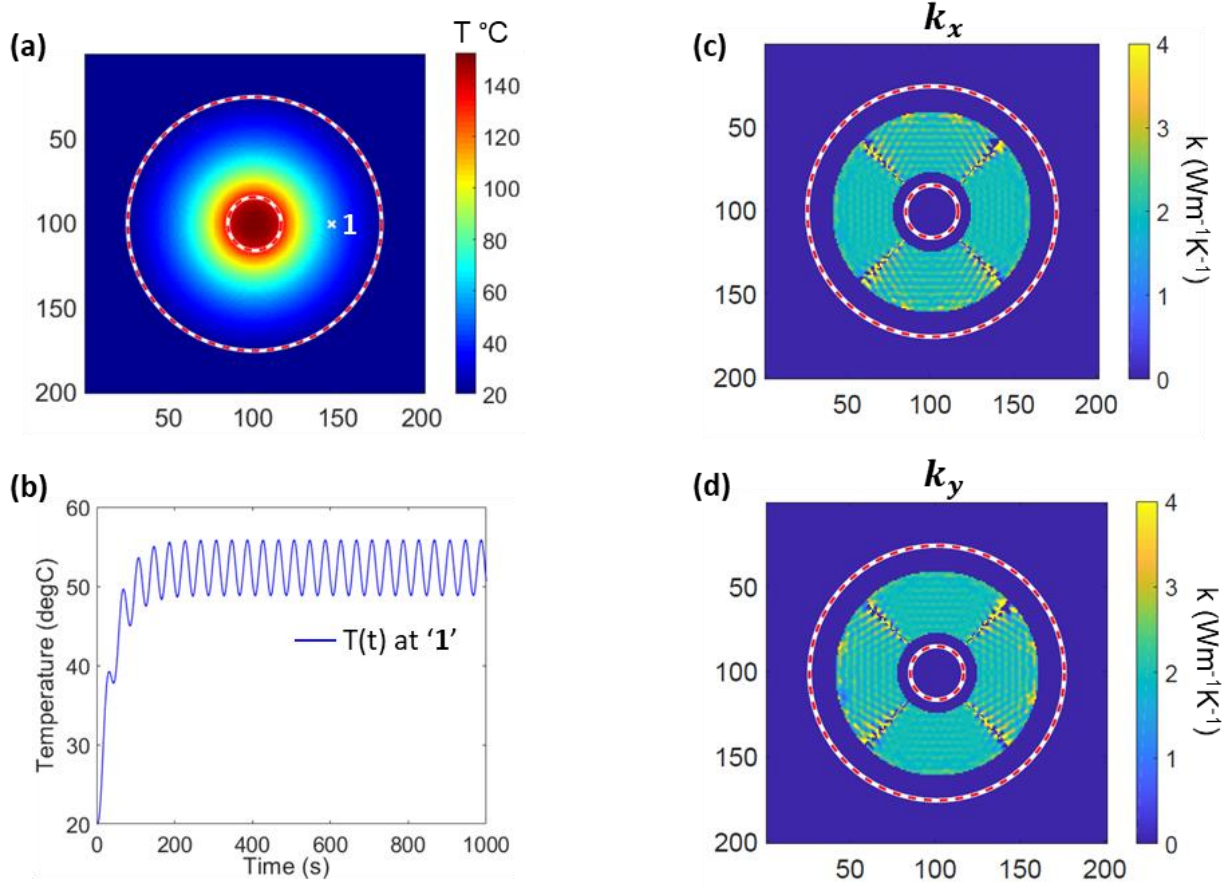


Figure 6.4: Representative analysis of numerical simulations for an in-plane isotropic sample with $k_x = 2 \text{ Wm}^{-1}\text{K}^{-1}$ and $k_y = 2 \text{ Wm}^{-1}\text{K}^{-1}$ depicting the (a) simulated top surface temperature map at a given time instant at quasi-steady state with the evolution of temperature with time at the indicated point plotted in (b). The extracted contour maps of k_x and k_y obtained individually at each point are plotted (c) and (d) respectively. The red-dashed circles indicate the inner and outer boundaries representing the edge of the metal tape disc and the edge of the heat sink

As a second representative example, a sample with equal input in-plane orthotropic thermal conductivities of $2 \text{ Wm}^{-1}\text{K}^{-1}$ and all other input parameters of the first case is considered. In this case, the surface temperature map, the transient response, and the calculated maps of k_x and k_y are shown in Figure 6.4. The in-plane isotropic nature of the sample is evident from the circular isotherms seen in Figure 6.4a. The extracted values of k_x and k_y in this case based on solving the system of equations eq. (6.5) are 1.997 and $1.995 \text{ Wm}^{-1}\text{K}^{-1}$ with confidence intervals of $(1.9936, 1.9997)$ and $(1.9922, 1.9982)$ respectively. This is in excellent agreement with the input thermal conductivity values. This case is primarily used as a validation of the proposed numerical approach by comparing with the analytical approach for the in-plane isotropic case described in Section 6.2.3. The same transient temperature data is processed using the described analytical solution approach by obtaining the amplitude and phase lag of the temperature oscillations as a function of radial distance from the outer radius of the metal tape disc to the edge of the heat sink platform. This is done by dividing this suspended region of the sample into 50 radial segments and averaging the temperature data within these segments over 360° . This spatially averaged temperature amplitude and phase lag data is plotted in Figure 6.5a. As expected, the amplitude of the oscillations continuously decreases with increasing radial distance and the magnitude of the phase lag with respect to the center of the sample where the heat input is applied continuously increases. By fitting the combined amplitude and phase parameter f (as described in Section 6.2.3) in the region indicated by the red-dashed lines in Figure 6.5a, the thermal diffusivity of the sample is obtained. Note that the jump in the phase corresponds to a phase change of 2π , and the fitted result is not significantly dependent on the chosen fitting region in this case provided the starting point is sufficiently away from the inner boundary for the one-dimensional radial heat transfer assumption to hold good. The data from the numerical experiment, fitted result, and 10%

sensitivity bounds for the fitted solution is plotted in Figure 6.5b. The fitted thermal diffusivity of $\alpha = 1.055 \times 10^{-6} \text{ m}^2\text{s}^{-1}$ corresponds to a thermal conductivity of $1.995 \text{ Wm}^{-1}\text{K}^{-1}$ which agrees well with the input value of $2 \text{ Wm}^{-1}\text{K}^{-1}$ with good sensitivity of the fit.

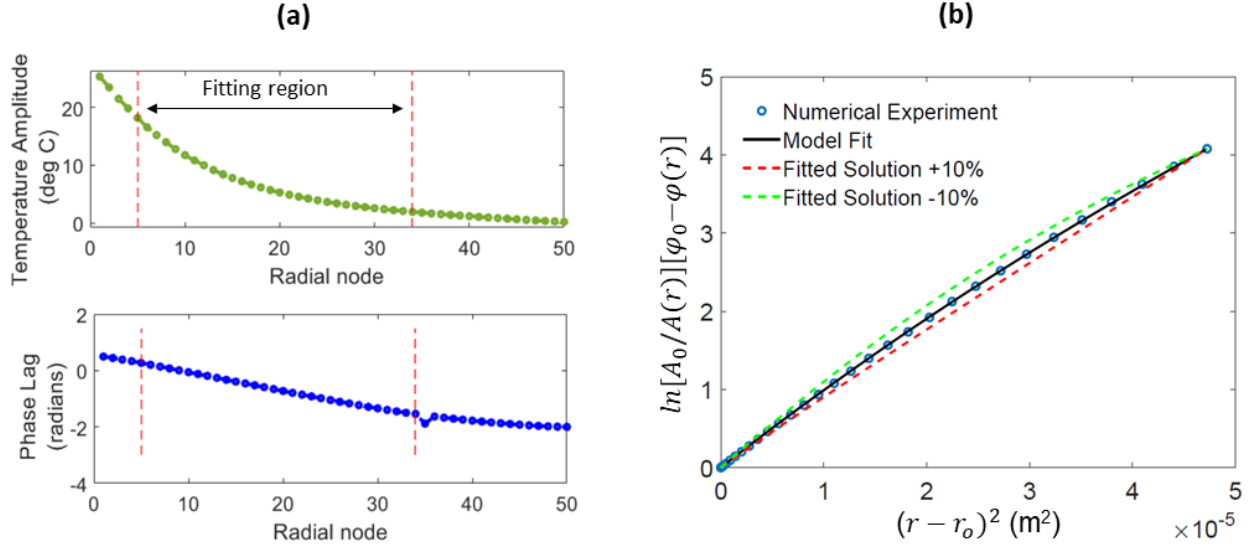


Figure 6.5: (a) The temperature amplitude and phase lag as a function of radial distance from the edge of the metal tape disc averaged over 360° for the case of the in-plane isotropic sample with $k_x = 2 \text{ Wm}^{-1}\text{K}^{-1}$ and $k_y = 2 \text{ Wm}^{-1}\text{K}^{-1}$. The data from the indicated fitting region is used to fit for the thermal conductivity of the sample as shown in (b) along with 10% sensitivity bounds. A fitted conductivity of $1.995 \text{ Wm}^{-1}\text{K}^{-1}$ is obtained which agrees well with the input value of $2 \text{ Wm}^{-1}\text{K}^{-1}$

6.4.2 Measurement Considerations

The measurement approach and representative cases presented above demonstrate the applicability and validity of the proposed method to characterize the in-plane anisotropic thermal properties of a sample based on the known/measured transient temperature distribution of the top surface when subjected to periodic heating. The thermal conductivities in the in-plane direction are extracted independent of the laser heat input, periodic heating frequency, and the through-plane sample properties and temperature gradients. Here, the main assumption is that the heat transfer is predominantly two-dimensional in the plane of the sample and that the through-plane temperature gradients in the third dimension across the sample thickness are not significant. This assumption is generally valid when the region of analysis does not include locations close to the laser heat input. However, it is important to consider the validity of this assumption depending on the properties of sample to be characterized and the associated limits of this measurement method. Specifically, this consideration relates to the relative in-plane and through-plane thermal properties and the thickness of the sample, which influence the periodic heating frequency and the dimensions of the experimental setup to be chosen for a particular measurement. By tuning these controllable measurement parameters appropriately, the accuracy of the measurement can be reasonably maintained over a wide range of thermal properties and length scales.

An important measurement consideration is the relative through-plane versus in-plane thermal conductivity of the sample which also directly relates to the sample thickness (t). To minimize the error induced by through-plane temperature gradients of the sample which are assumed to be negligible compared to the in-plane gradients, a sufficiently low frequency should be used such that the sample thickness is much lower than the thermal penetration depth. This condition can be given as:

$$f \ll \frac{\alpha_z}{\pi t^2} \quad (6.9)$$

where $\alpha_z = \frac{k_z}{\rho C_p}$. Therefore, for a given through-plane conductivity and sample thickness, the input frequency for accurate measurements should be much smaller (factor of ~ 0.1) compared to this upper bound. At the same time, with respect to the in-plane direction, the frequency of heating cannot be too low and should be sufficiently high to minimize the effect of the boundaries based on the dimensions of the setup. More specifically, the temperature oscillations on the plane of the sample should be sufficiently attenuated close to the boundaries to satisfy the semi-infinite criteria. This condition can be given as ⁸⁷ :

$$f > \frac{2.98 \alpha_{x,y}}{\pi R^2} \quad (6.10)$$

where $\alpha_{x,y} = \frac{k_{x,y}}{\rho C_p}$, and R , the outer radius of the heat sink platform, is chosen as a characteristic sample length along the radial direction in this case. Depending on the specific sample parameters involved, the measurement frequency can be on the same order of this ideal lower bound, but values significantly lower than this limit will lead to inaccuracies in the predicted results.

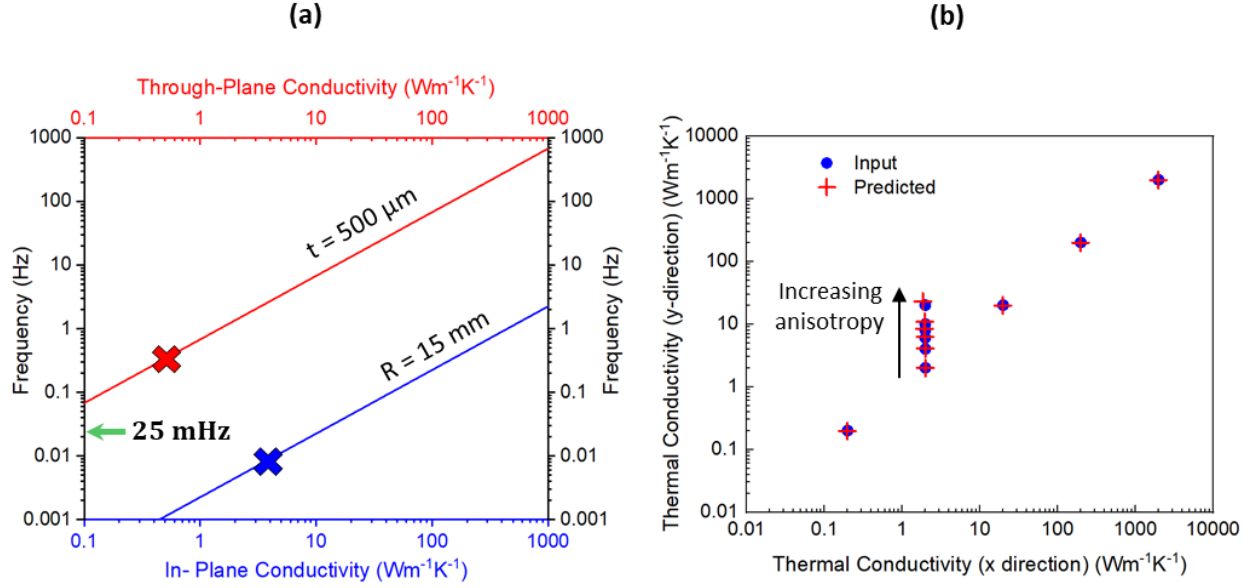


Figure 6.6: (a) Illustration of periodic heating frequency bounds depending on the in-plane and through-plane thermal conductivity of a sample at a fixed value of thickness and outer radius of the experimental setup. An example case corresponding to $k_{x,y} = 4 \text{ Wm}^{-1}\text{K}^{-1}$ and $k_z = 0.5 \text{ Wm}^{-1}\text{K}^{-1}$ is depicted as indicated by the pair of 'X' points. A typical frequency choice (25 mHz) for measurement in this case is indicated. (b) Input and predicted thermal conductivities along the x and y orthotropic directions demonstrating the applicability of the proposed measurement method across a wide range of thermal conductivity values.

The conditions described above are graphically illustrated in Figure 6.6a for a specific case corresponding to $k_{x,y} = 4 \text{ Wm}^{-1}\text{K}^{-1}$, $k_z = 0.5 \text{ Wm}^{-1}\text{K}^{-1}$, $t = 500 \mu\text{m}$, and $R = 15 \text{ mm}$. The upper bound is dictated by the values of k_z and t , and the lower bound by the values of $k_{x,y}$ and R . In this way, for a given set of sample parameters and estimated thermal properties, and a specific experimental setup, the frequency of the periodic heat input can be chosen to lie in the region between these two limits, as indicated by the example choice of 25 mHz. This plot serves as a general guideline to assist choice of measurement parameters during an experiment and understand the limits of the measurement. For example, we can see from the figure that measurements of a sample with high in-plane conductivity ($>100 \text{ Wm}^{-1}\text{K}^{-1}$) and low through-plane conductivity (<0.1

$\text{Wm}^{-1}\text{K}^{-1}$) would not be feasible for this case of sample thickness and outer radius of the setup, and a scaled-up version of the experimental setup (higher R) would be needed. It is important to note that this plot does not consider the in-plane anisotropy of the sample, which is a separate and important measurement consideration. More detailed analysis is needed to thoroughly understand the parametric space associated with these measurements and develop this approach as a standard characterization technique.

To demonstrate the tunability of the measurement approach based on the properties of the sample, different numerical experiments are considered with the in-plane orthotropic thermal conductivity of the sample spanning 5 orders of magnitude. In each case, the through-plane thermal conductivity is set to be on the order of 0.1 times the in-plane thermal conductivity as a representative factor of in-plane to through-plane anisotropy. Fixed input values of sample thickness, density, and heat capacity, and fixture dimensions are assumed. Figure 6.6b shows a chart of thermal conductivity along the orthotropic directions plotted against each other to compare the inputs and the predictions from the numerical approach across a range of conductivities. For each pair of data points plotted, the input laser power and heating frequency are adjusted to accurately capture the in-plane thermal conductivities along both directions. As an example, a heating power of $5 \times 10^5 \text{ Wm}^{-2}$ and a frequency of $f = 25 \text{ mHz}$ are used for the case of $k_x, k_y = 2 \text{ Wm}^{-1}\text{K}^{-1}$, while a heating power of $1 \times 10^8 \text{ Wm}^{-2}$ a frequency of $f = 10 \text{ Hz}$ are used for the case of $k_x, k_y = 2000 \text{ Wm}^{-1} \text{ K}^{-1}$. The agreement between the input and predicted values is within 1% for equal values of k_x and k_y across the broad range of thermal conductivity considered with other sample properties being constant. Also, an in-plane anisotropic ratio of up to 10 is accurately predicted to within an average error <10% across the entire range, with representative cases shown in Figure 6.6a for a thermal conductivity on the order of 1-10 $\text{Wm}^{-1} \text{ K}^{-1}$. Note that the error for

anisotropic ratios in the range of 1-8 is within 5% with error increasing to >10% for an anisotropic ratio of 10. This increase in error with increasing anisotropy is mainly related to increased relative differences in temperature oscillations and phase lag along the primary in-plane directions which is captured with lesser accuracy for a given value of heating frequency. Conducting multiple sets of experiments with different chosen frequencies can potentially be used to significantly reduce this error for highly anisotropic (in-plane) samples. However, an anisotropic ratio of 10 considered here as an upper bound is a conservative estimate as high anisotropic ratios in the in-plane direction are atypical for materials in general.

6.4.3 Experimental Demonstration

Here, an experimental demonstration of the proposed measurement method is presented. Thermal measurements are performed using the experimental setup and procedures described in Section 6.1. Two different samples are considered: an isotropic high-density polyethylene (HDPE) sheet and a Dyneema Black composite fabric with different sets yarns along its warp and weft directions as described in Chapter 5. These materials are experimentally characterized at periodic heating frequencies of 25 mHz and 100 mHz respectively using different power levels for the two samples. Transient temperature movies are captured using infrared microscopy at quasi-steady state to obtain ~5 periods of temperature oscillations, and representative IR temperature maps at a particular time instant are shown in Figure 6.7.

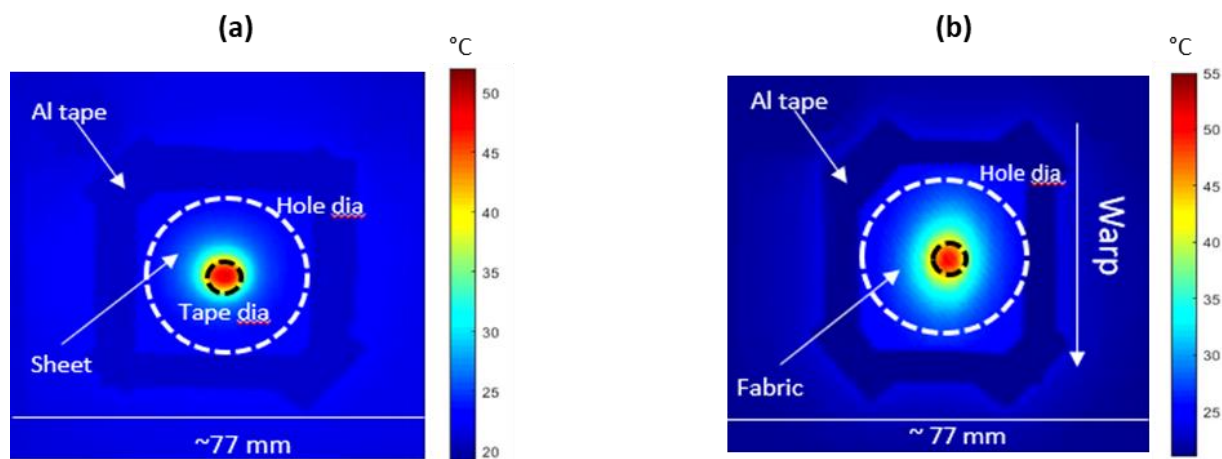


Figure 6.7: Representative IR temperature maps at quasi-steady state for (a) HDPE sheet, and (b) Dyneema Black fabric under periodic heating frequencies of 25 mHz and 100 mHz respectively using a laser heat source. The circular isotherms in the case of the isotropic HDPE sheet and the elliptical isotherms in the case of the Dyneema fabric demonstrate that the intrinsic in-plane anisotropy of the sample can be captured experimentally.

As seen in Figure 6.7a, circular isotherms are obtained for the HDPE sheet due to the in-plane isotropic nature of the sample, while Figure 6.7b shows elliptical isotherms for the Dyneema Black fabric due to the intrinsic in-plane anisotropy of the sample resulting from the different types of yarns present along the two orthotropic directions. Therefore, the in-plane anisotropy of a material can be visually captured during experiments using this measurement method. Another important aspect of these measurements is that the relative in-plane heat spreading properties of different materials can be qualitatively compared based on the surface temperature maps. To obtain the same order of average temperature rise of the samples for the two cases shown here, a significantly higher frequency and laser power were used for the Dyneema fabric compared to the HDPE sheet. This indicates that the Dyneema fabric has a significantly higher in-plane thermal conductivity compared to the HDPE sheet which was also evident from the results presented in Chapter CHAPTER 5.

This experimental data for both samples is processed using the numerical analysis approach. Due to presence of noise in the temperature oscillations of the actual experimental data when compared to the COMSOL numerical experiments, the calculation of the second order derivative estimators P_{xx} , P_{yy} , Q_{xx} , and Q_{yy} described in Section 6.3.1 requires applying filtering methods using MATLAB's image averaging filter function to obtain smooth gradient maps for accurate computations. After appropriate filtering of the raw data, the 95% confidence intervals for extracted thermal conductivities, k_x and k_y , for the HDPE sample are (0.508, 0.522) $\text{Wm}^{-1}\text{K}^{-1}$ and (0.539, 0.553) respectively, assuming typical values of density and specific heat for HDPE. This is in very good agreement with the theoretical conductivity of HDPE, as also measured using the steady state heater wire method in Section 0, and also indicates an anisotropy ratio of ~ 1 which is expected for this material. For the Dyneema fabric, effective diffusivity parameters, $\left(\frac{k}{\rho C}\right)_x$ and $\left(\frac{k}{\rho C}\right)_y$, are determined along each orthotropic direction in lieu of the thermal conductivities, as the directional effective density and specific heat of the fabric are not well defined or quantifiable due to the presence of different types of yarns in each direction. The extracted effective diffusivity parameters are $(k/\rho C_p)_x = (0.60 \times 10^{-6}, 0.66 \times 10^{-6}) \text{ m}^2 \text{ s}^{-1}$ and $(k/\rho C_p)_y = (0.06 \times 10^{-6}, 0.095 \times 10^{-6}) \text{ m}^2 \text{ s}^{-1}$, indicating an in-plane spreading anisotropy ratio of ~ 8.3 .

In order to further improve and validate this method, additional experimentation and modeling analysis are needed. Specifically, experiments need to be performed by adjusting the periodic heating frequency and laser power to obtain higher amplitude of temperature oscillations away from the edge of the metal tape disc to reduce the noise in the raw temperature data. The uncertainty in the measurements can be reduced by performing multiple experiments at different input frequencies and power levels for the same sample. Also, the numerical modeling approach can be

extended to include the effect of natural convection by including a convection coefficient as a fitting parameter in the governing equations. Finally, the measurement technique can be further validated by performing experiments with a standardized reference sample with known thermal conductivities in the in-plane orthotropic directions.

CHAPTER 7. CONCLUSION

7.1 Summary⁵

In this thesis, the effective thermal properties of a high thermal conductivity polymer material (UHMW-PE) have been investigated. The material studied is a commercial gel-spun fiber manufactured using techniques that impart a high degree of crystallinity and orientation to the polymer molecular chains, resulting in a high strength and high thermal conductivity material. To enable the measurement of thermal properties of this material across different forms (individual fiber, fiber bundle/yarn, woven fabric), an in-house steady state thermal characterization technique based on infrared thermography has been developed. The experiments presented in this work establish the validity of the measurement technique for the materials characterized in this study, and also demonstrate the generality of the method for in-plane thermal characterization of different materials. Additionally, prototype plain-weave fabrics constructed from the high conductivity UHMW-PE fibers are measured to have a very high in-plane thermal conductivity ($\sim 10 \text{ Wm}^{-1}\text{K}^{-1}$) in the dominant heat conduction direction. This finding is also supported by the results obtained from a reduced-order heat conduction model developed to predict the thermal properties of the woven fabrics. Ultimately, the results from this study have demonstrated great potential for scalability of thermally conductive polymer fibers, especially for applications in low-power flexible and wearable electronic devices.

This work also comprehensively characterizes the thermal and mechanical properties of commercial fabrics that are relevant for heat spreading applications in flexible and wearable devices. Suitable high-performance polymer materials are surveyed, identifying Dyneema® fibers

⁵ Portions of this section are adapted from our published work (Candadai *et al.*¹¹⁰) and a recently submitted paper

as an ideal candidate for construction of heat spreading textiles and substrates. The thermal conductivity and bending stiffness of fabrics constructed from these fibers are characterized using in-house thermal and mechanical metrology techniques, demonstrating great promise for such applications. Compared to other conventional heat spreading and textile materials of comparable thickness, UHMW-PE fabrics possess a unique combination of high thermal conductivity and mechanical flexibility suitable for these applications. Moreover, additional tests conducted with respect to both mechanical and thermal reliability assessment suggest that these materials can be used reliably in wearable device technologies. Our findings related to these previously unexplored properties of existing commercial materials pave the way for further research in the development of novel materials constructed from UHMW-PE to enhance key thermal and mechanical properties for application-specific performance criteria. The mechanical characterization work provides a foundation to enable understanding of the bend stressing limits of these materials associated with desired levels of thermal performance, with key implications to device design and reliability in potential applications.

Finally, a measurement method to characterize the in-plane thermal anisotropy of a material is demonstrated through numerical simulations and experimental demonstrations. The proposed technique is a modification of the traditional Angstrom method and combines infrared thermography and non-contact optical heating to enable anisotropic thermal characterization of materials. We demonstrate that this method is applicable for measurement of a wide range of thermal conductivities along different orthotropic directions by controlling the measurement parameters involved. The tunability of this measurement approach is particularly beneficial towards addressing thermal metrology challenges that arise during characterization of different types of materials both at the microscale and the macroscale. Additionally, this method can also

be used for device-level performance characterization of substrate materials for directional heat spreading, hotspot thermal management, and electronics packaging applications.

The results from the present study have helped develop a fundamental physical understanding of the thermal properties of high-performance polymer materials as they are scaled up from the microscale to practically usable macroscale materials such as woven fabrics. Overall, the major outcome of this research has been the development of metrology techniques using basic heat transfer and engineering principles that are broadly applicable for the thermal characterization of various materials across different forms, length-scales, and directions. This has enabled identification of desirable properties in a specific category of high-performance polymer materials with great promise for use in flexible/wearable device applications.

7.2 Future Research Directions

The primary focus of the present thesis work spans fundamental physics and applied engineering areas related to thermal metrology of high-performance polymer materials. The potential directions for future research in these areas is summarized based in Table 7.1 and details are discussed below:

Table 7.1: Topic Coverage of Future Research Directions

	Metrology	Materials
Fundamental Physics	<ul style="list-style-type: none"> • Development of IR-Laser Angstrom method as a standard characterization approach • Related experimental work to validate the numerical approach for anisotropic materials and measure fabrics/thin films of interest 	<ul style="list-style-type: none"> • Experimental investigation of thermal conductivity enhancements of fibers by thermal annealing/fusing, and addition of high thermal conductivity filler materials such as carbon • Experiments and thermal modeling to understand role of interfacial contact resistances in fibers/yarns
Applications	<ul style="list-style-type: none"> • Device-level performance metrology applied to materials of interest such as composite fabric and film-based heat spreaders • IR-based characterization and associated modeling of wearable electronics packages accounting for interface resistances and skin contact 	<ul style="list-style-type: none"> • Modeling based investigation of novel weave designs/3D fabrics using UHMW-PE to tune properties along specific directions • Application-based reliability testing: effect of washing and drying cycles, thermal cycling, etc. on fabric properties

7.2.1 Metrology related

The laser-based IR Angstrom method discussed in Chapter 6 can be further developed as a diverse and robust standardized anisotropic characterization technique by further investigating the measurement parameter space. Specific experimental and modeling tasks in this direction could include: (1) performing detailed numerical experiments/simulations and analysis across a range of in-plane and through-plane thermal conductivities, sample thicknesses, heating frequencies and experimental setup dimensions to develop a thorough understanding of measurement tunability; (2) detailed error analysis across a range of these parameters to understand the limits of measurement depending on relative sample properties; (3) uncertainty propagation and sensitivity analysis based on numerical experiments; (4) accounting for natural convection coefficient in the

numerical model; (5) performing experiments for both isotropic and in-plane anisotropic materials at multiple frequencies and input laser power levels to develop a model fitting approach across different input parameters to minimize error (particularly crucial for highly anisotropic materials); (6) using optical techniques or more-circular laser beams with lower spot sizes to minimize some of the experimental challenges and reduce noise in the data; (7) developing a more refined experimental facility to enable efficient characterization of samples across a range of forms and property ranges; (8) using data from several numerical simulations to develop a reduced-order neural network model to enable efficient extraction of thermal properties from IR surface temperature map images, which may be specifically useful for quick in-situ characterization analysis; and, (9) combining concepts of the 1D radial-Angstrom analysis and the 2D cartesian orthotropic thermal conductivity analysis to develop a comprehensive thermal model in radial coordinates to accurately predict angular variation of thermal conductivity.

Since the proposed experimental setup is also useful for device-level thermal performance characterization, the in-plane heat spreading properties of different materials of interest such as composite fabric and film-based heat spreaders can be characterized and benchmarked. A test device can be constructed by mounting/embedding on/in the woven fabrics to test a representative wearable cooling solution, and the performance of the device can be evaluated using IR thermography. The performance of wearable electronic packages under different transient power input conditions can also be well understood using this method. Associated thermal modeling of wearable electronics packages accounting for interface resistances and skin contact can be performed to inform their thermal design in application-specific scenarios.

7.2.2 Materials

In the materials focus area, experimental approaches can be explored to further enhance the baseline thermal properties of UHMW-PE based fibers and fabrics. Thermal modeling and complementary experiments are needed to estimate the interfacial contact resistances in fibers and yarns and understand their role on effective thermal properties, as they may be more important for complex fabric weave geometries. Experimental investigation of thermal conductivity enhancements of fibers by thermal annealing or fusing of the fibers to reduce inter-fiber and inter-yarn contact resistances in the fabric can be carried out. Addition of high thermal conductivity fillers such as carbon-based materials can be also be explored to improve thermal properties depending on the desired application.

Thermal modeling of novel planar fabric weave configurations and 3D fabrics constructed from UHMW-PE can be performed by significantly improving the reduced-order model developed in the present work to understand the effect of anisotropic weave properties. The current results from the reduced-order model indicate that inter-yarn thermal contact resistances can play a significant role in determining the effective thermal conductivity of different weave configurations depending on the orientation of the yarns with respect to the primary heat flow direction. Modeling based investigation of novel planar weave designs as well as three-dimensional fabrics constructed using can be performed to tune properties along specific directions.

Further characterization of properties of UHMW-PE fabrics is needed specifically with respect to understanding their reliability during operation. The effect of washing and drying cycles, long-duration thermal cycling, transient thermal loads etc. on the thermal properties of the fabrics can be investigated.

The proposed future directions can further build on the findings of this thesis work to provide a strong foundation for heat spreading applications leveraging properties of novel materials to

assist thermal management solutions during design and engineering of future flexible and wearable electronics.

APPENDIX A. BENDING STIFFNESS

Validation using Plate Theory

An approximate validation of the bend testing measurement approach, similar to that adopted by Lammens et al. ¹³⁹, is done by comparing the measured value for a Kapton® (polyimide) film to the predicted bending stiffness using plate theory. For a solid film, the stiffness is given by:

$$G = \frac{Et^3}{12(1-\nu^2)},$$

where E is Young's Modulus (Pa), t is the thickness of the material (m), and ν is Poisson's ratio. Note that plate theory is not used as a theoretical comparison for the fabric samples measured in this study because it is applicable only for isotropic solid materials. The stiffness based on plate theory for the Kapton® film is calculated to be $4.83 \times 10^{-4} Nm$, while the measured stiffness at a bending angle of 7.1° is $(2.7 \pm 0.8) \times 10^{-4} Nm$. This comparison is also shown in Fig A1, alongside the other bending stiffness measurements. Considering that bending stiffness for the materials spans multiple orders of magnitude, this order of agreement between the theoretical value and the measured value is reasonable for the purposes of estimating and benchmarking the bending stiffness of the fabrics considered in this study.

Measurements at Two Bending Angles

The measurement of bending stiffness is performed at two different angles for each sample (41.5° and 7.1°) except for HDPE and cotton as mentioned in the manuscript. The measured data are plotted in Fig A1 which demonstrates a reasonable agreement between the results at the two different bending angles.

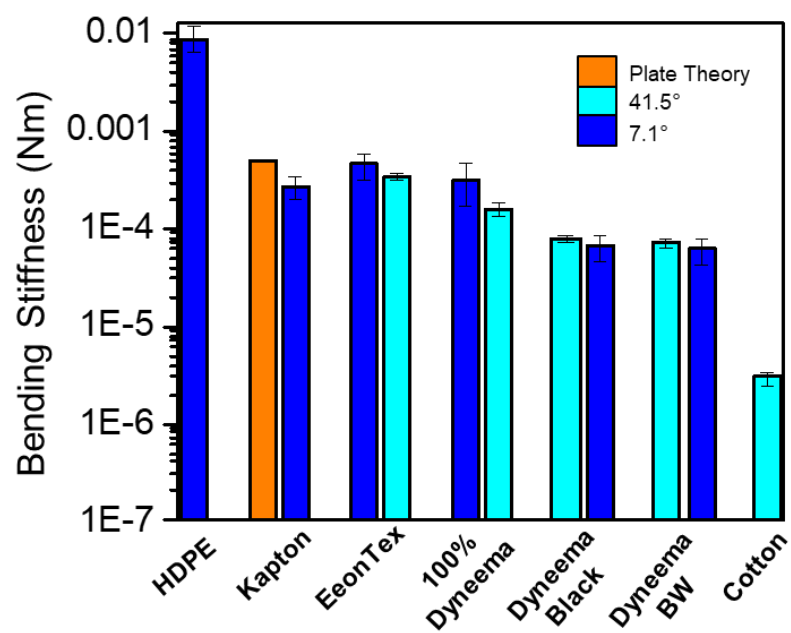


Figure A1: Measured bending stiffness (flexural rigidity) of all materials characterized at different bending angles. The measurements at and 7.1° and 41.5° are in reasonably good agreement.

APPENDIX B. DIFFERENTIAL SCANNING CALORIMETRY MEASUREMENTS

Differential Scanning Calorimetry (DSC) measurements are performed using a DSC system (NETZSCH DSC 2014 Polyma) to assess the impact of annealing of the Dyneema® fibers and fabrics at different temperatures approaching the melting point. Fig B1a and B1b show the DSC response curves for Dyneema® fibers and the Dyneema® Black fabric, respectively, for as-received samples as well as for those subjected to annealing at different temperatures (100, 115, 130, 145°C) for 1 hr. From these plots, we see that the melting peak for the Dyneema® fibers occurs at ~147°C, and that for the Dyneema® denim fabric occurs at ~149°C. This is in good agreement with the expected melting range of 147-152°C for Dyneema®¹⁴¹.

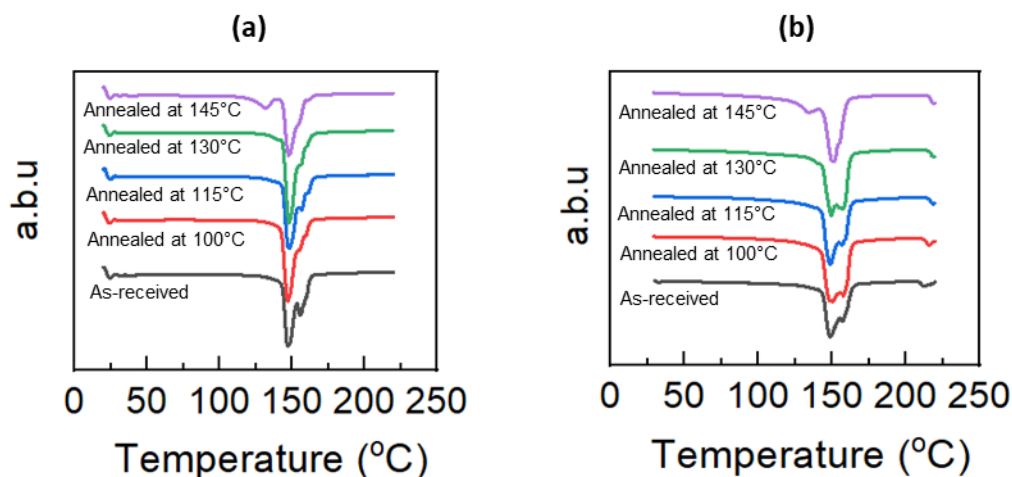


Figure B1: DSC response curves for (a) Dyneema® fibers and (b) a Dyneema® Black fabric, measured for as-received samples and for samples subjected to annealing at the different temperatures indicated. The early melting peak can be noted for the samples annealed at 145°C.

The results from Figure B1 also indicate no significant change in the DSC response for both fibers and fabrics, except for the samples subjected to annealing at the highest temperature condition of 145°C. For these samples (for both the fiber and the fabric), the onset of melting begins earlier as

indicated by the short melting peak ($\sim 133\text{-}135^{\circ}\text{C}$) that precedes the more prominent, deep peak. This is because of the melting and recrystallization of a small fraction of polymer during and after the annealing process at 145°C . This fraction of polymer which is no longer highly crystalline and oriented then melts at a lower temperature during the DSC measurement, which is seen as an early, short melting peak in the response curve. Since the DSC response changes significantly only for the 145°C condition, the other temperature conditions are inferred to have no significant effect on the intrinsic crystallinity or thermal conductivity of the fabrics.

These DSC measurements guide our choice of using the fabric samples annealed at 145°C for 1 hour to assess the thermal stability of these materials as pertaining to the thermal conductivity, as reported in the manuscript.

APPENDIX C. FIN HEAT CONDUCTION ANALYSIS OF ANNEALED DYNEEMA FABRICS

A fin-based heat conduction analysis is used to obtain a relative measure of thermal conductivity of the Dyneema® fabric before and after annealing. A Dyneema® control fabric sample and an annealed fabric (at 145°C for 1 hour) are suspended between a heater block and cold block maintained at 20°C as shown in Fig C1. At a fixed heater power, steady state infrared (IR) temperature maps can be used to extract the relative thermal conductivity of the two samples by comparing the experimental temperature profile along the length of the sample and the theoretical temperature profile using the temperature distribution for a fin with prescribed tip temperature. For each sample, the theoretical temperature is given by ¹⁴⁴:

$$\frac{\theta(x)}{\theta_b} = \left(\frac{(\theta_L/\theta_b) \sinh(mx) + \sinh m(L-x)}{\sinh mL} \right),$$

where, for each sample (control or annealed), θ is the temperature rise (with respect to ambient) as a function of length θ_b is the difference between the base temperature (temperature at the heated end) and ambient temperature, L is the sample length, θ_L is the difference between the prescribed tip temperature (obtained from the IR image) and the ambient temperature, and m is a non-dimensional parameter given by $\sqrt{\frac{hP}{kA}}$. Since the two fabric samples are cut to be of the same size and geometry, they have the same convection heat transfer coefficient h , perimeter P , and cross-sectional area A . Using the above equation, the parameter m can be individually obtained by fitting with the experimental steady state temperature profile as a function of length. Following this, the ratio of the thermal conductivities of the control and annealed samples (k_1/k_2) can be obtained. By shifting the location at which the base temperature is measured by a few pixels away from the heated end (up to ~1 mm away), four values of k_1/k_2 are calculated to provide a measure of

uncertainty in this measurement. The calculated ratio ranges from ~ 0.81 – 1.06 , indicating that the thermal conductivity of the control and annealed sample are estimated to be the same to within experimental uncertainty.

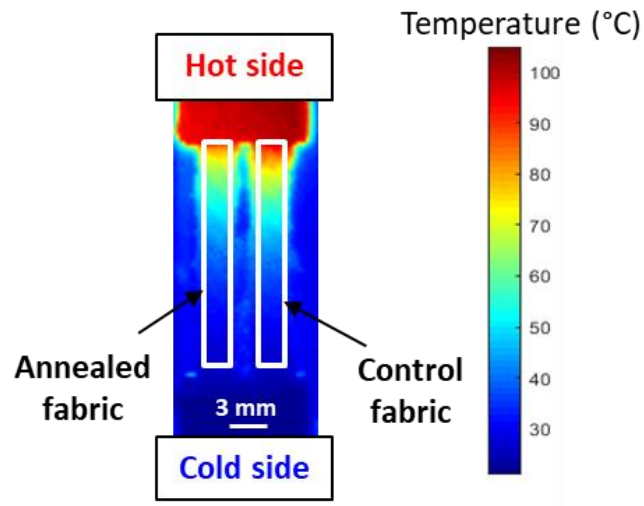


Figure C1: IR temperature image of the experimental test setup used to compare the relative in-plane thermal conductivities of a control fabric sample and an annealed (at 145°C for 1 hour) fabric sample.

A visual demonstration was also carried out by capturing a video to illustrate the transient temperature distribution of both samples captured by the IR microscope after the heater is turned on. This provided a qualitative comparison of the in-plane heat spreading in both samples and indicated that there is no noticeable or significant change in the thermal conductivity.

APPENDIX D. ANALYTICAL SOLUTION FOR 1D RADIAL-ANGSTROM METHOD

Consider the heat diffusion equation:

$$\frac{\partial^2 T}{\partial r^2} + \frac{1}{r} \frac{\partial T}{\partial r} = \frac{1}{\alpha} \frac{\partial T}{\partial t}$$

The boundary conditions at two radial locations at the inner and outer boundaries are considered as periodic conditions in temperature:

$$T(r = a, t) = \frac{T_a}{2} e^{i\omega t} + \frac{T_a}{2} e^{-i\omega t}$$

$$T(r = b, t) = \frac{T_b}{2} e^{i(\omega t - \phi_b)} + \frac{T_b}{2} e^{-i(\omega t + \phi_b)}$$

Assume a solution of the form, $T(r, t) = T_1 e^{i\omega t} + T_2 e^{-i\omega t}$ and plug into the differential equation.

Consider the $T_1 e^{i\omega t}$ part of solution:

$$\frac{\partial^2}{\partial r^2} (T_1 e^{i\omega t}) + \frac{1}{r} \frac{\partial}{\partial r} (T_1 e^{i\omega t}) = \frac{1}{\alpha} \frac{\partial}{\partial t} (T_1 e^{i\omega t})$$

Solving, we can obtain an ordinary differential equation for $T_1(r)$ as shown below:

$$\frac{d^2 T_1}{dr^2} + \frac{1}{r} \frac{dT_1}{dr} - \frac{i\omega}{\alpha} T_1 = 0$$

This has a general solution given by:

$$T_1(r) = c_1 J_0 \left((-1)^{\frac{3}{4}} \sqrt{\frac{\omega}{\alpha}} r \right) + c_2 Y_0 \left(-(-1)^{\frac{3}{4}} \sqrt{\frac{\omega}{\alpha}} r \right)$$

Applying the boundary conditions $T_1(r = a) = \frac{T_a}{2}$ and $T_1(r = b) = \frac{T_b}{2} e^{-i\phi_b}$, we get two

simultaneous equations to solve for the unknown constants.

$$\frac{T_a}{2} = c_1 J_0 \left((-1)^{\frac{3}{4}} \sqrt{\frac{\omega}{\alpha}} a \right) + c_2 Y_0 \left(-(-1)^{\frac{3}{4}} \sqrt{\frac{\omega}{\alpha}} a \right)$$

$$\frac{T_b}{2} e^{-i\phi_b} = c_1 J_0 \left((-1)^{\frac{3}{4}} \sqrt{\frac{\omega}{\alpha}} b \right) + c_2 Y_0 \left(-(-1)^{\frac{3}{4}} \sqrt{\frac{\omega}{\alpha}} b \right)$$

Solving these equations yields the constants and therefore we can obtain an expression for $T_1(r)$.

Applying a similar approach using the general solution and boundary conditions given below, we can solve for $T_2(r)$:

$$T_2(r) = c_3 J_0 \left((-1)^{\frac{1}{4}} \sqrt{\frac{\omega}{\alpha}} r \right) + c_4 Y_0 \left(-(-1)^{\frac{1}{4}} \sqrt{\frac{\omega}{\alpha}} r \right)$$

$$T_2(r = a) = \frac{T_a}{2}; T_2(r = b) = \frac{T_b}{2} e^{-i\phi_b}$$

Finally, the solution is then given as:

$$T(r, t) = T_1(r) e^{i\omega t} + T_2(r) e^{-i\omega t}$$

where,

$$T_1(r) = \frac{e^{-i\phi_b} \left(J_0 \left((-1)^{\frac{3}{4}} \sqrt{\frac{\omega}{\alpha}} r \right) \left(\frac{T_b}{2} Y_0 \left(-(-1)^{\frac{3}{4}} \sqrt{\frac{\omega}{\alpha}} a \right) - \frac{T_a}{2} e^{i\phi_b} Y_0 \left(-(-1)^{\frac{3}{4}} \sqrt{\frac{\omega}{\alpha}} b \right) \right) - Y_0 \left(-(-1)^{\frac{3}{4}} \sqrt{\frac{\omega}{\alpha}} r \right) \left(\frac{T_b}{2} J_0 \left((-1)^{\frac{3}{4}} \sqrt{\frac{\omega}{\alpha}} a \right) - \frac{T_a}{2} e^{i\phi_b} J_0 \left((-1)^{\frac{3}{4}} \sqrt{\frac{\omega}{\alpha}} b \right) \right) \right)}{Y_0 \left(-(-1)^{\frac{3}{4}} \sqrt{\frac{\omega}{\alpha}} a \right) J_0 \left((-1)^{\frac{3}{4}} \sqrt{\frac{\omega}{\alpha}} b \right) - J_0 \left((-1)^{\frac{3}{4}} \sqrt{\frac{\omega}{\alpha}} a \right) Y_0 \left(-(-1)^{\frac{3}{4}} \sqrt{\frac{\omega}{\alpha}} b \right)},$$

$$T_2(r) = \frac{e^{-i\phi_b} \left(J_0 \left((-1)^{\frac{1}{4}} \sqrt{\frac{\omega}{\alpha}} r \right) \left(\frac{T_b}{2} Y_0 \left(-(-1)^{\frac{1}{4}} \sqrt{\frac{\omega}{\alpha}} a \right) - \frac{T_a}{2} e^{i\phi_b} Y_0 \left(-(-1)^{\frac{1}{4}} \sqrt{\frac{\omega}{\alpha}} b \right) \right) - Y_0 \left(-(-1)^{\frac{1}{4}} \sqrt{\frac{\omega}{\alpha}} r \right) \left(\frac{T_b}{2} J_0 \left((-1)^{\frac{1}{4}} \sqrt{\frac{\omega}{\alpha}} a \right) - \frac{T_a}{2} e^{i\phi_b} J_0 \left((-1)^{\frac{1}{4}} \sqrt{\frac{\omega}{\alpha}} b \right) \right) \right)}{Y_0 \left(-(-1)^{\frac{1}{4}} \sqrt{\frac{\omega}{\alpha}} a \right) J_0 \left((-1)^{\frac{1}{4}} \sqrt{\frac{\omega}{\alpha}} b \right) - J_0 \left((-1)^{\frac{1}{4}} \sqrt{\frac{\omega}{\alpha}} a \right) Y_0 \left(-(-1)^{\frac{1}{4}} \sqrt{\frac{\omega}{\alpha}} b \right)}.$$

REFERENCES

1. Tao, X. & Textile Institute (Manchester, E. *Wearable electronics and photonics*. (CRC Press, 2005).
2. Wang, X. *et al.* Flexible Energy-Storage Devices: Design Consideration and Recent Progress. *Adv. Mater.* **26**, 4763–4782 (2014).
3. Kim, D.-H. *et al.* Ultrathin Silicon Circuits With Strain-Isolation Layers and Mesh Layouts for High-Performance Electronics on Fabric, Vinyl, Leather, and Paper. *Adv. Mater.* **21**, 3703–3707 (2009).
4. Bauer, S. Sophisticated skin. *Nat. Mater.* **12**, 871–872 (2013).
5. Gates, B. D. Flexible Electronics. *New Ser.* **323**, 1566–1567 (2009).
6. Park, S. & Jayaraman, S. Smart textiles: Wearable electronic systems. *MRS Bull.* **28**, 585–591 (2003).
7. Gniotek, K. & Krucińska, I. The basic problems of textronics. *Fibres Text. East. Eur.* **12**, 13–16 (2004).
8. Garimella, S. V, Persoons, T., Weibel, J. A. & Gektin, V. Electronics Thermal Management in Information and Communications Technologies: Challenges and Future Directions. *IEEE Trans. Components, Packag. Manuf. Technol.* **7**, 1191–1205 (2017).
9. Hu, L. *et al.* Stretchable, porous, and conductive energy textiles. *Nano Lett.* **10**, 708–714 (2010).
10. Lee, H. M., Choi, S.-Y., Jung, A. & Ko, S. H. Highly Conductive Aluminum Textile and Paper for Flexible and Wearable Electronics. *Angew. Chemie Int. Ed.* **52**, 7718–7723 (2013).
11. Stoppa, M., Chiolerio, A., Stoppa, M. & Chiolerio, A. Wearable Electronics and Smart Textiles: A Critical Review. *Sensors* **14**, 11957–11992 (2014).
12. Jin, J., Ko, J.-H., Yang, S. & Bae, B.-S. Rollable Transparent Glass-Fabric Reinforced Composite Substrate for Flexible Devices. *Adv. Mater.* **22**, 4510–4515 (2010).
13. Grancarić, A. M. *et al.* Conductive polymers for smart textile applications. **48**, 612–642 (2018).
14. Maity, S., Chatterjee, A., Singh, B. & Pal Singh, A. Polypyrrole based electro-conductive textiles for heat generation. *J. Text. Inst.* **105**, 887–893 (2014).
15. Ala, O. & Fan, Q. Applications of Conducting Polymers in Electronic Textiles. *Res. J. Text. Appar.* **13**, 51–68 (2009).

16. Bajgar, V. *et al.* Cotton fabric coated with conducting polymers and its application in monitoring of carnivorous plant response. *Sensors (Switzerland)* **16**, 498 (2016).
17. Mohanty, N. *et al.* Nanotomy-based production of transferable and dispersible graphene nanostructures of controlled shape and size. *Nat. Commun.* **3**, 844 (2012).
18. Kuzum, D. *et al.* Transparent and flexible low noise graphene electrodes for simultaneous electrophysiology and neuroimaging. *Nat. Commun.* **5**, 5259 (2014).
19. Wang, X. *et al.* A spectrally tunable all-graphene-based flexible field-effect light-emitting device. *Nat. Commun.* **6**, 7767 (2015).
20. Trung, T. Q., Ramasundaram, S. & Lee, N. E. Infrared Detection Using Transparent and Flexible Field-Effect Transistor Array with Solution Processable Nanocomposite Channel of Reduced Graphene Oxide and P(VDF-TrFE). *Adv. Funct. Mater.* **25**, 1745–1754 (2015).
21. Zeng, X. *et al.* Fibrous Epoxy Substrate with High Thermal Conductivity and Low Dielectric Property for Flexible Electronics. *Adv. Electron. Mater.* **2**, 1500485 (2016).
22. Moore, A. L. & Shi, L. Emerging challenges and materials for thermal management of electronics. *Materials (Basel)*. **17**, (2014).
23. Pola, T., Häkkinen, T., Hännikäinen, J. & Vanhala, J. Thermal Performance Analysis of 13 Heat Sink Materials Suitable for Wearable Electronics Applications. *Sci. Technol.* **3**, 67–73 (2013).
24. *High-Temperature Properties and Applications of Polymeric Materials*. **603**, (American Chemical Society, 1995).
25. Dunn, A. S. Introduction to physical polymer science (2nd edition). By L. H. Sperling, New York, 1992 John Wiley & Sons Inc. John Wiley & Sons Inc., New York, 1992. pp. xxvii + 594, price £55.00. ISBN 0-471-53035-2. *Polym. Int.* **33**, 233–233 (1994).
26. Choy, C. L. Thermal conductivity of polymers. *Polymer (Guildf)*. **18**, 984–1004 (1977).
27. Kim, G.-H. *et al.* High thermal conductivity in amorphous polymer blends by engineered interchain interactions. *Nat. Mater.* **14**, 295–300 (2015).
28. Mamunya, Y. P., Davydenko, V. V., Pissis, P. & Lebedev, E. V. Electrical and thermal conductivity of polymers filled with metal powders. *Eur. Polym. J.* **38**, 1887–1897 (2002).
29. Ngo, I.-L., Jeon, S. & Byon, C. Thermal conductivity of transparent and flexible polymers containing fillers: A literature review. *Int. J. Heat Mass Transf.* **98**, 219–226 (2016).
30. Li, A. *et al.* Thermal Conductivity of Graphene-Polymer Composites: Mechanisms, Properties, and Applications. *Polymers (Basel)*. **9**, 437 (2017).

31. Huang, X., Jiang, P. & Tanaka, T. A review of dielectric polymer composites with high thermal conductivity. *IEEE Electr. Insul. Mag.* **27**, 8–16 (2011).
32. Shenogina, N., Shenogin, S., Xue, L. & Keblinski, P. On the lack of thermal percolation in carbon nanotube composites. *Appl. Phys. Lett.* **87**, 133106 (2005).
33. Kargar, F. *et al.* Thermal Percolation Threshold and Thermal Properties of Composites with High Loading of Graphene and Boron Nitride Fillers. *ACS Appl. Mater. Interfaces* **10**, 37555–37565 (2018).
34. Zhong, Z. *et al.* Structure-induced enhancement of thermal conductivities in electrospun polymer nanofibers. *Nanoscale* **6**, 8283–8291 (2014).
35. Singh, V. *et al.* High thermal conductivity of chain-oriented amorphous polythiophene. *Nat. Nanotechnol.* **9**, 384–390 (2014).
36. Shen, S., Henry, A., Tong, J., Zheng, R. & Chen, G. Polyethylene nanofibres with very high thermal conductivities. *Nat. Nanotechnol.* **5**, 251–255 (2010).
37. Park, J. H. & Rutledge, G. C. Ultrafine high performance polyethylene fibers Publisher Springer-Verlag Terms of Use Creative Commons Attribution-Noncommercial-Share Alike Ultrafine High Performance Polyethylene Fibers. *J. Mater. Sci.* **53**, 3049–3063 (2017).
38. Reto Haggenmueller, †, Csaba Guthy, †, Jennifer R. Lukes, ‡, John E. Fischer, † and & Karen I. Winey*, †. Single Wall Carbon Nanotube/Polyethylene Nanocomposites: Thermal and Electrical Conductivity. (2007). doi:10.1021/MA0615046
39. Vasileiou, A. A., Kontopoulou, M. & Docoslis, A. A Noncovalent Compatibilization Approach to Improve the Filler Dispersion and Properties of Polyethylene/Graphene Composites. *ACS Appl. Mater. Interfaces* **6**, 1916–1925 (2014).
40. Mergenthaler, D. B., Pietralla, M., Roy, S. & Kilian, H.-G. Thermal Conductivity in Ultraoriented Polyethylene. *Macromolecules* **25**, 3500–3502 (1992).
41. Wang, X., Ho, V., Segalman, R. A. & Cahill, D. G. Thermal conductivity of high-modulus polymer fibers. *Macromolecules* **46**, 4937–4943 (2013).
42. Ghasemi, H. *et al.* High thermal conductivity ultra-high molecular weight polyethylene (UHMWPE) films. *Thermomechanical Phenom. Electron. Syst. -Proceedings Intersoc. Conf.* 235–239 (2014). doi:10.1109/ITHERM.2014.6892287
43. Xu, Y. *et al.* Nanostructured polymer films with metal-like thermal conductivity. *Nat. Commun.* **10**, 1771 (2019).
44. Nakajima, T., Kajiwar, K. & McIntyre, J. E. *Advanced Fiber Spinning Technology*. *Advanced Fiber Spinning Technology* (1994). doi:10.1533/9781845693213

45. Hearle, J. W. S. & Textile Institute (Manchester, E. *High-performance fibres*. (CRC Press, 2001).
46. DSM. Ultra High Molecular Weight Polyethylene Fiber from DSM Dyneema. *Technical DataSheet* (2016). Available at: <https://issuu.com/eurofibers/docs/name8f0d44>.
47. Honeywell. Technical Specifications - Spectra Fiber. Available at: <https://www.spectra-fiber.com/technical-specifications/>. (Accessed: 5th July 2019)
48. Hoogsteen, W., van der Hooft, R. J., Postema, A. R., ten Brinke, G. & Pennings, A. J. Gel-spun polyethylene fibres. *J. Mater. Sci.* **23**, 3459–3466 (1988).
49. Litvinov, V. M. *et al.* Morphology, Chain Dynamics, and Domain Sizes in Highly Drawn Gel-Spun Ultrahigh Molecular Weight Polyethylene Fibers at the Final Stages of Drawing by SAXS, WAXS, and ^1H Solid-State NMR. *Macromolecules* **44**, 9254–9266 (2011).
50. Zwijnenburg, A. & Pennings, A. J. Longitudinal growth of polymer crystals from flowing solutions III. Polyethylene crystals in Couette flow. *Colloid Polym. Sci.* **254**, 868–881 (1976).
51. Deitzel, J. M., McDaniel, P. & Gillespie, J. W. High performance polyethylene fibers. in *Structure and Properties of High-Performance Fibers* 167–185 (Elsevier Inc., 2017). doi:10.1016/B978-0-08-100550-7.00007-3
52. Smith, P. & Lemstra, P. J. Ultra-high-strength polyethylene filaments by solution spinning/drawing. *J. Mater. Sci.* **15**, 505–514 (1980).
53. Smith, P., Lemstra, P., Kalb, B. & Pennings, A. Ultrahigh-strength polyethylene filaments by solution spinning and hot drawing. *Polym. Bull.* **1**, 733–736 (1979).
54. Kikutani, T. Formation and structure of high mechanical performance fibers. II. Flexible polymers. *J. Appl. Polym. Sci.* **83**, 559–571 (2002).
55. NPTEL Textile Engineering. High Strength High Modulus Fibers. Available at: <https://nptel.ac.in/courses/116102006/6>. (Accessed: 8th July 2019)
56. Clark, E. S. & Scott, L. S. Superdrawn crystalline polymers: A new class of high-strength fiber. *Polym. Eng. Sci.* **14**, 682–686 (1974).
57. Kanamoto, T., Sherman, E. S. & Porter, R. S. Extrusion of Polyethylene Single Crystals. *Polym. J.* **11**, 497–502 (1979).
58. Smith, P. & Lemstra, P. J. Ultra-high strength polyethylene filaments by solution spinning/drawing. 3. Influence of drawing temperature. *Polymer (Guildf)*. **21**, 1341–1343 (1980).
59. Choy, C. ., Luk, W. . & Chen, F. . Thermal conductivity of highly oriented polyethylene. *Polymer (Guildf)*. **19**, 155–162 (1978).

60. Choy, C. L. & Young, K. Thermal conductivity of semicrystalline polymers — a model. *Polymer (Guildf)*. **18**, 769–776 (1977).
61. Choy, C. L., Fei, Y. & Xi, T. G. Thermal conductivity of gel-spun polyethylene fibers. *J. Polym. Sci. Part B Polym. Phys.* **31**, 365–370 (1993).
62. Choy, C. L. & Leung, W. P. Thermal conductivity of ultradrawn polyethylene. *J. Polym. Sci. Polym. Phys. Ed.* **21**, 1243–1246 (1983).
63. Bergman, T. L. & Incropera, F. P. *Fundamentals of heat and mass transfer*. (Wiley, 2011).
64. Kasap, S., Málek, J. & Svoboda, R. Thermal Properties and Thermal Analysis: Fundamentals, Experimental Techniques and Applications. in *Springer Handbook of Electronic and Photonic Materials* 1–1 (Springer International Publishing, 2017). doi:10.1007/978-3-319-48933-9_19
65. Zhao, D., Qian, X., Gu, X., Jajja, S. A. & Yang, R. Measurement Techniques for Thermal Conductivity and Interfacial Thermal Conductance of Bulk and Thin Film Materials. *J. Electron. Packag.* **138**, 040802 (2016).
66. ASTM International. Standard Test Method for Steady-State Heat Flux Measurements and Thermal Transmission Properties by Means of the Guarded-Hot-Plate. *ASTM C177* 1–23 (2013). doi:10.1520/C0177-13.2
67. Pope, A. L., Zawilski, B. & Tritt, T. M. *Description of removable sample mount apparatus for rapid thermal conductivity measurements*.
68. Liu, W. & Asheghi, M. Thermal Conductivity Measurements of Ultra-Thin Single Crystal Silicon Layers. *J. Heat Transfer* **128**, 75 (2006).
69. Marconnet, A. M., Kodama, T., Asheghi, M. & Goodson, K. E. Phonon Conduction in Periodically Porous Silicon Nanobridges. *Nanoscale Microscale Thermophys. Eng.* **16**, 199–219 (2012).
70. Li, D. *et al.* Measuring Thermal and Thermoelectric Properties of One-Dimensional Nanostructures Using a Microfabricated Device. (2003). doi:10.1115/1.1597619
71. ASTM International. Standard Test Method for Thermal Conductivity of Solids Using the Guarded-Comparative-Longitudinal Heat Flow Technique. *ASTM E1225* i, 1–10 (2013).
72. Kantharaj, R. *et al.* Thermal conduction in graphite flake-epoxy composites using infrared microscopy. in *2017 16th IEEE Intersociety Conference on Thermal and Thermomechanical Phenomena in Electronic Systems (ITherm)* 1–7 (IEEE, 2017). doi:10.1109/ITHERM.2017.8023960
73. Marconnet, A. M., Yamamoto, N., Panzer, M. A., Wardle, B. L. & Goodson, K. E. Thermal Conduction in Aligned Carbon Nanotube–Polymer Nanocomposites with High Packing Density. **20**, 45 (2019).

74. McNamara, A. J., Joshi, Y. K. & Zhang, Z. M. Characterization of Nanostructured Thermal Interface Materials - A Review. in *Proceeding of TMNN-2011. Proceedings of the International Symposium on Thermal and Materials Nanoscience and Nanotechnology - 29 May - 3 June , 2011, Antalya, Turkey* 14 (Begellhouse, 2011). doi:10.1615/ICHMT.2011.TMNN-2011.320
75. Hu, X. J., Panzer, M. A. & Goodson, K. E. Infrared Microscopy Thermal Characterization of Opposing Carbon Nanotube Arrays. *J. Heat Transfer* **129**, 91–93 (2007).
76. Tritt, T. M. *Thermal Conductivity: Theory, Properties, and Applications*. (Kluwer Academic/Plenum Publishers, New York, 2004).
77. Zawilski, B. M., Littleton Iv, R. T. & Tritt, T. M. *Measurement of small sample thermal conductivity by parallel thermal conductance technique*.
78. Wang, J. L., Gu, M., Zhang, X. & Song, Y. Thermal conductivity measurement of an individual fibre using a T type probe method. *J. Phys. D. Appl. Phys.* **42**, (2009).
79. Zhang, X., Fujiwara, S. & Fujii, M. Measurements of thermal conductivity and electrical conductivity of a single carbon fiber. *Int. J. Thermophys.* **21**, 965–980 (2000).
80. Wang, J.-L., Gu, M., Ma, W., Zhang, X. & Song, Y. Temperature dependence of the thermal conductivity of individual pitch-derived carbon fibers. *Carbon N. Y.* **47**, 353 (2009).
81. Zeng, Y. & Marconnet, A. A direct differential method for measuring thermal conductivity of thin films. *Rev. Sci. Instrum.* **88**, (2017).
82. Parker, W. J., Jenkins, R. J., Butler, C. P. & Abbott, G. L. Flash Method of Determining Thermal Diffusivity, Heat Capacity, and Thermal Conductivity. *J. Appl. Phys.* **32**, 1679–1684 (1961).
83. Taylor, R. E., Gembarovic, J. & Maglic, K. D. Thermal Diffusivity by the Laser Flash Technique. *Charact. Mater.* (2002). doi:10.1002/0471266965.com102
84. Vozár, L. & Hohenauer, W. Flash method of measuring the thermal diffusivity a review. *High Temp. - High Press.* **35–36**, 253–264 (2003).
85. Laser flash analysis - Wikiwand. Available at: http://www.wikiwand.com/en/Laser_flash_analysis. (Accessed: 5th November 2020)
86. Angström, A. J. New method of determining the thermal conductivity of bodies. *London, Edinburgh, Dublin Philos. Mag. J. Sci.* **25**, 130–142 (1863).
87. Hahn, J., Reid, T. & Marconnet, A. Infrared microscopy enhanced Angstrom's method for thermal diffusivity of polymer monofilaments and films. *J. Heat Transfer* **141**, 081601 (2019).

88. Hu, Y. & Fisher, T. S. Accurate Thermal Diffusivity Measurements Using a Modified Ångström's Method With Bayesian Statistics. *J. Heat Transfer* **142**, 1–9 (2020).
89. Zhu, J. *et al.* Ultrafast thermorefectance techniques for measuring thermal conductivity and interface thermal conductance of thin films. *J. Appl. Phys.* **108**, 094315 (2010).
90. Cahill, D. G. Thermal conductivity measurement from 30 to 750 K: the 3ω method. *Rev. Sci. Instrum.* **61**, 802–808 (1990).
91. Adams, W. W. & Eby, R. K. High-Performance Polymer Fibers. *MRS Bull.* **12**, 22–26 (1987).
92. Liu, J., Xu, Z., Cheng, Z., Xu, S. & Wang, X. Thermal Conductivity of Ultrahigh Molecular Weight Polyethylene Crystal : Defect Effect Uncovered by 0 K Limit Phonon Diffusion. 1–10 (2015). doi:10.1021/acsami.5b08578
93. Zhu, B. *et al.* Novel Polyethylene Fibers of Very High Thermal Conductivity Enabled by Amorphous Restructuring. *ACS Omega* **2**, 3931–3944 (2017).
94. Ma, J. *et al.* Thermal conductivity of electrospun polyethylene nano fibers. 16899–16908 (2015). doi:10.1039/c5nr04995d
95. Fujishiro, H., Ikebe, M., Kashima, T. & Yamanaka, A. Thermal Conductivity and Diffusivity of High-Strength Polymer Fibers. *Jpn. J. Appl. Phys.* **36**, 5633–5637 (1997).
96. Fujishiro, H., Ikebe, M., Kashima, T. & Yamanaka, A. Drawing Effect on Thermal Properties of High-Strength Polyethylene Fibers. *Jpn. J. Appl. Phys.* **37**, 1994–1995 (1998).
97. Ronca, S., Igarashi, T., Forte, G. & Rastogi, S. Metallic-like thermal conductivity in a lightweight insulator: Solid-state processed Ultra High Molecular Weight Polyethylene tapes and films. *Polymer (Guildf)*. **123**, 203–210 (2017).
98. Loomis, J. *et al.* Continuous fabrication platform for highly aligned polymer films. *TECHNOLOGY* **02**, 189–199 (2014).
99. Kaplan, S. & Okur, A. *Thermal comfort performance of sports garments with objective and subjective measurements. Indian Journal of Fibre & Textile Research* **37**, (2012).
100. Manshahia, M. & Das, A. *High active sportswear-A critical review. Indian Journal of Fibre & Textile Research* **39**, (2014).
101. Yang, Y., Stapleton, J., Diagne, B. T., Kenny, G. P. & Lan, C. Q. Man-portable personal cooling garment based on vacuum desiccant cooling. *Appl. Therm. Eng.* **47**, 18–24 (2012).
102. Bartkowiak, G., Dabrowska, A. & Marszalek, A. Assessment of an active liquid cooling garment intended for use in a hot environment. *Appl. Ergon.* **58**, 182–189 (2017).

103. Elbel, S., Bowers, C., Zhao, H., Park, S. & Hrnjak, P. Development Of Microclimate Cooling Systems For Increased Thermal Comfort Of Individuals Development of Microclimate Cooling Systems for Increased Thermal Comfort of Individuals. in *International Refrigeration and Air Conditioning Conference at Purdue* (2012).
104. Hsu, P. C. *et al.* Radiative human body cooling by nanoporous polyethylene textile. *Science* (80-.). **353**, 1019–1023 (2016).
105. Hsu, P. C. *et al.* A dual-mode textile for human body radiative heating and cooling. *Sci. Adv.* **3**, (2017).
106. Tong, J. K. *et al.* Infrared-Transparent Visible-Opaque Fabrics for Wearable Personal Thermal Management. *ACS Photonics* **2**, 769–778 (2015).
107. Gao, T. *et al.* Three-Dimensional Printed Thermal Regulation Textiles. (2017). doi:10.1021/acsnano.7b06295
108. Wang, J. *et al.* High temperature thermally conductive nanocomposite textile by ‘green’ electrospinning †. **10**, 16868 (2018).
109. Gong, J. *et al.* Graphene woven fabric-reinforced polyimide films with enhanced and anisotropic thermal conductivity. *Compos. Part A Appl. Sci. Manuf.* **87**, 290–296 (2016).
110. Candadai, A. A., Weibel, J. A. & Marconnet, A. M. Thermal Conductivity of Ultrahigh Molecular Weight Polyethylene: From Fibers to Fabrics. *ACS Appl. Polym. Mater.* **2**, 437–447 (2020).
111. Tang, Z., Yao, D., Du, D. & Ouyang, J. Highly machine-washable e-textiles with high strain sensitivity and high thermal conduction. *J. Mater. Chem. C* **8**, 2741–2748 (2020).
112. Candadai, A. A., Weibel, J. A. & Marconnet, A. M. A Measurement Technique for Thermal Conductivity Characterization of Ultra-High Molecular Weight Polyethylene Yarns Using High-Resolution Infrared Microscopy. in *Intersociety Conference on Thermal and Thermomechanical Phenomena in Electronic Systems (IEEE ITherm)* (2019).
113. Hahn, J. *How Heat Affects Human Hair: Thermal Characterization and Predictive Modeling of Flat Ironing Results.* (2018).
114. Hyndman Industrial Products Inc. Resistance Heating Wire Nickel-Chromium Alloy 80% Nickel / 20% Chromium - N8: Alloy Data Table. doi:ADT2001.12.17.N8.ENG
115. Liu, P. *et al.* Continuous Carbon Nanotube-Based Fibers and Films for Applications Requiring Enhanced Heat Dissipation. *ACS Appl. Mater. Interfaces* **8**, 17461–17471 (2016).
116. Faulkner, M. G., Amalraj, J. J. & Bhattacharyya, A. Experimental determination of thermal and electrical properties of Ni-Ti shape memory wires. *Smart Mater. Struct.* **9**, 632–639 (2000).

117. Ye, C.-M., Shentu, B.-Q. & Weng, Z.-X. Thermal conductivity of high density polyethylene filled with graphite. *J. Appl. Polym. Sci.* **101**, 3806–3810 (2006).
118. INEOS Olefins & Polymers USA. Typical Engineering Properties of High Density Polyethylene.
119. Yang, C. *et al.* Thermal conductivity enhancement of recycled high density polyethylene as a storage media for latent heat thermal energy storage. *Sol. Energy Mater. Sol. Cells* **152**, 103–110 (2016).
120. Yuan Gao, Marconnet, A. M., Rong Xiang, Maruyama, S. & Goodson, K. E. Heat Capacity, Thermal Conductivity, and Interface Resistance Extraction for Single-Walled Carbon Nanotube Films Using Frequency-Domain Thermorefectance. *IEEE Trans. Components, Packag. Manuf. Technol.* **3**, 1524–1532 (2013).
121. Thirumalai, K., Singh, A., Ramesh, R. & Ramesh, R. A MATLAB™ code to perform weighted linear regression with (correlated or uncorrelated) errors in bivariate data. *J. Geol. Soc. India* **77**, 377–380 (2011).
122. York, D., Evensen, N. M., Martínez, M. L. & De Basabe Delgado, J. Unified equations for the slope, intercept, and standard errors of the best straight line. *Am. J. Phys.* **72**, 367–375 (2004).
123. Rengasamy, R. S. & Kawabata, S. *Computation of thermal conductivity of fibre from thermal conductivity of twisted yarn.* **27**, (2002).
124. Shah, D. U., Schubel, P. J., Licence, P. & Clifford, M. J. Determining the minimum, critical and maximum fibre content for twisted yarn reinforced plant fibre composites. *Compos. Sci. Technol.* **72**, 1909–1917 (2012).
125. Ning Pan, N. Development of a Constitutive Theory for Short Fiber Yams: Part III: Effects of Fiber Orientation and Bending Deformation. *Text. Res. J.* **63**, 565–572 (1993).
126. Bodla, K. K., Murthy, J. Y. & Garimella, S. V. Resistance network-based thermal conductivity model for metal foams. *Comput. Mater. Sci.* **50**, 622–632 (2010).
127. Baxter, S. The thermal conductivity of textiles. *Proc. Phys. Soc.* **58**, 105–118 (1946).
128. Stanković, S. B., Popović, D. & Poparić, G. B. Thermal properties of textile fabrics made of natural and regenerated cellulose fibers. *Polym. Test.* **27**, 41–48 (2008).
129. Abbas, A., Zhao, Y., Zhou, J., Wang, X. & Lin, T. Improving thermal conductivity of cotton fabrics using composite coatings containing graphene, multiwall carbon nanotube or boron nitride fine particles. *Fibers Polym.* **14**, 1641–1649 (2013).
130. Xu, Y. *et al.* Nanostructured Polymer Films with Metal-like Thermal Conductivity. *Nat. Commun.* 1–8 (2019). doi:10.1038/s41467-019-09697-7

131. Song, K. *et al.* Structural Polymer-Based Carbon Nanotube Composite Fibers: Understanding the Processing–Structure–Performance Relationship. *Materials (Basel)*. **6**, 2543–2577 (2013).
132. Liu, J., Xu, Z., Cheng, Z., Xu, S. & Wang, X. Thermal Conductivity of Ultrahigh Molecular Weight Polyethylene Crystal: Defect Effect Uncovered by 0 K Limit Phonon Diffusion. *ACS Appl. Mater. Interfaces* **7**, 27279–27288 (2015).
133. Chae, H. G. & Kumar, S. Rigid-rod polymeric fibers. *J. Appl. Polym. Sci.* **100**, 791–802 (2006).
134. Allen, S. R., Farris, R. J. & Thomas, E. L. High-modulus-high-strength poly-(p-phenylene benzobisthiazole) fibres - Part 1 Heat treatment processing. *J. Mater. Sci.* **20**, 2727–2734 (1985).
135. *Vectran™ Liquid Crystal Polymer Fiber: A Unique Combination of Properties For Demanding Applications.*
136. Kawabata, S. & Rengasamy, R. Thermal conductivity of unidirectional fibre composites made from yarns and computation of thermal conductivity of yarns. *Indian J. Fibre Text. Res.* **27**, 217–223 (2002).
137. Tashiro, K., Kobayashi, M. & Tadokoro, H. Elastic Moduli and Molecular Structures of Several Crystalline Polymers, Including Aromatic Polyamides. *Macromolecules* **10**, 413–420 (1977).
138. ASTM International. Standard Test Method for Stiffness of Fabrics (ASTM D1338-08). 1–6 (2008). doi:10.1520/D1338-08
139. Lammens, N., Kersemans, M. & Luyckx, G. Improved accuracy in the determination of flexural rigidity of textile fabrics by the Peirce cantilever test (ASTM D1388). (2014). doi:10.1177/0040517514523182
140. Smith, P., Lemstra, P. J., Kalb, B. & Pennings, A. J. Ultrahigh-strength polyethylene filaments by solution spinning and hot drawing. *Polym. Bull.* **1**, 733–736 (1979).
141. Teishev, A., Incardona, S., Migliaresi, C. & Marom, G. Polyethylene fibers-polyethylene matrix composites: Preparation and physical properties. *J. Appl. Polym. Sci.* **50**, 503–512 (1993).
142. Liu, X. & Yu, W. Evaluation of the tensile properties and thermal stability of ultrahigh-molecular-weight polyethylene fibers. *J. Appl. Polym. Sci.* **97**, 310–315 (2005).
143. Kong, Y. & Hay, J. N. The measurement of the crystallinity of polymers by DSC. *Polymer (Guildf)*. **43**, 3873–3878 (2002).
144. Bergman, T., Lavine, A., Incropera, F. P. & Dewitt, D. *Fundamentals of Heat and Mass Transfer. John Wiley and Sons* **369**, (2013).

- 145. *Materials Data Book*. (2003).
- 146. *PROPERTIES AND CHARACTERISTICS OF GRAPHITE*. (2013).
- 147. *TYPICAL GRAFOIL SHEET PROPERTIES*.
- 148. Lemak, R. J. High Performance Pyrolytic Graphite Composite Heat Spreaders. 1–26 (2011).
- 149. Christov, I. C. *et al.* Long-range interactions of kinks. *Phys. Rev. D* **99**, (2019).

VITA

Aaditya Candadai completed his B.E. (Hons.) in Mechanical Engineering from BITS Pilani, India in 2015 and received his Master of Science (MSME) in Mechanical Engineering from Purdue University in 2017. His undergraduate research work was based on the performance analysis of a solar thermoelectric generator that employed spectrally selective absorber coatings. At Purdue University, his initial work as a Ph.D. student was related to roll-to-roll manufacturing and characterization techniques of graphene on copper, as well as heat transfer modeling of nanowire networks under the guidance of Prof. Timothy Fisher. His PhD thesis work is co-advised by Prof. Amy Marconnet and Prof. Justin Weibel, and is based on the thermal characterization of flexible high thermal conductivity polymer fabrics for potential heat spreading applications in flexible/wearable electronics. His recent work has received recognition as a featured presentation and an outstanding paper award at the IEEE ITherm 2019 conference, the premier annual conference on electronics cooling.

PUBLICATIONS

1. A. A Candadai, J. A Weibel, A. M. Marconnet, “ A Non-Contact Anisotropic Thermal Measurement Technique using Laser-Infrared Angstrom Method” (*In Preparation*).
2. A. A Candadai, E. J. Nadler, J. S. Burke, J. A Weibel, A. M. Marconnet. “Thermal and Mechanical Characterization of High-Performance Polymer Fabrics for Applications in Wearable Devices” (*Submitted*).
3. A. A Candadai, J. A Weibel, A. M. Marconnet, “Thermal Conductivity of Ultra-High Molecular Weight Polyethylene: From Fibers to Fabrics,” ACS Applied Polymer Materials 2 (2020).
4. A. A. Candadai, J. A. Weibel, and A. M. Marconnet, “A Measurement Technique for Thermal Conductivity Characterization of Ultra-High Molecular Weight Polyethylene Yarns Using High-Resolution Infrared Microscopy,” Intersociety Conference on Thermal and Thermomechanical Phenomena in Electronic Systems (IEEE ITherm), May 2019.
5. A. A. Candadai, A. Kumar, M. A. Alrefae, D. Xemlyanov, and T. S. Fisher, “Rapid Colorimetric Analysis of Graphene on Copper,” Corrosion Science, vol. 138, pp. 319-325, 2018.
6. S. Sadeque, A. A. Candadai, A. Gong, K. Maize, A. K. Ziabari, A. Mohammed, A. Shakouri, T. S. Fisher, and D. B. Janes, “Transient Self-Heating at Nanowire Junctions in Silver Nanowire Network Conductors,” IEEE Transactions on Nanotechnology, vol. 17, pp. 1171-1180, 2018.
7. M. A. Alrefae, A. Kumar, P. Pandita, A. A. Candadai, I. Billionis, and T. S. Fisher, “Process Optimization of Graphene Growth in a Roll-to-Roll Plasma CVD System,” AIP Advances, vol. 7, pp. 115102, 2017.
8. Gilbert Kogo, Bo Xiao, Samuel Danquah, Harold Lee, Julien Niyogushima, Kelsea Yarbrough, Aaditya Candadai, Amy Marconnet, Sangram K. Pradhan, and Messaoud Bahoura. "A Thin Film Efficient PN-junction Thermoelectric Device Fabricated by Self-Align Shadow Mask." Scientific Reports 10 (2020).
9. Kim, Kyungho, Patrick J. Kim, Reaz Ahmed Chowdhury, Rajath Kantharaj, Aaditya Candadai, Amy Marconnet, Vilas G Pol, Jeffrey P Youngblood. “Structural Orientation effect of Cellulose Nanocrystals (CNC) Films on Electrochemical Kinetics and Stability in Lithium-ion Batteries”. Chemical Engineering Journal (2020).